

https://dspace.org/

# Approaches to enhance optical absorption and efficiency of photovoltaic device

**Mayimele, Nhluvuko**

**2017**

http://hdl.handle.net/10539/22747

Mayimele, Nhluvuko (2017) Approaches to enhance optical absorption and efficiency of photovoltaic device, University of the Witwatersrand, Johannesburg, <http://hdl.handle.net/10539/22747>

Downloaded from a DSpace repository. https://dspace.org/

# Approaches to enhance optical absorption and efficiency of photovoltaic device

Nhluvuko Mayimele
Student number: 889250

Supervisor: Prof A Quandt

Co-supervisor: Dr D Wamwangi

Masters Dissertation



WITS
UNIVERSITY

School of Physics

University of the Witwatersrand Johannesburg

South Africa

November 2016

**Abstract**

Organic Photovoltaic (OPV) is an environmental friendly technology that promises efficient and effective harvesting of solar energy. The organic polymers used in the fabrication of OPVs are characterized by low weight, tunable electrical and optical properties. However, the low photo-conversion efficiency (PCE) and instability in air remains a major drawback that limits their commercialization. The project seeks to increase the PCE of a cheap photovoltaic device using plasmonic effects and rare earth doped waveguides to modify the optical response in the active layer. Incorporating regularly shaped silver (Ag) nanoparticles (NPs) in OPVs through the surface plasmon resonance will enhance tunable absorption and scattering of light. These NPs are prepared by reducing $AgNO_3$ with N,N-dimethylformamide (DMF) and using 2,2-Poly(vinylpyrrolidone) (PVP) as a stabiliser at different reaction times. The Ag NPs have shown different shapes such as spherical and prism shapes of 14, 15 and 16 nm visualised by TEM. The flexibility of the process allows tunability of the optical properties of Ag NPs by variation of the surface to volume aspect ratios. Optical resonance dependences on shape has been measured in the range of 350 nm and 450 nm. The surface plasmon resonance by Ag NPs has been modelled by MIT Electromagnetic Equation propagation (MEEP) software based on the modified Drude-Lorentz model to calculate the optical absorption and scattering cross-sections. The dependence of absorption and scattering cross-section on the Ag NPs size has been established by MEEP and it is in agreement with the experimental data. The optimum incorporation of the noble metal in the OPV cell structure is pursued to achieve maximum light scattering and absorption at the NPs plasmon resonance, as well as to expand the absorption spectrum beyond the visible region. Furthermore the Ag NPs were incorporated onto organic solar cells where they were blended in poly(3,4-ethylenedioxythiophene)

polystyrene sulfonate (PEDOT:PSS) in volume ratios, then spin coated onto a clean Indium Tin Oxide (ITO) glass. The polymer blend of [6,6]-phenyl $C_{61}$-butyric acid methyl (PCBM) ester and Poly(3-hexylthiophene-2,5-diyl (P3HT), P3HT:PCBM was spin coated on the Ag NPs incorporated PEDOT:PSS to make a device. We report an efficiency enhancement from 0.703% (a pristine device) to 1.054% (a device with Ag NPs) on organic solar cells.

The planar $Eu^{3+}$ doped silica-hafnia waveguides were synthesized by sol-gel methods to investigate light management through up and down conversion. SEM images show a fully densified (without cracks) waveguide with no phase separation at the wavelength scale, and with a refractive index and thickness of 1.5848 and 1.4951 $\mu$m respectively. Rare earth doped ($SiO_2 - HfO_2{:}Eu^{3+}$) waveguides optical response excited by argon ion laser at 488 nm showed a strong red emission peak located at 613 nm meaning that they are good down–converter and they can harvest solar energy.

# Declaration

I Nhluvuko Mayimele declare that " Approaches to enhance optical absorption and efficiency of photovoltaic device " is my own, unaided work submitted at the University of the Witwatersrand, Johannesburg, South Africa. And that this work has not been submitted for any degree or examination in any other institution of higher learning. Moreover, that all sources used or quoted have been indicated and acknowledged with complete references.

Date: .....2016

Signature: .....

# Acknowledgement

I would like acknowledge my supervisor Prof A Quandt and my co-supervisor Dr D Wamwangi for the energy and effort expended in the success of this project. Much appreciation to Dr GC Righini (Associate Scientist, Enrico Fermi Center and Nello Carrara Institute of Applied Physics in Italy) and Prof M Ferrari (Consiglio Nazionale delle Ricerche CNR-IFN (Istituto di Fotonica e Nanotecnologie) in Trento(Italy) ) for the financial and training support in the Italy- South Africa collaboration on the bi-lateral project "plasmonics for a better efficiency for solar cells"(PLECS). Thank you Center of Excellence for Strong Materials (CoE-SM) for funding. I would also like to acknowledge Lustyna Vasilchenko and Wesley Cardoso Muscelli for assisting as well with experiments in CNR-IFN (Istituto di Fotonica e Nanotecnologie) lab in Trento(Italy). To the schools of Physics and Chemistry for provision of research infrastructure. Mr F Otieno thank you for assisting on the experiments and Mr F Mohammed for assisting with computational numerical analysis throughout the project. To my group, which is led by Prof A Quandt here at Wits, thanks for the support and time you gave me to become what I am today. More specially to Dr R Warmbier and as well the Materials for Energy Research Group (MERG). I would like to thank Mr M Ngobeni, Mr O Nukeri and Mr MA Mayimele for support you gave me.

# Dedication

I dedicate this dissertation to my mother Nxalati Baby Baloyi and my brother Meehleketo Mayimele.

# Contents

**List of Figures** **vii**

**List of Tables** **x**

**1 Introduction** **1**

1.1 Problem statement . . . . . 7

1.2 Aim of the project . . . . . 7

1.3 Objectives of the project . . . . . 8

1.4 Dissertation structure . . . . . 9

**2 Literature review** **11**

2.1 Mechanisms of operation of an organic photovoltaic device . . . . . 11

2.1.1 Absorption of photons . . . . . 14

2.1.2 Single junction solar cells . . . . . 15

2.1.3 Operating principles of organic solar cell . . . . . 17

2.1.4 Reflection losses . . . . . 20

2.2 Photoluminescence . . . . . 22

**3 Theoretical frame work** **27**

3.1 Plasmonics . . . . . 27

3.1.1 Surface plasmon condition . . . . . 27

3.1.2 Energy dispersion of metalic nanoparticles . . . . . 30

3.1.3 Numerical modelling for scattering and absorption cross-section 34

3.2 Simulations of the absorption and scattering cross-section of Ag NPs with MEEP . . . . . 41

3.3 Waveguides for applications in photonics . . . . . 44

3.3.1 Waveguide structure . . . . . 45

3.3.2 Boundary condition for electromagnetic fields. . . . . 45

3.3.3 Optical waveguides . . . . . 46

3.3.4 Transverse magnetic and electric modes in a planar wavegiude . 48

**4 Methodology** **51**

4.1 Synthesis of Ag nanoparticles . . . . . 51

4.2 Fabrication of Organic photovoltaic device . . . . . 53

4.2.1 Cleaning of substrate . . . . . 53

4.2.2 Reference solar cell . . . . . 53

4.2.3 A solar cell with Ag NPs incorporated in the hole transport layer 54

4.2.4 Thermal evaporation technique . . . . . 55

4.3 Sol-gel technique . . . . . 57

4.3.1 Dip-coating process . . . . . 60

4.3.2 Cleaning of substrate . . . . . 61

4.3.3 $SiO_2 - HfO_2$ planar waveguides doped with $Eu^{3+}$ . . . . . 61

4.4 Techniques used for optical and morphology analysis . . . . . 62

4.4.1 Scanning electron microscopy for morphological analysis . . . . 62

4.4.2 Transmission electron microscopy for morphological analysis . . 63

4.4.3 UV-vis spectroscopy for optical characterization . . . . . 64

**5 Results and discussion** **65**

5.1 Data analysis from MEEP simulation . . . . . 66

5.1.1 Methods of the simulation . . . . . 66

5.1.2 Results from the simulation: . . . . . 67

5.2 Morphological analysis of Ag NPs . . . . . 72

5.3 The optical absorption of Ag NPs by UV-Vis Spectroscopy . . . . . 80

5.4 The I-V characteristics of organic photovoltaic cell and analysis . . . . 82

5.5 Morphology of $SiO_2 - HfO_2$ planar waveguides . . . . . 89

5.6 M-line spectroscopy measurement for planar silica-hafnia waveguides . 91

5.7 Photoluminescence properties of europium doped silica-hafnia waveguides . . . . . 92

**Conclusions** **95**

**Future research** **97**

# List of Figures

1.1 World energy consumption demands, and the projected growth in solar energy as a renewable and alternative energy resource [4]. . . . . 2

1.2 The efficiency road map of diverse families of solar cell technologies [6]. 3

2.1 A solar emission spectrum [43] . . . . . 15

2.2 (a) Description of the absorption and thermalization losses occurring in a solar cell . . . . . 16

2.3 (1) Photoexitation of the donor to generate a bound electron hole pair, called an exciton. (2) Exciton diffusion to the D-A interface. A distance longer than the maximum diffusion length (max DL) will lead to relaxation of the exciton. (3) Bound exciton dissociation at the D-A interface to form a germinate pair. (4) Free charge transportation and collection at electrodes [51]. . . . . 18

2.4 Energy levels of triply charged lanthanide ions [79] . . . . . 25

3.1 Two media with dielectric function separated at interface [82] . . . . . 28

3.2 Real and imaginary part of the dielectric constant for silver according to the Drude-Sommerfeld free-electron model . . . . . 33

3.3 A sphere of radius $a$ exposed to the E field . . . . . 34

3.4 A three layer slab optical waveguide with refractive indexes, $n_s, n_f, n_c$ . 49

4.1 Schematic of thermal evaporation . . . . . 55

4.2 The experimental set-up of the thermal evaporation system used in the present study. . . . . 56

4.3 Sol-gel processing options . . . . . 59

5.1 The scattering cross–section for silver spheres of different diameters. . . 68

5.2 The absorption cross-section for a simple plane surface with silver spheres of different diameters. . . . . 69

5.3 Scattering/absorption cross-section for a spherical Ag NPs of a diameter 5 nm in a simple plane surface. . . . . 70

5.4 Scattering/absorption cross-section for a spherical Ag NPs of a 100 nm diameter in a simple plane surface. . . . . 70

5.5 TEM images showing spherical Ag NPs. . . . . 72

5.6 Histogram showing Ag spherical NPs of an average diameter of 15 nm. 73

5.7 TEM images showing prism like Ag NPs. . . . . 73

5.8 Histogram showing agglomerated prism like Ag NPs of an average diameter of 14 nm. . . . . 74

5.9 TEM images showing nucleated prism Ag NPs. . . . . 74

5.10 Histogram showing agglomerated Ag NPs average diameter of 16 nm. . 75

5.11 SAED patterns of Ag NP synthesized at varied reaction time . . . . . 76

5.12 EDS of Ag NPs synthesized at varied reaction times . . . . . 79

5.13 Absorption spectrum of Ag NPs fabricated at varied reaction times . . 80

5.14 Absorption spectra and TEM images showing interspacing of spherical Ag NPs . . . . . 81

5.15 Absorption spectra for Ag spherical NPs of 10 nm diameter with MEEP simulation. . . . . 82

5.16 I–V characteristics of fabricated devices with different concentration of Ag NPs . . . . . 83

5.17 Shunt resistance increase at constant open circuit voltage. . . . . 86

5.18 J-V characteristics fabricated device with varied concentration of Ag NPs in PEDOT:PSS. . . . . 87

5.19 P-V characteristics fabricated device with varied concentration of Ag NPs in PEDOT:PSS . . . . . 88

5.20 $SiO_2 - HfO_2$ waveguide at the edge (left) and at the surface (right) of the sample . . . . . 90

5.21 EDS analysis of $SiO_2 - HfO_2$ waveguides . . . . . 90

5.22 M-line measurement for both modes TE and TM . . . . . 91

5.23 Energy level diagram for $Eu^{3+}$ ions. . . . . 92

5.24 Room temperature photolumensence spectrum of $Eu^{3+}$ doped $SiO_2 - HfO_2$. . . . . 93

# List of Tables

2.1 Solubilities of P3HT and PCBM in halogenated solvents [31]. . . . . 12

5.1 Parameters used in the modelling of Ag NPs absorption and scattering cross–section. . . . . 67

5.2 Summary of the perfomance banch mark values of $I_{sc}$, $V_{oc}$, $I_{P_{max}}$ and $V_{P_{max}}$ for the OPVs with spherical Ag NPs blended in PEDOT:PSS . . 84

5.3 Summary of the device characteristics parameters $J_{SC}$, $R_{CH}$, $R_S$ and $R_S$ for OPV cell with spherical Ag NPs blended in PEDOT:PSS. . . . . 85

5.4 Summary of the performance (including Power produced by the cell and photo convertion efficiency) of the OPVs with spherical Ag NPs blended in PEDOT:PSS. . . . . 89

# Chapter 1

# Introduction

The use of fossil fuels as an energy source continue to raise environmental concerns due to their deleterious effects [1]. These concerns have triggered concerted efforts for innovation on clean and renewable energy alternatives. Furthermore the increased demand for energy by growing economies have compounded the energy deficit problem in the third world [2]. To address this shortage, harvesting solar power is considered as one of the effective and sustainable approaches towards mitigating the energy crisis. The search for a low cost solar cell has steered research towards organic photovoltaic and halide perovskite solar cells [3]. In the mid to long term, the need to increase the use of solar energy sources would be very important to keep up with the global energy needs, as figure 1.1 elaborates. In South Africa, the shortage and rationalization of the electricity usage has led to load shedding which has far reaching implications to the economy and industry.

The production of the most effective solar cell with higher photo-conversion efficiency (PCE) still remains a problem, not to mention the prohibiting costs, since the materials explored for photovoltaic applications are expensive. The worst case of a photovoltaic industry is that it is highly subsidized, which renders this energy alternative a less competitive option. The current generation of organic solar cells is less expensive and provides an efficiency of more than 15% for a single junction cell [5]. Solar cells

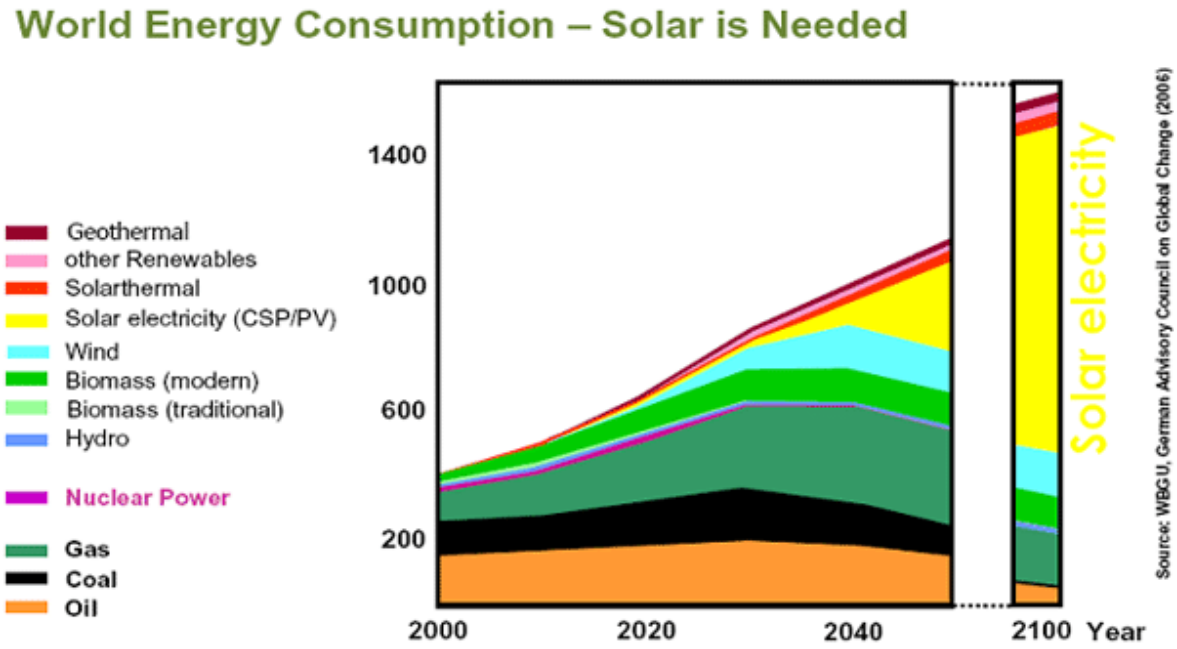



**Figure 1.1:** World energy consumption demands, and the projected growth in solar energy as a renewable and alternative energy resource [4].

fabricated from less expensive materials with similar performance benchmarks would provide a commercially viable technology for application in $3^{rd}$ world countries. Figure 1.2 illustrates the drive towards materials that yield high PCE for the replacement of silicon based solar cell which continues to be regarded as the standard PV. Interestingly the high potential of organic halide perovoskite and hybrid based solar cells is explicitly demonstrated, due to their rapid increase in the PCE over a short period of time. The push towards these materials has been mainly because of their cost effective and environmental friendly attributes.

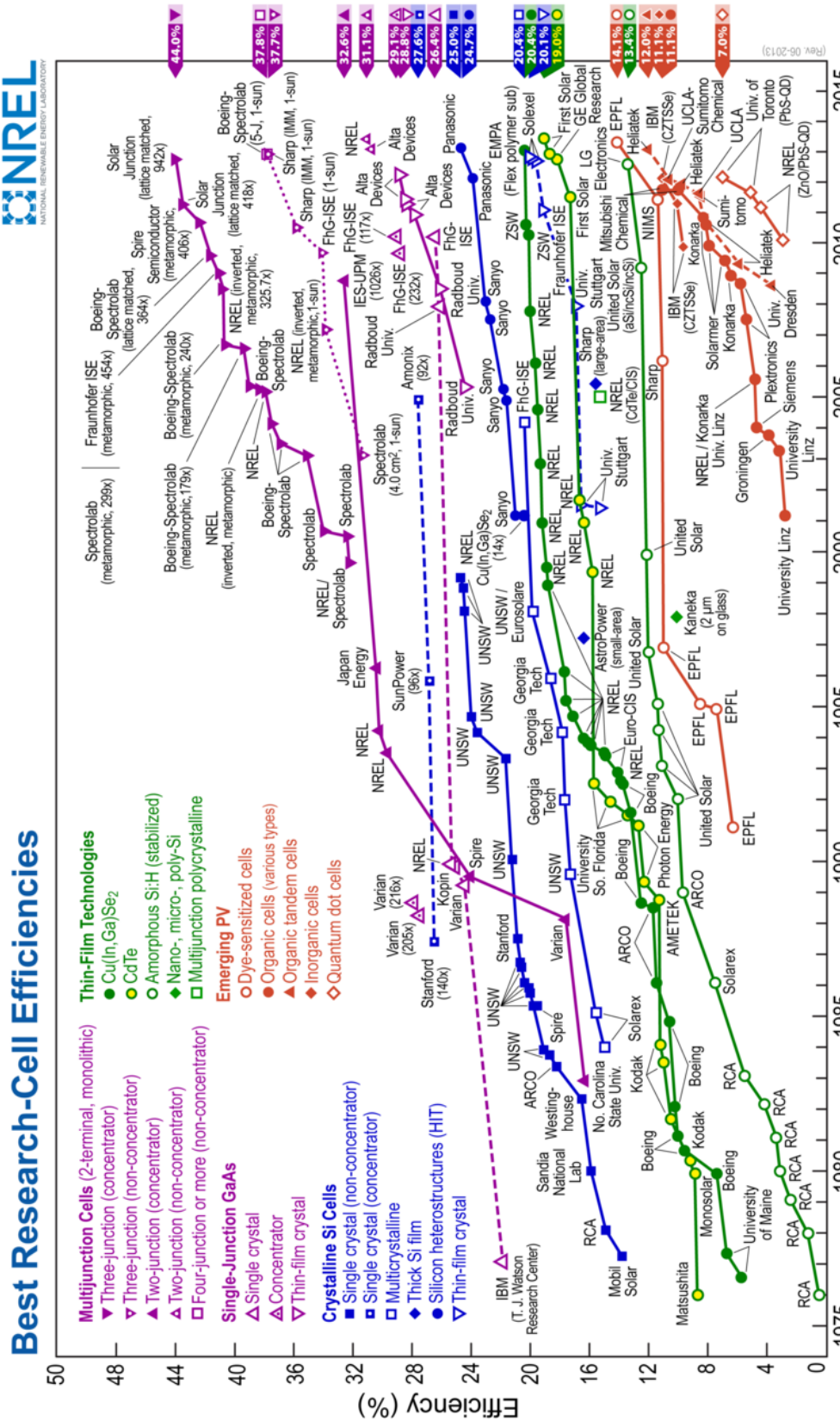



**Figure 1.2:** The efficiency road map of diverse families of solar cell technologies [6].

In general a solar cell is known as a photovoltaic (PV) cell. PV is a device which converts solar energy directly into electricity. It is also considered to be a form of a photoelectric cell, because of its electrical properties such as current, voltage, or resistance [7]. These properties varies as they are exposed to light. Solar cells may be defined as building blocks of photovoltaic modules called solar panels [8].

Enormous research focus has been directed toward the development of highly efficient and stable organic photovoltaics. The intensive research on these materials have been driven by the following positive attributes [9]:

- The cost of high volume production of the polymers is low, making organic photovoltaic (OPV) quite affordable.
- Most polymer-based photovoltaic elements are easily fabricated by solution processing at low temperatures and the thermal evaporation of the electrode deposition requires small amounts of materials.
- OPVs are marked by ultra fast optoelectronic response and generation of charge carriers at the donor – acceptor interface.
- Structural flexibility of OPVs enhances their application suite. There are many possible functionalities and chemical structures of organic materials that favours the current research for competitive alternative materials that has the necessary PV properties.
- The band gaps of OPVs can be varied by changing the length and the functional group of polymers during synthesis. They are thus chemically tunable so that their optical and electronic properties can be separately modified without trade off's concerning their solubility and structure (the valance highest occupied molecular orbital (HOMO) and conduction lowest unoccupied molecular orbital (LUMO) band energies, the band gap and the charge transport adjust separately).

Despite the many positive properties of photovoltaic devices, they have efficiencies less than 50% due to the losses and band gap mismatch with the solar emission spectrum [10]. The two major mechanisms that limit the PCE of any general solar cell constitute:

- Thermalisation of high energy photons. This effect is ascribed to the intraband transitions involving the high energy photons and hot electron carrier. Thus the need to use down conversion in cases where thermalisation of photons having energies larger than that of a band gap of the semiconductor will reduce losses due to their excess energy via thermal equilibration [11].
- Non absorption of sub-band photons (Transmission losses). For transmission losses, the energy barrier between the HOMO level of the donor and LUMO level of the acceptor are too high for photon absorption. Thus it makes it impossible to absorb low energy photons ($E < E_g$) [12]. To mitigate the losses of photons of energy $E < E_g$ the up conversion concept is adopted to generate photon energies at resonance with the band gap energies of the active layer.

Beside photon cutting and up conversion for the enhancement of optical scattering and absorption of solar cell, the use of metallic nanoparticles (NPs) of diverse shapes and sizes in a solar cell can enhance the PCE. The additional functionalized layer containing metallic NPs uses surface plasmon resonance effects to absorb light and scatter it preferentially into the active layer of the solar cell [13]. A combination of plasmonic effects with rare earth doped waveguides can widen the available absorption spectrum of the solar cell through up- and down-conversion, and increase the absorption efficiency of thin film solar cells [14].

Rare earth ions ($Er^{3+}$, $Pr^{3+}$, $Ho^{3+}$, and $Tm^{3+}$) doped into oxide materials or heavy metal fluoride have been used to fabricate optical amplifiers that operate at the wavelengths of 1.55, 1.46, and 1.31 $\mu$m. These materials are also being used as up-conversion lasers and detectors of the infra-red radiation [15, 16]. Up–conversion is a luminescence

process where two or more photons of low energy are converted to a higher energy photon. When a layer containing an up-conversion phosphor is attached to the rear of a solar cell, the sub-bandgap photons that are transmitted by the solar cell can be absorbed by the up-conversion layer and converted into higher energy photons [17]. Up-conversion may enhance the response of solar cells in the infrared region [18].

The metallic NPs are embedded in a surrounding dielectric medium. The absorption, scattering, reflection and transmission of an incoming plane wave of such a system will be determined from the knowledge of the Poynting vector, calculated by the MIT Electromagnetic Equation Propagation (MEEP) software. MEEP is a finite difference time domain software that carry many other properties to determine the scattering and absorption cross-sections spectra of nanostructured materials. We will examine the scattering from single metallic sphere and from spheres arranged on a regular lattice forming a plasmonic photonic crystal [19].

Furthermore, metallic NPs having sizes smaller than the wavelength of light will give stronger dipole excitations similar to localized surface plasmon resonances (LSPR)[20]. LSPR is an optical phenomena generated by light when it interacts with conductive NPs that are smaller than the incident wavelength [12, 21]. This effect has attracted extensive research in both applied and fundamental physics [22]. The resonance frequency of the collective oscillation of electrons are referred as surface plasmon (SP), that which is obtained through optical characteristics of a metal and the surrounding environment such as:

- nanoparticle size,
- nanoparticle shape,
- coverage/density of nanoparticle's,
- inter particle spacing.

The collective charge oscillations have a large effect on the surface plasmon resonance enhancement in local fields that are inside and near the metallic NPs. The field enhancement caused by the resonance of free electrons is used in surface-enhanced Raman scattering (SERS) [23] and are investigated in detail for numerous of applications in non-linear optical devices [24].

## 1.1 Problem statement

OPV device are problematic because of their low PCE and instability. However their low weight and low cost enables them to stand out as a superior potential PV device that could remedy the exigent energy challenges. Their application consequently leads to reduced environmental pollution resulting from reliance on fossil fuels. The biggest challenge of OPV's is their limited life time due to their instability in air and UV. When OPVs are exposed to oxygen they degrade rapidly. This is one of the leading factors that severely limits their commercialization in the market. For the widespread usage of OPVs, high module efficiencies (more than 10%) and suitable lifetimes (in excess of 25 years) are required. There is need to develop new strategies to increase light harvesting capabilities, as well as the improvement of device architecture, modification of the optoelectronic and the development of cost effective device processing methods properties of the active layer are important for the enhance the efficiency and device stability.

## 1.2 Aim of the project

The project seeks to increase the PCE of a cheap photovoltaic device using enhanced optical absorption and scattering approaches by incorporating spherical Ag NPs in functionalized PEDOT:PSS thin films. The incorporation of metallic NPs in OPV cell

structure is explored as for to achieve maximum light scattering and absorption at the NPs plasmonic resonance within the visible region. In addition the application of light guiding and down conversion through rare earth doped waveguide ($SiO_2$-$HfO_2$ ) will be studied.

## 1.3 Objectives of the project

The *objectives* of the project are outlined as follows:

1. Synthesis of Ag NPs of definite shape and size through the wet chemical reduction.
2. Establish the fundamental optical and plasmonic properties of Ag NPs in a functionalized thin film. The properties are dependent on structural effects such as size, surface structures, shape, density and dielectric medium encapsulating them.
3. Numerical modelling of the optical data by suitable tools such as MEEP and Python are used to optimize on the plasmonic characteristics that gives better optical properties.
4. To incorporate metallic NPs into the OPV device for light scattering purpose such that there's an enhancement light absorption on the OPV. The effect of optical absorption enhancement on the optoelectronic properties of OPV will be established as a proof of concept.
5. Waveguides as an approach to guide/scatter light.

## 1.4 Dissertation structure

The dissertation is structured as follows:

**Chapter 1**: Introduces the background information and trends in photovoltaic technology and the ensuing global demands for energy resources. Here the projected growth of renewable energy is highlighted. In addition the advantages of low cost OPV alternatives are presented against the backdrop of efficiency and stability.

**Chapter 2**: Presents a literature review on the mechanisms of operation of an organic solar cell. The associated device requirements for extraction of PCE are discussed.

**Chapter 3**: A brief discussion of the theoretical framework detailing the conditions for surface plasmon resonance is presented, using the Drude - Lorentz model and Maxwell's equations. We provide the theoretical description of the dielectric function of metal NPs of diverse shapes and sizes. Further theoretical principles describing light propagation in waveguides is presented.

**Chapter 4**: Discusses the synthesis of Ag NPs and the techniques used in fabrication of organic solar cell (device), as well the techniques used in fabrication of waveguides. It also includes the techniques used in the characterization and analysis of the samples as prepared for morphology analysis and optical properties.

**Chapter 5**: Discusses the simulation (MEEP) results of spherical Ag NPs and morphological and optical analysis of Ag NPs. It also include the I-V or J-V characteristics data analysis of organic solar cell with and without Ag NPs incorporated in PEDOT:PSS, as well the morphology and optical characterisation of $Eu^{3+}$ doped $SiO_2 - HfO_2$ waveguides.

**Chapter 6**: Gives a summary of the results concerning simulations by FDTD methods of Ag NPs and the morphology with optical characterization of Ag NPs and the

efficiency enhancement of Ag NPs incorporated OPV's. And also the summary on waveguides.

# Chapter 2

# Literature review

In this chapter the general working principles of organic solar cells are introduced. We discuss the photo absorption mediated through exciton generation and its diffusion from the donor – acceptor acceptor interface. Subsequently the dissociation of the exciton at the interface is highlighted. The conceptualization of charge transport and charge collection are discussed briefly in this chapter as well the production of free electrons and holes. Subsequently the parameters that are used to relate to the performance benchmarks in solar cells are discussed in this chapter.

## 2.1 Mechanisms of operation of an organic photovoltaic device

An organic solar cell is a device that uses conjugate polymers or small organic molecules such as PCBM ([6,6]-phenyl $C_{61}$-butyric acid methyl ester) and P3HT (Poly(3-hexylthiophene-2,5-diyl)) as active layers for light absorption and charge transport in order to generate electricity from sunlight through the photovoltaic effect [25]. These organic materials are considered as conjugated systems in which the optical absorption and charge transport are dominated partly by delocalised $\pi^*$ and $\pi$ orbitals [26].

Materials such as P3HT are mainly used as a donor because of its suitable band gap (1.9 eV $< E_g <$2.0 eV ) spans within the longer ultra-violet (UV) and the visible spectrum (400 nm - 650 nm). It also has a high hole mobility (between $10^{-5}$ and $10^{-4}$ $cm^2/Vs$) [27, 28] and it is also partially stable in air. Importantly its solubility in chlorinated solvents such as chloroform, chlorobenzene, dichlorobenzene and trichlorobenzene (see table 2.1 for the solubility values of PBCM and P3HT) enables it to be fabricated thin film using solution processing. PCBM, on the other hand has a high electron affinity and it can delocalize negative charges as long they are relatively low in absorption in the visible spectrum (400 nm) [29]. The mechanism of OPV device operation needs to have four basic attributes namely: Absorption of light to generate electron-hole pairs (excitons). Secondly, the exciton diffusion to the (donor – acceptor) interface, thirdly the separation of charge carriers and finally, the separate extraction of those carriers to an external circuit [30]. A detailed treatment of each attribute is presented in the subsequent paragraphs.

| Solubility values of P3HT and PCBM in halogenated aromatics (mg $mL^{-1}$) | | |
|---|---|---|
| Halogenated aromatics | P3HT solubility | PCBM solubility |
| Chlorobenzene | 15.9 | 59.5 |
| Dichlorobenzene | 14.7 | 42.1 |
| Trichlorobenzene | 2.7 | 81.4 |

**Table 2.1:** Solubilities of P3HT and PCBM in halogenated solvents [31].

Exclusive features of organic photovoltaic materials:

- Photogenerated excitons are bounded strongly and don't naturally dissociate into free charge pairs. For dissociation to take place the input energy should be in excess of 100 meV.The carrier generation doesn't actually come from the absorption of light [32, 33].
- Charge transport takes place in localised states instead of the transport inside the band, it comes from low mobilities in the range (2 – 5.8 $\times$ $10^{-4}$ $cm^2/Vs$)

[34, 35].

- The optical absorption is relatively low when compared with the values in the solar emission spectrum [32].
- Sufficient absorption coefficients of ($10^7$ $cm^{-1}$) are obtained such that the adequate optical densities are achievable, at the peak wavelength of thin films.
- A lot of materials are susceptible to degradation when exposed to oxygen or presence of water.

The inter-molecular van der Waals forces in organic solids are known to be weak compared to the bonds in inorganic crystals. They are also more weaker than the intramolecular bonds. Resulting in electronic states that are localised in an isolated molecule and don't create bands. The low mobility is critical, when a disorder of a high degree is found in numerous organic solids. The optical excitations is only achievable on photons that are in the visible region as they usually involve the $\pi$ to $\pi^*$ transitions [36]. Hence most of conjugated solids tend to absorb light in the blue or green region, thus rendering absorption in the infra-red or red difficult to harvest. Nevertheless, the absorption bandwidth can be tuned by changing the conjugation degree to attain a broader spectral sensitivity such as in a highly conjugated dye molecule [37].

Properties that imposes some limitations on OPV devices [38]:

- A strong electric field is needed to separate the photogenerated exciton.
- Low mobility of the charge carriers limits the optimal thickness of devices to few nm.
- Light absorption is quite limited beyond the solar emission spectrum, which curbs the photocurrent produced.
- Very thin devices means that interference effects is vital.

- The sensitive photocurrent to temperature mainly by hopping transport.

In organic polymers, the absorption coefficient $\alpha(E)$ is equivalent to the density of the HOMO states in which an electron hole is generated, and as well the LUMO level density to which the electron is excited too. Assuming that $\alpha(E)$ is uniform in a polymer, the incoming light intensity out from a glass slab having thickness $x$, is described by Beer's law as:

$$I = I_o e^{-\alpha x} \tag{2.1}$$

and $I_o$ is the incident light intensity [39].

### 2.1.1 Absorption of photons

In OPV devices, at most cases a small portion/fraction of the incident light is absorbed, mainly because of the band gaps that are very large relative to the solar emission spectrum (see figure 2.1). A band gap of 1.1 eV (1100 nm) is needed to absorb 77% of the solar radiation here on earth. This is sharp contrast with the band gap values of the most semiconducting polymers as they have band gaps in excess of 2.0 eV (600 nm), the trade off is thus limited by optical absorption of at least 30% [40]. Furthermore the low film thickness ( 100 nm) also reduces the optical absorption significantly. The thickness of the cell is constrained by the low carrier mobilities and short exciton diffusion length ( 20nm). Fortunately enough the absorption coefficient of organic materials is basically higher than that of silicon, thus making it possible for devices of active layer thickness of 100 nm absorb between 60% and 90%, if reflective back contacts are used [41, 42].

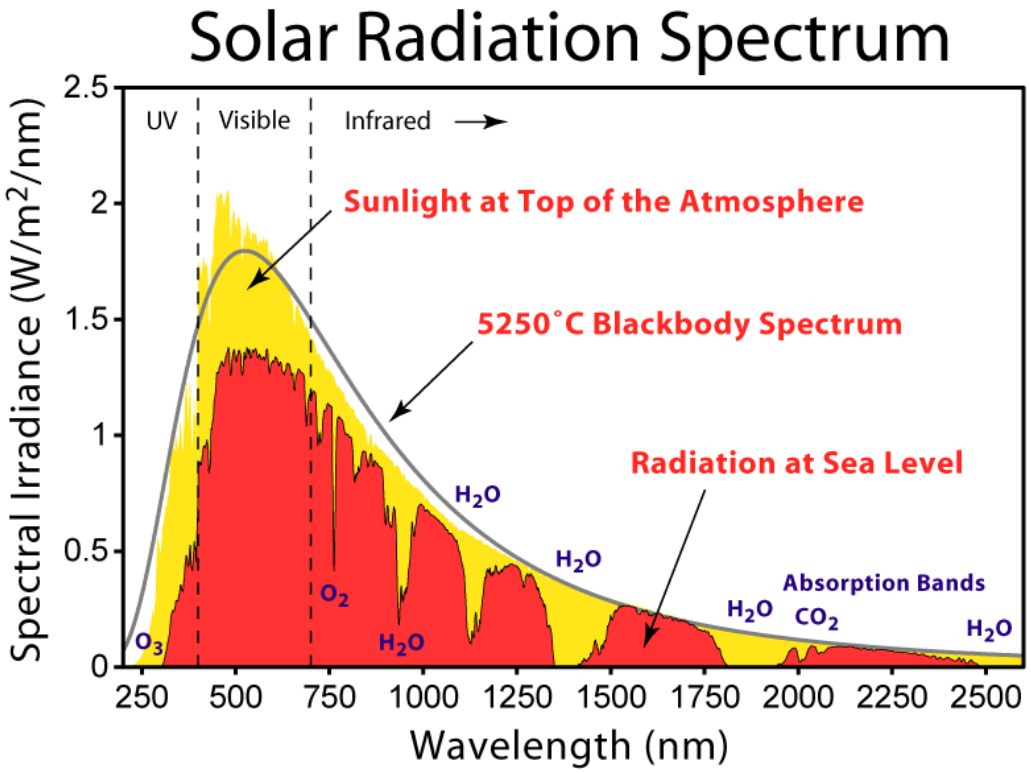



**Figure 2.1:** A solar emission spectrum [43]

### 2.1.2 Single junction solar cells

Shockley and Queisser carried out calculations in 1961 for the evaluation of thermodynamic limitations of the energy conversion efficiency of photovoltaics [44]. Figure 2.2 illustrates the basic phenomena (thermalization losses) that determines the energy conversion efficiency:

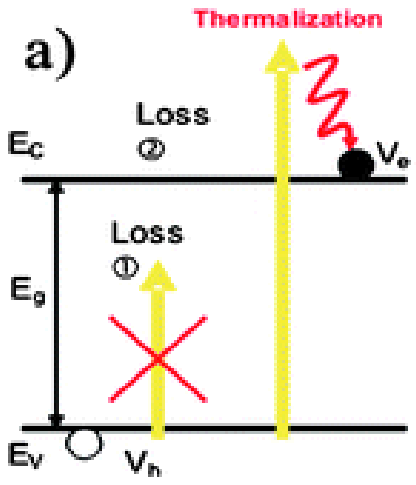



**Figure 2.2:** (a) Description of the absorption and thermalization losses occurring in a solar cell [45].

- Photons with energy greater than that of the band gap of the photoactive materials get absorbed to contribute to photovoltaic conversion.
- Hot charge carriers that are created by photon absorption, relax down to conduction band of the photoactive materials, will contribute to the rise of thermalization. This energy is released as heat to the device.
- The current collection (short-circuit current) and the forward bias injection current (open-circuit voltage) are effected by recombination losses [46].

These phenomena have direct consequence on the maximum charge extraction of potential at open circuit ($V_{OC}$). This is because of the band gap of a photoactive material. We then consider the Fill Factor (FF). The Fill Factor (FF) is the ratio of the maximum power from the photovoltaic device to the product of short circuit current ($I_{SC}$) and open circuit voltage ($V_{OC}$) [45]. The fill factor is mainly affected by the device's shunt and series resistances and diodes losses. If the shunt resistance ($R_{sh}$) is increased, while the series resistance ($R_s$) is decreasing, this will then lead to a higher fill factor,

resulting in a higher efficiency, and thus enabling the cell's output power (P) to be closer to its theoretical maximum [47]:

$$FF = \frac{P}{V_{OC} \times I_{SC}} \tag{2.2}$$

Assuming that the ideal fill factor (FF) is 1, then the maximum efficiency $\eta(E_g)$ obtained with materials of band gap energy $E_G$ is given by:

$$\eta(E_G) = \frac{J_{SC}(E_G) \times V_{OC}}{P_{in}} \tag{2.3}$$

where $P_{in}$ is the input power $W/m^2$ or is given as the optical radiance (1 sun = $100mW/cm^2$ for A.M 1.5G), while the open circuit potential is given by

$$V_{OC} = \frac{K_B T}{q} ln(\frac{J_{sc}}{J_o} + 1) \tag{2.4}$$

$$= f(E_G) \tag{2.5}$$

but $V_{OC}$ is dependent on the dark current $J_o$ and $J_{SC}$ is the short circuit current density calculated by:

$$J_{SC}(E_G) = \frac{I_{SC}}{A} \tag{2.6}$$

Where A is the active area of the device [44, 48].

### 2.1.3 Operating principles of organic solar cell

The operating principles of organic solar cells are illustrated in the electronic band diagram (figure 2.3). The processes entailing this operation are discussed below:

- The photoexcitation of a donor material through light absorption to generate

excitons, which is a bound electron–hole pair. The exciton diffuses into a donor–acceptor (D–A) interface where exciton dissociation occurs through an electron–transfer process.

The internal electric field generates the photocurrent and photovoltage from the separated charge carriers, which move to the electrodes. But the limiting factors of their lifetimes and diffusion length only allow excitons to diffuse for a short distance [49, 50, 51] and the donor excitons generated far from the heterojunction interface will decay fast to ground state without contacting the acceptor [51]. This then leads to loss of absorbed photons and a reduction of the quantum efficiency.

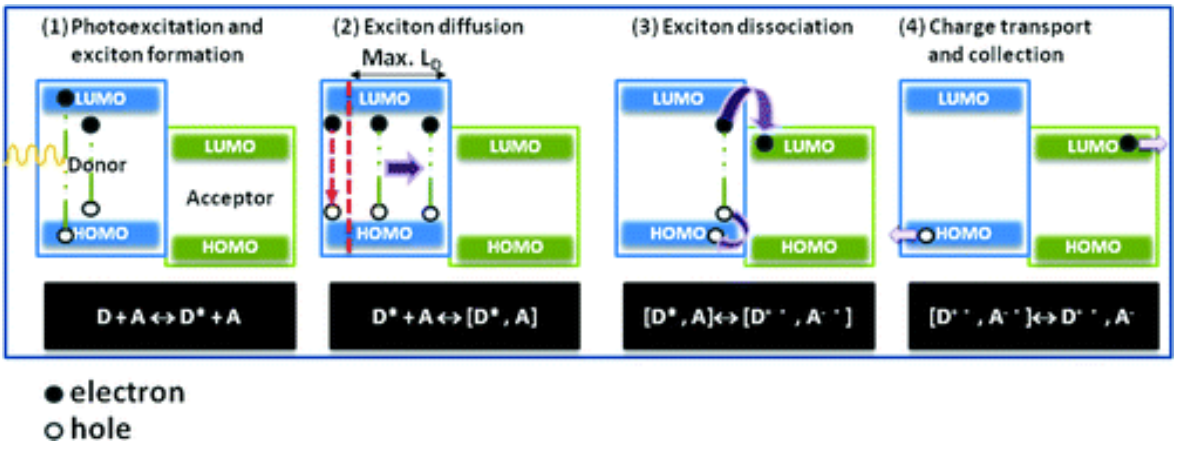



**Figure 2.3:** (1) Photoexitation of the donor to generate a bound electron hole pair, called an exciton. (2) Exciton diffusion to the D-A interface. A distance longer than the maximum diffusion length (max DL) will lead to relaxation of the exciton. (3) Bound exciton dissociation at the D-A interface to form a germinate pair. (4) Free charge transportation and collection at electrodes [51].

#### 2.1.3.1 Exciton difussion

The binding energy and diffusion length of the exciton are influences by the location of the dissociation site. The dissociation site is a site where the absorbed photon with low energy diffuses. The recombination of the electron and hole, i.e. the decay of the exciton, is limited by resonance stabilization due to the overlap of the electron and

hole wave functions, resulting in an extended lifetime for the exciton. Exciton diffusion ranges in pigments and polymers are usually likely to be around 10 nm [52].

Now the concept of a bulk heterojunction (BHJ) pioneered by Yu et al [53] comes to play and has thus been used to increase the donor-acceptor interface area without compromising the exciton diffusion length. Organic BHJ solar cells generally have efficiency values in the range of 10% [54] . In this approach the donor (P3HT) – acceptor (PCBM), are mixed in nanoscale dimensions to enhance the interpenetrability of the resulting network, thus providing the requisite field to split the exciton. The standard efficiency of the P3HT:PCBM based device is 3.6% under standard conditions, however a high PCE of about 3.5 to 5.0% can be achieved by increasing the nanoscale morphology or changing the constituents of the polymer blend [55, 56].

The generation of a bicontinuous network normally generates two channels for transporting holes in the donor and electrons domains, producing an efficient charge collection [51]. Studies on BHJ has proved that the open-circuit voltage depends on the change of energy between the LUMO level of the acceptor and HOMO level of the donor. This assumption/condition is valid if there's a good electrical contact at the electrode organic layer interfaces [57]. The efficiency of exciton dissociation is predominantly dependent on the heterojunction-interface area. This provides the ability of an exciton to diffuse through the interface [58].

#### 2.1.3.2 Charge separation

Charge separation (exciton dissociation) occurs at the organic metal/semiconductor interfaces, even at impurities like oxygen, and also between materials with great difference in ionisation potentials (IP) and electron affinities (EA). Thus some material may serve as electron donor (D) while the other as an electron acceptor (A) since it receives the positive charge. If the difference in IP and EA is not sufficient, the exciton

will only just jump up and down onto the material with the lower band gap without splitting up its charges. Hence recombination will preferentially occur without charge contribution to the photocurrent [9, 52].

#### 2.1.3.3 Charge transport

The transport of free charge carriers in OPV device is affected by recombination when they are transferred to the electrodes, more specially if the exact material acts as an ambipolar transport medium for both holes and electrons [59]. The interaction of electrons and holes may be very slow due to the travel speed known as the drift velocity, that which limits the current flow [60].

#### 2.1.3.4 Charge collection

An electrode material having a very low work function (Al or Ca), has charges in which the hole/electron often have to break the potential barrier of a thin oxide layer. In addition, the formation of a blocking contact between the metal and the semiconductor and the quality of the donor/acceptor interface could prohibit charge transport through germinate recombination [61]. This effect is especially aggravated when donor/acceptor domains are formed on the cathode and anode, respectively [52, 60]. The collection of the charge carriers at the electrode is achieved by a transparent conducting oxide (TCO) such as ITO and a hole transport layer PEDOT:PSS (which is a charged conducting polymer at the ITO side.) which provide the required ohmic contact [62].

### 2.1.4 Reflection losses

Reflection losses may be really significant, but there less investigation in these materials. Systematic studies of photovoltaic materials are required to estimate the absorption

and reflective losses. at the interface or outward layers. The non-reflection coatings are used initially in inorganic devices may also be proved resourceful, If there are other losses like recombination, it becomes useless [63, 64].

## 2.2 Photoluminescence

Photoluminescence (PL) of noble metal and metal nanostructures has brought a great attraction in research [65]. The elastic scattering of light in solid state material is a useful technique to investigate the optical properties of matter. This is especially critical in areas where highly coherent light sources are used to probe the medium to emit secondary light that carries information on the electronic properties of matter. This is photoluminescence whose efficiency is dependent on the type of interband transition. Metal photoluminescence is produced from recombination of photoexcited core holes radiation and conduction band electrons [66].

The radiative recombination in noble metals, arises from transitions between electrons in the *sp* conduction band and holes in the *d*–band generated by optical excitation [67]. Photon distribution is influenced by two factors. The first is due to the optics and the final density of states for the exiting photons. This is off-set by a d-band density of states factor increasing as the number of available d-states increase [68].

For example, let us consider the radiative recombination of an *s*–electron and a *d*–hole inside a spherical NPs which has a radius that is less than the wavelength $\Gamma$ of the radiation. The *d*–holes in noble metals appear to be strongly localized, this process is considered as radiation of a dipole located at the *d*–hole position *r*. Radiative decay rate of such a dipole, $4dr$, will enhance relatively to the free–space radiative decay rate, $\Gamma dr$, through the local field factor [69].

Rare-earth (RE)/Lanthanides elements are elements spanning in group III in the periodic table. With an electronic configuration Ar $4f^{n-1}$ in which the *f* levels determines the valency states or lead to excellent luminescence properties [70]. These excellent optical properties of RE enable them to be used in numerous photonic applications. Basic devices requires a RE ions concentrations varying between tens and several thousand parts per million (ppm), giving in a devices that of one to tens meters long like

optical fibers and channel waveguides , respectively [71].

Optical devices, require the localization of the RE ions to be localised at the center of the core for a maximum power gain per unit area. Such that, there's transaction restraint and the concentration of RE ions. To obtain a confined structure, a higher concentration of RE ions is required [21, 72].

Exclusive features of RE ions are outlined below [71]:

- They emit and absorb at about narrow wavelength range.
- The absorption and emission wavelengths are dependent on the host material.
- The transition intensities are weak.
- The lifetimes are long for metastable states.
- The quantum efficiencies are high, but not in aqueous solutions.

The above mentioned properties enables RE ions application in diverse optical applications such as devices with low scattering losses (glass or single-crystal hosts). In cases where the application of crystalline materials are considered for reasons such as better thermal conductivities or higher peak cross–sections. The utility of ceramic glasses and absorption spectra and broader emission provision has led to higher applications for the use of RE doped glasses, eventually it has limitation for particular host glass composition [73].

RE ions can either be divalent or trivalent ions in solids. They have electronic configuration of Ar $4f^N 5s^2 5p^6$ and $4f^{N-1} 5s^2 5p^6$, respectively. Trivalent RE ions are the ones that have the most common valence state while divalent RE ions are the ones incorporated in crystals [74].

The outermost electrons in these ions are not the 4f electrons (which are weakly perturbed by surrounding charges of the atoms and are shielded by the electronic shells with larger radial extension from the external fields). However the 4f levels are responsible for the absorption or emission in solids owing to the atomic structure [21, 75].

The energy levels for a free RE ion are explained by the interactions between the 4f electrons. The notation for these energy levels is given by Russell-Saunders notation $^{2S+1}L_J$, which accounts for the spin-spin coupling, the orbit-orbit coupling and the spin-orbit coupling, where L is the sum of the orbital angular momenta, J is the total angular momentum of the atom and S is the total spin [76, 77]. The Hamiltonian for the embedded RE ions is thus given as

$$H = \frac{\hbar^2}{2m}\Sigma_{i=1}^{N}\Delta_i - \Sigma_{i=1}^{N}\frac{Z^*e^2}{r_i} + \Sigma_{i,j}^{N}\frac{e^2}{r_{ij}} + \Sigma_{i=1}^{N}\zeta(r_i)s_i \cdot l_i \tag{2.7}$$

where the first and second terms in the Hamiltonian are spherically symmetric. The spherical symmetry doesn't lift any of the degeneracies within the 4f electron configuration, and can thus be neglected. The third and fourth terms represents the mutual Coulomb interaction of the 4f electrons with their spin-orbit interaction, which are capable for the 4f electron energy levels structure [78].

Figure 2.4 shows the schematic of the energy levels of the triply charged RE ions. These ions are isolated and are partially filled 4f orbitals.

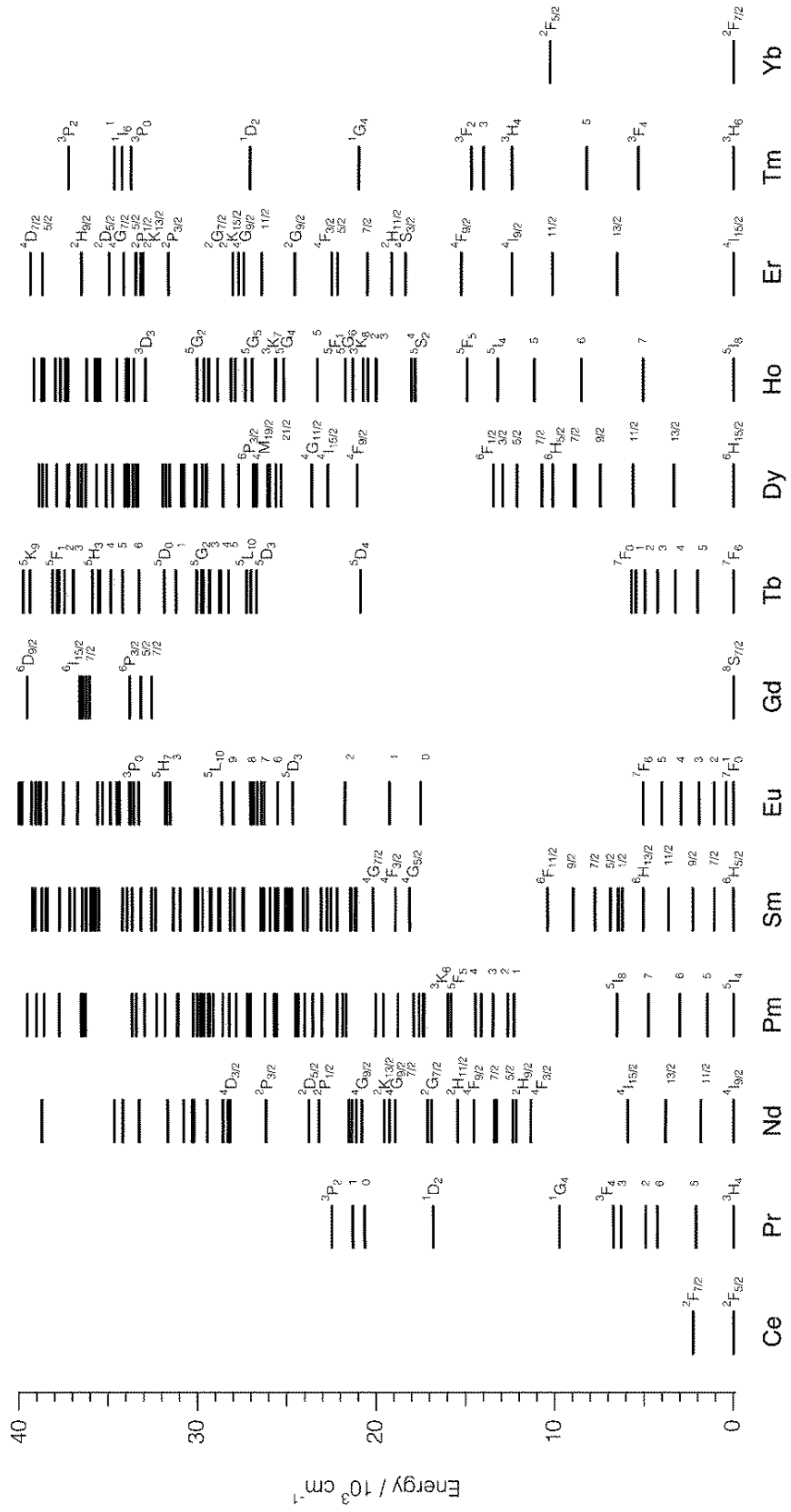



**Figure 2.4:** Energy levels of triply charged lanthanide ions [79]

Emission is predominantly caused by optical transitions in the f-manifold ($Gd^{3+}$ ($4f^7$), $Tb^{3+}$ ($4f^8$) and $Eu^{3+}$ ($4f^7$)). The 4f-electrons are protected from the chemical domains and retains their atomic character. Broad emission bands are known for a number of RE ions. Ions such as $Eu^{2+}$ and $Ce^{3+}$ are prominent examples, where optical emission arises from 5d to 4f transitions [80]. The emission spectra having broad bands is due to the chemical bonding nature of electrons. All of these transition are allowed quantum mechanically and consequently have fast lifetimes (a few $\mu s$ or less) [79, 71].

# Chapter 3

# Theoretical frame work

In this chapter a theoretical framework for surface plasmon resonance will be discussed in detail, using Maxwell's equations and the Drude-Sommerfeld model. We also provide the theoretical treatment of the dielectric function of metal NPs of diverse shapes and sizes.

## 3.1 Plasmonics

### 3.1.1 Surface plasmon condition

A classical approach to define the surface plasmon resonance effect is considered. The optical properties of metals can be explained by a frequency dependent complex dielectric function. These properties are determined by the conduction electrons which move freely within the bulk of the material and by the interband excitations due to the bound electrons in the metal [81]. Plasmons are collective electronic excitations at the interface of a metal and a dielectric material. Since this excitation is localised at the interface they can also be referred as surface plasmon (figure 3.1).

The conditions for the existence of surface plasmons is derived by solving the Maxwell's

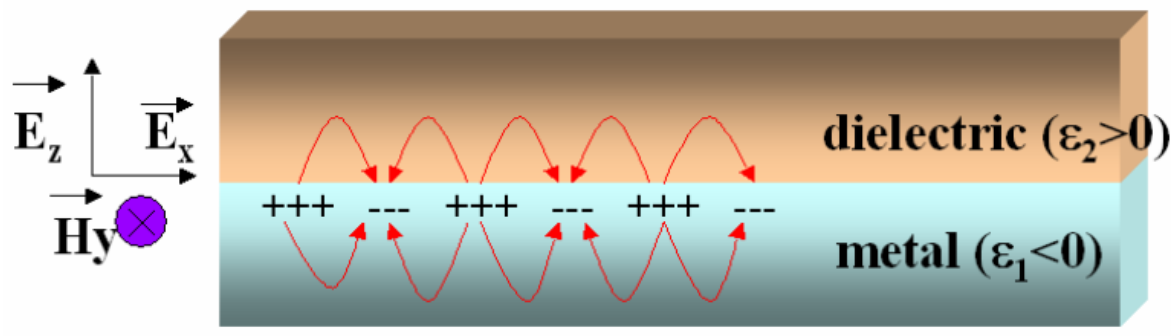



**Figure 3.1:** Two media with dielectric function separated at interface [82]

equations under specific boundary conditions. Suppose two semi-infinite media characterized by a metal and a dielectric of dielectric functions $\varepsilon_1$ and $\varepsilon_2$, respectively are considered. If they are in contact at the interface $z = 0$, then the appropriate Maxwell's equations become:

$$\nabla \times \vec{H} = \varepsilon_i \frac{1}{c} \frac{\partial}{\partial t} \vec{E} \tag{3.1}$$

$$\nabla \times \vec{E} = -\frac{1}{c} \frac{\partial}{\partial t} \vec{H} \tag{3.2}$$

if $\varepsilon_i$ is isotropic then

$$\nabla \cdot \varepsilon_i \vec{E} = 0 = \vec{\nabla} \cdot \vec{E} \tag{3.3}$$

$$\nabla \cdot \vec{H} = 0 \tag{3.4}$$

where $\vec{E}$ is the electric field, $\vec{H}$ is the magnetic field and $i$ is the index used to represent the two media (metal or dielectric). The medium is indexed as follows: if $z < 0$ then $i = 1$ and also if $z > 0$, $i = 2$. (See figure 3.1)

At $z = 0$, the fields decay into a positive and negative in the $z$ direction. We assume

that there is a propagation along the $x$ axis [83], then

$$\vec{E} = (\vec{E}_x, 0, \vec{E}_z)e^{-k_i|z|}e^{i(q_i x - \omega t)}) \tag{3.5}$$

$$\vec{H} = (0, \vec{E}_y, 0)e^{-k_i|z|}e^{i(q_i x - \omega t)}) \tag{3.6}$$

In which $q_i$ is the magnitude of a wave vector parallel to the surface (interface).

Now inserting equations 3.5 and 3.6 into equations 3.1-3.4 we find that

$$k_1\vec{H}_{1_y} = +\frac{\omega}{c}\varepsilon_1\vec{E}_{1_x} \tag{3.7}$$

$$k_2\vec{H}_{2_y} = -\frac{\omega}{c}\varepsilon_2\vec{E}_{2_x} \tag{3.8}$$

Where $k_i$ is given as

$$k_i = \sqrt{q^2 - \varepsilon_i\frac{\omega^2}{c^2}} \tag{3.9}$$

Now invoking the boundary conditions governing the continuity at the interface for components of vector $\vec{E}$ and $\vec{H}$ parallel to the interface [84]. From $\vec{E}_{1_x} - \vec{E}_{2_x} = 0$ (the boundary condition at plane $z = 0$) we find that

$$\frac{k_1}{\varepsilon_1}\vec{H}_{1_y} + \frac{k_2}{\varepsilon_2}\vec{H}_{2_y} = 0 \tag{3.10}$$

and at the same time we have

$$\vec{H}_{1_y} - \vec{H}_{2_y} = 0 \tag{3.11}$$

This is not possible if the coefficient determinant is zero,

$$\frac{\varepsilon_1}{k_1} + \frac{\varepsilon_2}{k_2} = 0 \tag{3.12}$$

$$\implies \frac{k_1}{k_2} = -\frac{\varepsilon_1}{\varepsilon_2} \tag{3.13}$$

This is the condition for the appearance of surface plasmon resonance. This system condition gives equations with non-trivial solutions, which shows the dispersion relation by connecting the frequency of the p-polarized wave and its wavenumber $k$.

The boundary condition also implies the continuity of 2D wave vectors. Now substituting equation 3.9 into 3.12 and let $k_1 = k_2 = k$ and make $q(\omega)$ the subject of the formula we have:

$$q(\omega) = \frac{\omega}{c}\sqrt{\frac{\varepsilon_1\varepsilon_2}{\varepsilon_1 + \varepsilon_2}} \tag{3.14}$$

In this case $\omega/c$ is the magnitude of wave vector, $\varepsilon_2$ is the dielectric function of the metal.

### 3.1.2 Energy dispersion of metalic nanoparticles

The Drude-Sommerfeld model has the following modifications:

1. It treats electrons using Fermi Dirac statistics.
2. Recognizes that their energies are discrete hence they can be considered as a particle in a box of constant energy.
3. Uses Pauli exclusion's principle to distribute them in the available energy states

Considering only the effect of the free electrons and using the Drude-Sommerfeld model for the free electron gas we have:

$$m_e \frac{\partial^2 r}{\partial t^2} + m_e \Gamma \frac{\partial r}{\partial t} = e E_0 e^{-i\omega t} \tag{3.15}$$

where $e$ is the electric charge (for free electrons), $m_e$ is the effective mass of the free electrons, $E_0$ is the amplitude of the applied field and $\omega$ is the frequency of the applied electric field. $\Gamma$ is the damping term which is proportional to the ration of the Fermi velocity and the electron mean free path between scattering ($\Gamma = v_f/l$). The cumulative effect of all free electron dipole moment $\mu = er$ ($r$ is the displacement) results in macroscopic polarization $P$ per unit volume

$$P = n\mu \tag{3.16}$$

$$= ner \tag{3.17}$$

$n$ is the number of electrons per unit volume and knowing that the macroscopic polarization can also be expressed in terms of the electronic susceptibility $\chi_e(\omega)$ as:

$$P(\omega) = \varepsilon_0 \chi_e(\omega) E(\omega) \tag{3.18}$$

and the frequency-dependent dielectric function of the metal assumes the form:

$$\varepsilon(\omega) = 1 + \chi_e(\omega) \tag{3.19}$$

using the ansatz $r(t) = r_0 e^{-i\omega t}$ and solving for 3.15 leads to

$$m_e(-r_0\omega^2 e^{-i\omega t}) + m_e\Gamma(-ir_0\omega e^{-i\omega t}) = eE_0e^{-i\omega t} \tag{3.20}$$

$$-m_e r_0 e^{-i\omega t}(\omega^2 + i\Gamma\omega) = eE_0e^{-i\omega t} \tag{3.21}$$

$$-m_e r_0(\omega^2 + i\Gamma\omega) = eE_0 \tag{3.22}$$

combining equations 3.16, 3.18 and 3.19 gives the frequency dependent electric field is in the form:

$$E_0 = \frac{ner_o}{[\varepsilon(\omega) - 1]\varepsilon_0} \tag{3.23}$$

now substituting 3.23 into 3.22 yields the frequency dependent dielectric function in the following form:

$$\varepsilon_{Drude}(\omega) = 1 - \frac{e^2 n}{m_e\varepsilon_0}\frac{1}{\omega^2 + i\Gamma\omega} \tag{3.24}$$

where $\omega_p = \sqrt{\frac{e^2 n}{m_e\varepsilon_0}}$ is the plasma frequency (measuring plasma oscillations of the electrons),

hence

$$\varepsilon_{Drude}(\omega) = 1 - \frac{\omega_p^2}{\omega^2 + i\Gamma\omega} \tag{3.25}$$

which can be decoupled into real part and imaginary parts as:

$$\varepsilon_{Drude}(\omega) = 1 - \frac{\omega_p^2}{\omega^2 + \Gamma^2} + i\frac{\Gamma\omega_p^2}{\omega(\omega^2 + \Gamma^2)} \tag{3.26}$$

Using $\omega_p = 1.380 \times 10^{15}\ s^{-1}$ and $\Gamma = 4.053 \times 10^{15}\ s^{-1}$ which are values for silver, we have plotted the real and imaginary part of equation 3.26 (figure 3.2). In order to plot this dispersion relation we assume that $\varepsilon_e = 1$ ($\varepsilon_e$ is the relative permittivity of free space) and independent of $\omega$.

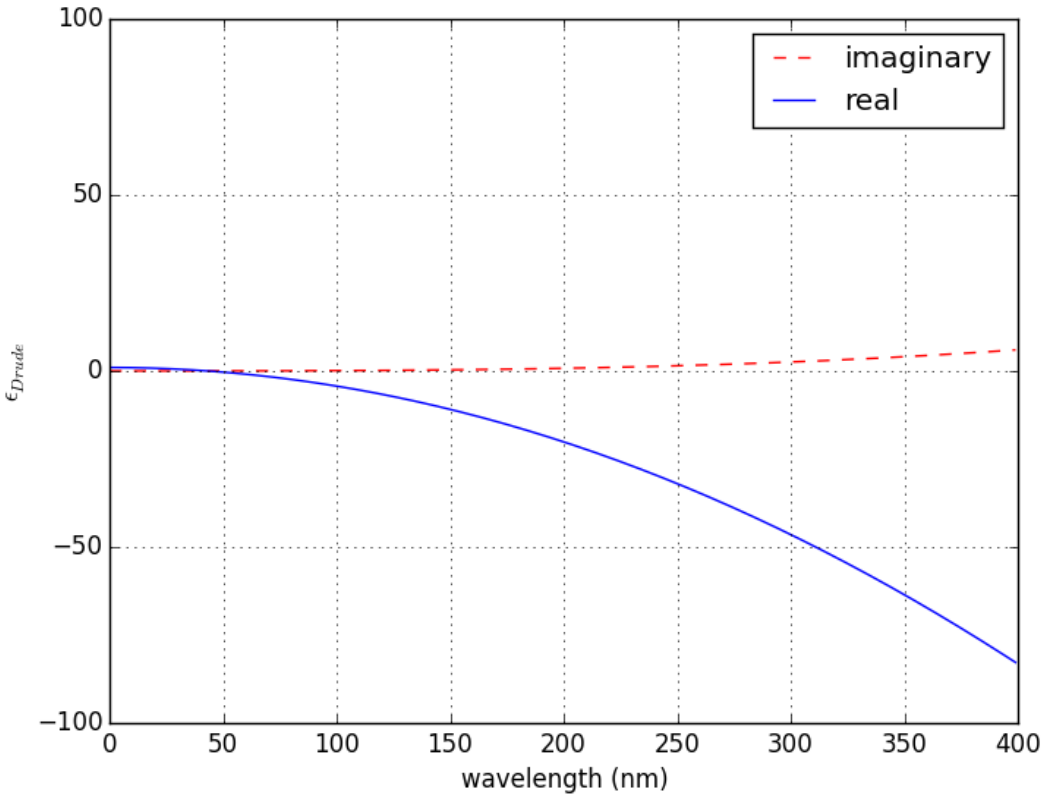



**Figure 3.2:** Real and imaginary part of the dielectric constant for silver according to the Drude-Sommerfeld free-electron model

In figure 3.2 the real part of the dielectric constant is negative because of the optical characteristics of noble metals (in this case silver). Light can only penetrate by a very small distance, having a negative dielectric constant gives a strong imaginary part of the refractive index $n = \sqrt{\varepsilon}$ . The imaginary part of $\varepsilon$ describes the dissipation of energy associated with the motion of electrons in metallic particles [85].

Substituting equation 3.25 into equation 3.14 we have

$$q(\omega) = \frac{\omega}{c}\sqrt{\frac{\omega^2 - \omega_p^2}{2\omega^2 - \omega_p^2}} \tag{3.27}$$

Equation 3.27 is the corresponding dispersion relation the particles.

### 3.1.3 Numerical modelling for scattering and absorption cross-section

#### 3.1.3.1 Absorption and scattering definition

Consider light scattering by small perfectly conducting sphere of radius $a$ which has the electric dipole $p = 4\pi\varepsilon_o a^3 E$ and the magnetic dipole moment $m = -2\pi a^3 H$ (figure 3.3).

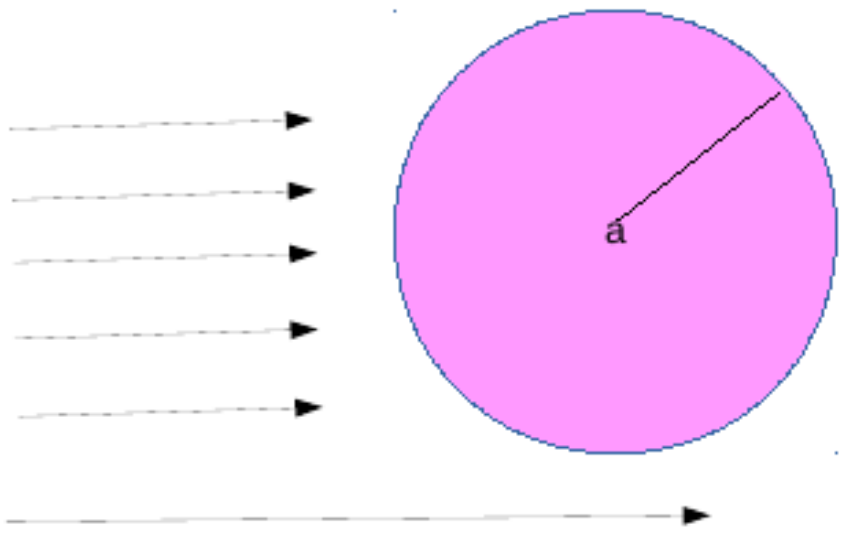



**Figure 3.3:** A sphere of radius $a$ exposed to the E field

The Laplace's equation for potential $\Phi$, is given by $\nabla^2\Phi = 0$, and the electric field is $E = -\nabla\Phi$. The Laplace equation may be expressed in spherical coordinates $(r, \theta, \varphi)$ as follows:

$$\nabla^2\Phi(r,\theta,\varphi) = \frac{1}{r^2 sin\theta}[sin\theta\frac{\partial}{\partial r}(\frac{r^2\partial}{\partial r})] + \frac{\partial}{\partial\theta}(sin\theta\frac{\partial}{\partial\theta}) + \frac{1}{sin\theta}\frac{\partial^2}{\partial\varphi^2}]\Phi(r,\theta,\varphi) = 0 \quad (3.28)$$

It has a solution in the following form:

$$\Phi(r,\theta,\varphi) = \sum_{l,m} b_{l,m} \cdot \Phi_{l,m}(r,\theta,\varphi) \quad (3.29)$$

where $b_{l,m}$ are the constant coefficients to be determined from the boundary condition. After evaluation of the boundary conditions [86] we have:

$$\Phi_{in} = -\vec{E}_o\frac{3\varepsilon_2}{\varepsilon_1 - 2\varepsilon_2}rcos\theta \quad (3.30)$$

$$\Phi_{out} = -\vec{E}_o rcos\theta + E_o\frac{\varepsilon_1 - \varepsilon_2}{\varepsilon_1 + 2\varepsilon_2}a^3\frac{cos\theta}{r^2} \quad (3.31)$$

see Jackson [86] and Novotny [85] for full details.

$\vec{E}_o$ is the amplitude of the external electric field, $\varepsilon_2$ and $\varepsilon_1$ are the dielectric permittivity of and the surrounding medium of the NPs, respectively, $\omega$ is the excitation frequency, $r$ is the radial coordinate for both functions. Substituting 3.30 into $\vec{E} = -\nabla\Phi$ ,the electric field is now expressed in the following form:

$$\vec{E}_{in} = \vec{E}_o\frac{3\varepsilon_2}{\varepsilon_1 - 2\varepsilon_2}(n_r cos\theta - n_\theta sin\theta) \quad (3.32)$$

$$= \vec{E}_o\frac{3\varepsilon_2}{\varepsilon_1 - 2\varepsilon_2}n \quad (3.33)$$

$$\vec{E}_{out} = \vec{E}_o(n_r cos\theta - n_\theta sin\theta) + \vec{E}_o \frac{\varepsilon_1 - \varepsilon_2}{\varepsilon_1 + 2\varepsilon_2} \frac{a^3}{r^3}(n_r 2cos\theta + n_\theta sin\theta) \tag{3.34}$$

From equation 3.34 the second term is known as the scattered field and is similar to electrostatic field of a dipole $\mu$ that is located at the center of the sphere [85]. The dipole induced by an external field is thus given by

$$\mu = \varepsilon_2 \alpha(\omega) E_o \tag{3.35}$$

which implies that the polarizability ($\alpha(\omega)$) is of the following form:

$$\alpha(\omega) = 4\pi\varepsilon_o a^3 \frac{\varepsilon_1(\omega) - \varepsilon_2}{\varepsilon_1(\omega) + 2\varepsilon_2} \tag{3.36}$$

The electric field of the oscillating dipole moment in the near field zone is approximated as

$$E(r,t) = \frac{1}{4\pi\varepsilon_o}[3n(n \cdot \mu) - \mu]\frac{e^{i\omega t}}{r^3} \tag{3.37}$$

where $n$ is the refractive index.

The scattering cross-section of the sphere is calculated by the ratio between the total radiated power of the sphere's dipole and the intensity of the exciting plane wave. Hence we have [85, 87]

$$\sigma_{scatt} = \frac{k^4}{6\pi\varepsilon_o^2}|\alpha(\omega)|^2 \tag{3.38}$$

where k is wavevector in the surrounding medium.

From the incident beam, power is removed not only because of the particle's scattering,

but also because of absorption. The sum of absorption and scattering equals extinction. To calculate the power which is dissipated inside the particle we use the Poynting's theorem. The power dissipated by a point dipole is [85]:

$$P_{abs} = (\frac{\omega}{2}) Im\{\mu \cdot E_0^{\star}\} \tag{3.39}$$

where $\mu = \varepsilon_2 \alpha E_0$ ($\varepsilon_2$ is real).

For the absorption cross-section we find that

$$\sigma_{abs} = \frac{k}{\varepsilon_o} Im\{\alpha(\omega)\} \tag{3.40}$$

#### 3.1.3.2 Finite difference time domain (FDTD) approach to calculate scattering and absorption cross-section

A better approach is to calculate the optical scattering and absorption cross-section of silver NPs using the Finite difference time domain (FDTD) codes. Finite difference time domain is a numerical technique used to model electrodynamic problems. It propagates approximate solutions to the Maxwell's equations. FDTD solutions covers a huge frequency range with a single simulation run, and the method also treats non-linear material properties in a natural way [88].

Among many applications of FDTD are also the calculation of absorption and scattering cross section of Ag NPs with diverse size distribution, a feature that is essential for plasmonics [89]. A description of the conceptual basis is found in [89, 90].

Absorption and scattering cross sections are calculated using MEEP, which is an open-source implementation of the FDTD algorithm. MEEP stands for MIT Electromagnetic Equation Propagation. It is accessible online at $http://ab-initio.mit.edu/meep$. MEEP has interesting features, such as: non-linear,arbitrary anisotropic and disper-

sive electric and as well magnetic media, such as different boundary conditions including perfectly matched layers (PML), distributed-memory parallelism (cylindrical and cartesian coordinates) and a very flexible output and field computations.

The package includes interesting features, like a frequency-domain solutions, which exploits the time-domain coding, advanced signal processing to analyse resonant modes and integrated optimization facilities and many more [90].

To compute the transmitted or scattered power in a particular direction as a function of the frequency of incident light, one wishes to compute the integral of the Poynting flux for a given sphere S:

$$P(\omega) = Re \oint_S \oint_S E(\omega, r) \times H(\omega, r)\, dA \tag{3.41}$$

$E$ and $H$ are defined for spatial points $r$ and frequencies $\omega$. FDTD usually simulates the propagation in space and time for the fields. The power spectrum $P(\omega)$ can be thus calculated by transforming the fields into frequency domain using the following Fourier transform:

$$E = \frac{1}{\sqrt{2}} \sum_n e^{i\omega n \Delta t} E(n\Delta t)\Delta t \tag{3.42}$$

which is also known as the discrete-time Fourier transformation [89].

#### 3.1.3.3 The Drude-Lorentz model on FDTD

Dielectric materials are implemented on MEEP in terms of a frequency and spatial position dependent, dipole moment $\mu$ and dielectric function $\varepsilon$.

The dielectric functions $\varepsilon(\omega)$ are given due to the contribution of free and bound electrons

$$\varepsilon(\omega) = \varepsilon_\infty + \Sigma_n \frac{\sigma_n \omega_n}{\omega_n^2 - \omega^2 - i\omega\Gamma_n} \tag{3.43}$$

where $\varepsilon_\infty$ is the instantaneous dielectric response, $\sigma_n$ is an electric conductivity as a position function specifying the strength of the $n$ resonance and $\omega_n$ and $\Gamma_n$ are the resonance and damping frequency, respectively.

The optical excitation in metals can be defined from the Drude-Lorentz model:

$$\varepsilon_{Drude-Lorentz} = \varepsilon_{Drude} + \varepsilon_{Lorentz} \tag{3.44}$$

where the Drude model represents the contribution due to free electrons, while the Lorentz model describes the bound electrons, given below

$$\varepsilon_{Drude} = 1 - \frac{\omega_p^2}{\omega(\omega - i\Gamma)} \tag{3.45}$$

$$\varepsilon_{Lorentz} = \Sigma_n \frac{\omega_p^2}{\omega_n^2 - \omega^2 + i\omega\Gamma_n} \tag{3.46}$$

and $\Gamma$ is the damping term

Implementing the Drude-Lorentz model in FDTD, we consider the polarization equa-

tion in a single resonance approach

$$\vec{P} = \varepsilon_o \chi(\omega) \vec{E}(\omega) \tag{3.47}$$

and

$$\chi(\omega) = \frac{\chi_o \omega_n}{\omega_n^2 - \omega^2 + i\omega\Gamma} \tag{3.48}$$

so now we have polarization as

$$\vec{P} = \varepsilon_o \frac{\chi_o \omega_o}{\omega_n^2 - \omega^2 + i\omega\Gamma} \vec{E}(\omega) \tag{3.49}$$

Taking the Fourier transform of the above equation, gives the differential equation of the following form

$$\frac{\partial^2 \vec{P}}{\partial t^2} + \Gamma \frac{\partial \vec{P}}{\partial t} + \omega_n \vec{P} = \varepsilon_o \chi_o \omega_n^2 \vec{E}(\omega) \tag{3.50}$$

and let $\frac{\partial \vec{P}}{\partial t} = J$ so now have

$$\frac{\partial \vec{J}}{\partial t} + \Gamma \vec{J} + \omega_n \vec{P} = \varepsilon_o \chi_o \omega_n^2 \vec{E}(\omega) \tag{3.51}$$

Equation 3.50 and 3.51 are solved numerically together with the following equation with in FDTD

$$\frac{\partial \vec{H}_x}{\partial z} - \frac{\partial \vec{H}_z}{\partial x} = \frac{\partial D_y}{\partial t} = \frac{\partial \vec{E}}{\partial t} \frac{\partial \vec{P}_y}{\partial t} \tag{3.52}$$

which supports simulations in 2D and 3D.

**NB**: $\vec{H}_{x,y}$ are real quantities.

## 3.2 Simulations of the absorption and scattering cross-section of Ag NPs with MEEP

As discussed before, to calculate the amount of light a particle absorbs/scatters, we consider the Poynting vectors and integrate it over a suitable domain [91].

Consider a surface $A$ which encloses a volume $V$. We can also choose a local normal vector, $\hat{n}$, at every point of $A$, such that it has a positive magnitude as it faces outwards. The rate at which electromagnetic energy is transferred through this surface is given by $\vec{W} = -\oint \vec{S} \cdot \hat{n} dA$, where $\vec{S}$ indicates the time-averaged Poynting vector. A time-averaged Poynting vector indicates the average rate of transfer of electromagnetic energy per unit area and is given by $\vec{S} = \frac{1}{2} Re\{\vec{E} \times \vec{H}^*\}$. A negative $\vec{W}$ indicates energy transferred out of the surface and positive $\vec{W}$ indicates transfer of energy into the surface.

Assume a particle of arbitrary geometry enclosed by $A$, as excited by light of some frequency and polarization. At any point on $A$, the time-averaged Poynting is given by

$$\vec{S} = \frac{1}{2} Re\{\vec{E} \times \vec{H}^*\} \tag{3.53}$$

where $\vec{S}$ is a sum of three terms:

$$\vec{S} = \vec{S}_{inc} + \vec{S}_{scat} + \vec{S}' \tag{3.54}$$

$\vec{S}_{inc}$, $\vec{S}_{scat}$ and $\vec{S}'$ are the time-averaged Poynting vector due to incident light, of the scattered light and due to extinction of the incoming light, respectively. They also can be expressed in terms of the scattered, and the incident electric and magnetic fields, respectively:

$$\vec{S}_{scat} = \frac{c}{8\pi} Re\{\vec{E}_{scat} \times \vec{H}^*_{scat}\}, \tag{3.55}$$

$$\vec{S}_{inc} = \frac{c}{8\pi} Re\{\vec{E}_{inc} \times \vec{H}^*_{inc}\}, \tag{3.56}$$

$$\vec{S}' = \frac{c}{8\pi} Re\{\vec{E}_{inc} \times \vec{H}^*_{scat} + \vec{E}_{scat} \times \vec{H}^*_{inc}\} \tag{3.57}$$

where the electric field $\vec{E}$ and magnetic field $\vec{H}$ can be written as

$$\vec{E} = \vec{E}_{inc} + \vec{E}_{scat} \tag{3.58}$$

$$\vec{H} = \vec{H}_{inc} + \vec{H}_{scat} \tag{3.59}$$

The rate at which energy comes into the surface $A$ is given by

$$\vec{W}_{inc} = -\oint (\vec{S}_{inc} \cdot \hat{n}) dA \tag{3.60}$$

The rate at which energy gets scattered and transferred out of $A$ is given

$$\vec{W}_{scat} = -\oint (\vec{S}_{scat} \cdot \hat{n}) dA \tag{3.61}$$

The rate at which energy is absorbed by the particle can be expressed in the following

form:

$$\vec{W} = -\vec{W}_{abs} = \vec{W}_{inc} + \vec{W}_{scat} + \vec{W}' \tag{3.62}$$

since the conservation of energy requires that the net outward energy through the surface A is in the same rate at which is absorbed [91].

As part of the light also gets absorbed by the particle. If we assume that a surface $A$ is completely surrounding the particle, so there is rate at which scattered energy ($W_{scat}$) is transferred across the surface, and is given by the integral of Poynting vector (which is electromagnetic energy/unit area, $W/m^2$) over the whole surface.

Total power $\mathbf{P}$ on the surfaces is then calculated by;

$$\mathbf{P}_{scat}(\omega) = Re\left[\hat{n} \cdot \oint_A \vec{E}_{scat}(\omega) \times \vec{H}^*{}_{scat}(\omega).d^2A\right] \tag{3.63}$$

$$\mathbf{P}_{abs}(\omega) = Re\left[\hat{n} \cdot \oint \vec{E}(\omega) \times \vec{H}^*(\omega).d^2A\right] \tag{3.64}$$

Where $\hat{n}$ is the outward normal direction to the surface and

$$\vec{E}_{scat}(\omega) = \vec{E}(\omega) - \vec{E}_{inc}(\omega) \tag{3.65}$$

$$\vec{H}_{scat}(\omega) = \vec{H}(\omega) - \vec{H}_{inc}(\omega) \tag{3.66}$$

Using the expression of the scatter and absorption we calculate the scattering and

absorption cross sections as:

$$\sigma_{scat}(\omega) = \frac{\mathbf{P}_{scat}(\omega)}{I_{inc}(\omega)} \tag{3.67}$$

$$\sigma_{abs}(\omega) = \frac{\mathbf{P}_{abs}(\omega)}{I_{inc}(\omega)} \tag{3.68}$$

where $I_{inc}(\omega)$ is the intensity of incident light. Equations 3.63 and 3.65 - 3.68 give the quantitative expression for the scattering and absorption cross-sections.

#### 3.2.0.4 Units conversion on MEEP

The coefficients are in electron volts eV, since MEEP operates in dimensionless units (e.g speed of light $c = \hbar = 1$ )

$\Leftrightarrow$ The conversion from Joules to eV is given by first converting eV to angular frequency given by $results/\hbar$

$\Leftrightarrow$ Frequency $f$ (corresponds to the time dependent term $e^{i2\pi ft}$) is expressed in $c/a$, where $a$ is the length scale chosen

$\Leftrightarrow$ Then convert angular frequency to dimensionless units: but

$results/\hbar = results/(2\pi c/a)$

then

$$\chi_o = \frac{\chi_{eV}}{\hbar}\frac{a}{2\pi c} = \chi_{eV}\frac{a}{hc} \tag{3.69}$$

## 3.3 Waveguides for applications in photonics

A waveguide is a elementary element which interconnects the different optical apparatus of the optical integrated circuit in which optical waves travel in prominent optical modes [92]. These modes are related to a spatial distribution of optical energy in one

or more dimensions. The commonly used dielectric waveguide is the optical fibre which mostly has a circular cross-section [93]. In contrast, the waveguides of interest in the integrated optics constitute planar structures, like planar films [94]. Our discussion is thus focused on planar waveguides even though most of the fundamentals properties are appropriate to all types of dielectric waveguides.

### 3.3.1 Waveguide structure

- The standard structure of dielectric waveguides contains a longitudinal extended high-index optical medium, known as the core. The core is transversely surrounded with low-index media, namely, the cladding
- An optical wave that is guided transmits in the longitudinal direction.
- In contrast the transverse profile of waveguides, are determined by its dielectric constant $\varepsilon(x, y)/\varepsilon_0$ which are independent of the longitudinal (z) or propagation direction.
- Optically isotropic media waveguide, are characterized waveguides with single spatial dependent transverse outline of the index of refraction n(x, y).

### 3.3.2 Boundary condition for electromagnetic fields.

The boundary conditions for the electromagnetic fields are given below [95]:

- Tangential components are continuous for the electric fields such that $E_1 = E_2$.
- Tangential components are continuous for the magnetic fields when no current flows on the surface, such that $H_1 = H_2$.

- When there is no charge on the surface, the normal components of the electric flux densities are continuous such that $D_1 = D_2$. However the presence of a charge on the surface, leads to discontinuity in the electric flux densities as follows: $D_1 - D_2 = \rho_S$, where $\rho_S$ is the surface charge density.
- Normal components of the magnetic flux densities are continuous such that $B_1 = B_2$.

### 3.3.3 Optical waveguides

A planar waveguide in a transverse direction, has one optical confinement, in which the core is sandwiched between cladding layers only in the x direction, having an index profile n(x). The planar waveguide core is called a thin film, whilst the lower and upper cladding layers are called the substrate and the cover respectively [96].

Assuming that the electromagnetic field oscillates with a singular frequency $\omega$, the electromagnetic field be represented as [86]

$$E(r,t) = Re\{\bar{E}(r)e^{(-i\omega t)}\} \tag{3.70}$$

$$H(r,t) = Re\{\bar{H}(r)e^{(-i\omega t)}\} \tag{3.71}$$

$$D(r,t) = Re\{\bar{D}(r)e^{(-i\omega t)}\} \tag{3.72}$$

$$B(r,t) = Re\{\bar{B}(r)e^{(-i\omega t)}\} \tag{3.73}$$

From the Maxwell's equation follows:

$$\nabla \times E = -i\omega\mu_0 H \tag{3.74}$$

$$\nabla \times H = i\omega\epsilon E \tag{3.75}$$

$$\nabla \cdot H = 0 \tag{3.76}$$

$$\nabla \cdot (\epsilon_r E) = 0 \tag{3.77}$$

where $\mu_o$ and $\epsilon_o$ are the permeability and permittivity of free space, respectively.

Taking account of equation 3.74 and invoking the curl ($\nabla\times$) on both sides leads to:

$$\nabla \times (\nabla \times E) = -i\omega\mu_0(\nabla \times H) \tag{3.78}$$

$$= \omega^2\varepsilon\mu_o E \tag{3.79}$$

The left side of equation 3.79 is written using the vector identity as

$$\nabla \times (\nabla \times E) = \nabla(\nabla \cdot E) - \nabla^2 E \tag{3.80}$$

where $\nabla^2$ is the Laplician defined for the rectangular co-ordinate system as

$$\nabla^2 = \frac{\partial^2}{\partial x^2} + \frac{\partial^2}{\partial y^2} + \frac{\partial^2}{\partial z^2} \tag{3.81}$$

and Gauss law 3.77 can also be written as

$$\nabla \cdot (\epsilon_r E) = \nabla \epsilon_r \cdot E + \epsilon_r \nabla \cdot E = 0 \tag{3.82}$$

Therefore the electric field is now:

$$\nabla \cdot E = -\frac{\nabla \epsilon_r}{\epsilon_r} \cdot E \tag{3.83}$$

Substituting equation 3.83 into equation 3.80 we have

$$\nabla \times (\nabla \times E) = -\nabla(\nabla \cdot \frac{\nabla \epsilon_r}{\epsilon_r})E - \nabla^2 E \tag{3.84}$$

then equation 3.79 can be written as

$$-\nabla(\nabla \cdot \frac{\nabla \epsilon_r}{\epsilon_r})E - \nabla^2 E = \omega^2 \epsilon \mu_o E \tag{3.85}$$

### 3.3.4 Transverse magnetic and electric modes in a planar waveguide

Consider a three layer optical waveguide slab in figure 3.4, showing a three layer slab optical waveguide film of thickness d and refractive index $n_f$ is placed between a substrate and a cover (air) material with lower refractive indices $n_s$ and $n_c$, respectively. The regions with $n_s$ and $n_c$, classified as the cladding layers and the region with $n_f$ is the core layer having a higher refractive index than the others ($n_f > n_s \geq n_c$ ).

Clearly from figure 3.4 the tangential field are connected at interface, we may assume that $\partial/\partial y = 0$, if the structure is uniform in the y direction.

A mathematical definition of the mode in the electromagnetic field is a solution of

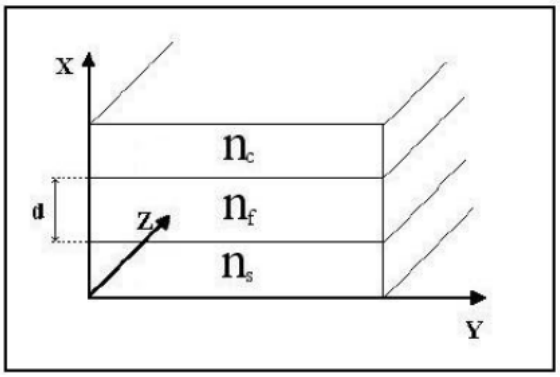



**Figure 3.4:** A three layer slab optical waveguide with refractive indexes, $n_s, n_f, n_c$

Maxwell's wave equation [97] given below

$$\nabla^2 E(r,t) = [n(\hat{r})/c]\frac{\partial^2 E(\hat{r},t)}{\partial t^2} \tag{3.86}$$

where $\hat{r}$ is a vector and $n(\hat{r})$ is the refractive index and c is the speed of light in a vacuum. Using the ansazt $E(\hat{r},t) = E(\hat{r})e^{i\omega t}$ where $\omega$ is the radian frequency in equation 3.86, we have the electric field as

$$\nabla^2 E(\hat{r}) + k^2 n^2(\hat{r})E(\hat{r}) = 0 \tag{3.87}$$

where $k = \omega/c$. Similarly for the magnetic field we have

$$\nabla^2 H(\hat{r}) + k^2 n^2(\hat{r})E(\hat{r}) = 0 \tag{3.88}$$

Equation 3.87 and 3.88 represents the two modes that propagate in a three layer slab optical waveguide. The modes represent the transverse electric (TE) and transverse magnetic (TM) modes, respectively.

For a uniform wave propagating in the $z$ direction, the electric field is $E(\hat{r},t) =$

$E(x,y)e^{i\beta z}$ and $\beta$ is the propagating constant, now we can write equation 3.87 as

$$\frac{\partial^2 E(x,y)}{\partial x^2} + \frac{\partial^2 E(x,y)}{\partial y^2} + [k^2 n^2(\hat{r}) - \beta^2]E(x,y) = 0 \tag{3.89}$$

We assumed that the waveguid is infinite in the $y$ direction. Now, we can expand equation 3.89 according to the layers in figure 3.4 such that we have

$$\frac{\partial^2 E(x,y)}{\partial x^2} + \frac{\partial^2 E(x,y)}{\partial y^2} + [k^2 n_c^2 - \beta^2]E(x,y) = 0 \tag{3.90}$$

$$\frac{\partial^2 E(x,y)}{\partial x^2} + \frac{\partial^2 E(x,y)}{\partial y^2} + [k^2 n_f^2 - \beta^2]E(x,y) = 0 \tag{3.91}$$

$$\frac{\partial^2 E(x,y)}{\partial x^2} + \frac{\partial^2 E(x,y)}{\partial y^2} + [k^2 n_s^2 - \beta^2]E(x,y) = 0 \tag{3.92}$$

The solutions of the above equations are either sinusoidal or exponential functions of x in each of the regions.

# Chapter 4

# Methodology

In this section, the methods used to synthesize and characterize Ag NPs will be technically presented. In addition the fabrication and characterization methods used to establish the properties of waveguides will be discussed in detail.

## 4.1 Synthesis of Ag nanoparticles

The application of the polyol process constitutes a robust and versatile for the synthesis Ag NPs of diverse shapes and sizes. Chemical reduction has a very important role in the synthesis of Ag NPs. A method suggested, based on coordination chemistry, is extended for $Ag^{+}$ stabilization in solution systems. Different ligands of metal ions can be tested, for the stabilization the metal ions and thereby preventing metals to precipitate onto the film surface [98]. The reduction process involves several routes, which have been proposed for the oxidation of DMF, it normally involve the evolution of $H_2$ or $CO_2$ gas [99].

Ag NPs with different sizes and shapes were synthesized through reducing $AgNO_3$ in N,N-dimethylformamide (DMF). DMF was used as a capping agent (**NB:** DMF is harmful so must be handled with care). 2,2 Poly(vinylpyrrolidone) (PVP) aqueous solution was prepared by adding 0.4g of PVP into 20ml of ethyl-glycol (EtG) and PVP

is used as stabiliser to prevent the agglomeration of Ag NPs and EtG oxidises to aldehyd species with an oxidation potential of 1.6 eV and it also temperature dependent, 10 ml of the solution was then added to DMF (80 ml), proceeded by an addition of 10 ml of $AgNO_3$ aqueous solution with a molar concentration of 0.01M. The aqueous solution of $AgNO_3$ was prepared by adding 0.192 g of $AgNO_3$ into 20 ml of EtG, the solution was allowed to mix in the darkroom. The reaction was kept for 3 hours at 100 $^o$C until a dark-brownish solution was obtained. Centrifugation was performed to purify the solution at 14000 rpm for 45 minutes. The resultant mixture was decanted to remove the Ag NPs and there after suspended in $H_2O$.

The concentration and temperature were kept constant at 0.1M and 100$^o$C, respectively. However the reaction times were varied by 10 minutes, 20 minutes and 40 minutes after the initial 3 hours.

**Reduction process of $AgNO_3$ in DMF:**

$AgNO_3$ decomposes when heated

$$2AgNO_3 \rightarrow 2Ag^+ + O_2 + 2NO_2 \tag{4.1}$$

The overall reaction displayed in equation when $Ag^+$ react with DMF ($(CH_3)_2NCOH$) shows the formation of a carbamic acid. The carbamic acid in conjunction with the resulting acidic environment promote the deposition of Ag NPs [100]:

$$(CH_3)_2NCOH + 2Ag^+ + H_2O \rightarrow 2Ag^0 + (CH_3)_2NCOOH + 2H^+ \tag{4.2}$$

if heat is applied, the carbamic acid is decomposed to

$$(CH_3)_2NCOOH \rightarrow (CH_3)_2NH + CO_2 \tag{4.3}$$

## 4.2 Fabrication of Organic photovoltaic device

### 4.2.1 Cleaning of substrate

ITO-coated glass was cut into 1.2 cm x 1.2 cm slices with a WC tip scriber. Then 30% of the cut ITO surface was etched through wet chemistry using zinc paste (mixture of zinc powder and water) and hydrochloric acid (HCl) (with a concentration of 0.2 M). The zinc paste was coated on the ITO glass and then immersed in HCl for a few minutes until the ITO was completely removed. ITO has unique characteristics such as low resistivity of $7.5\times10^{-4}$ $\Omega cm$, high optical transmittance of about 82% to 89% over the visible wavelength region, excellent adhesion to substrates and chemical stability. The samples were then washed with detergents, then rinsed in distilled water. Thereafter the samples were sonicated for 10 minutes in acetone, followed by methanol ultrasonicating for 10 minutes. Finally the samples were sonicated in ethanol and distilled water for 10 minutes again and then dried with purified nitrogen gas (99.999%).

### 4.2.2 Reference solar cell

A reference solar cell was fabricated first by preparing a solution of PCBM ([6,6]-phenyl $C_{61}$-butyric acid methyl ester) by adding 0.5ml of chlorobenzene into 0.010g PCBM and stirring it for 3 hours at room temperature. Similarly a solution of P3HT (Poly(3-hexylthiophene-2,5-diyl)) was prepared with 0.5 ml of chlorobenzene into 0.010g of P3HT under the same condition as PCBM solution. After stirring for 3 hours both solutions were mixed together in 1:1 ratio and stirred for 2 hours at room temperature.

The fabrication of the OPV entailed foremost spin coating PEDOT:PSS [poly (3,4-ethylenedioxythiophene)–poly(styrenesulfonate)] onto ITO glass substrate at 2000 rpm for 1 minute. PEDOT:PSS serves to increase the transport of hole to the anode while

blocking the flow of electrons (PEDOT:PSS solution is purchased as prepared). Afterwards the samples were then annealed on a hot plate for 15 minutes at 70 $^oC$ to remove $H_2O$.

After this thermal treatment, the active layer was spin coated to the layer stack on the substrate using the blend solution of PCBM:P3HT at room temperature with a spin rate of 2000 rmp for 1 minute. Thermal evaporation was performed to deposit a thin layer of aluminium on the sample to complete the whole organic solar cell after attaining a base of pressure of $10^{-4}$ Pa (A full technical detail of thermal evaporation is discussed in the following section). The OPV was later annealed in Ar gas at a temperature of $50^oC$ for 15 minutes to remove the residual solvent and promote nanoscale morphology.

**NB:** PCBM and P3HT were purchased at Sigma–Aldrich with 99.50% and 99.995% trace metals basis (purity), respectively. See the link below for information
$http://www.sigmaaldrich.com/catalog/product/aldrich/684449?lang=en\&region=ZA$

### 4.2.3 A solar cell with Ag NPs incorporated in the hole transport layer

The same method described above was used to prepare the PCBM:P3HT blend except for Ag NPs incorporation into PEDOT:PSS solution. The Ag NPs were suspended in distilled water were blended in PEDOT:PSS solution in the following ratios: for every $x$ drops of Ag NPs, 10 drops of PEDOT:PSS were added. The following droplet ratios were used in this work for Ag NPs and PEDOT:PSS, (2:10), (3:10) and (4:10).

All the different droplet ratios were separately spin coated on ITO under similar condition (see section 4.2.2) and thereafter annealed at 70$^o$C for 15 minutes. On each sample, the active layer of PCBM:P3HT (1:1) was spin coated.. Metallization of Al

electrode on the OPV was performed at $10^{-4}$ Pa by thermal evaporation. The OPV was the annealed in a vacuum at a temperature of $50^{o}C$ for 15 minutes.

### 4.2.4 Thermal evaporation technique

Thermal evaporation is a physical vapour deposition technique to deposit material as thin films onto a substrate.

Our interest in thermal evaporation is the deposition of thin (Al) films. Figure 4.1 shows the principles of thermal evaporation, involving vaporizing of solid by heating the material to sufficiently high temperature in high vacuum ($10^{-5}$mbar) [101]. The vaporized material diffuses radiatively upwards before it re-condenses on a cooler substrate mounted above the evaporation site. Vaporized molecules are allowed to deposit on the substrate due to their high condensation coefficient. While monitoring the process, a quartz crystal monitor will measure the films thickness as well the deposition rate [102].

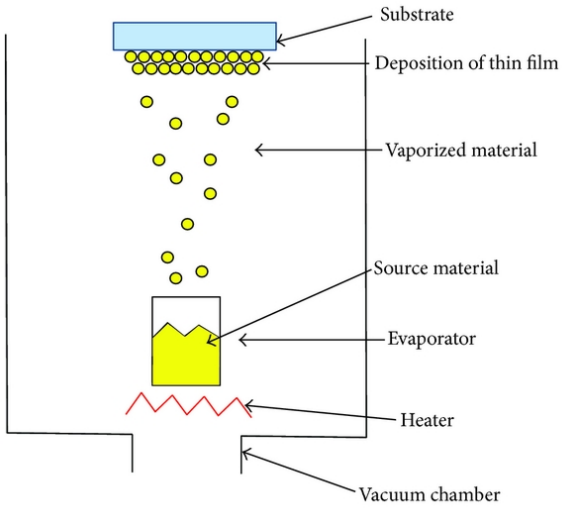



**Figure 4.1:** Schematic of thermal evaporation [103]

A thermal evaporation is a resistant heating method that is used to melt material and

raises its pressure (vapour) to a more useful range. This is achieved in high vacuum, allowing both the vapour to reach the substrate without reaction or scattering against other gas-phase atoms in the chamber. This reduces the incorporation of unwanted particles from the residual gas in the vacuum chamber [104]. Figure 4.2 shows the experimental set-up used in the present study metallization of Al on an organic solar cell and it is a home build thermal evaporator. The voltage used to melt Al was 45 Volts and the chamber deposition pressure was $10^{-4}$ Pa.

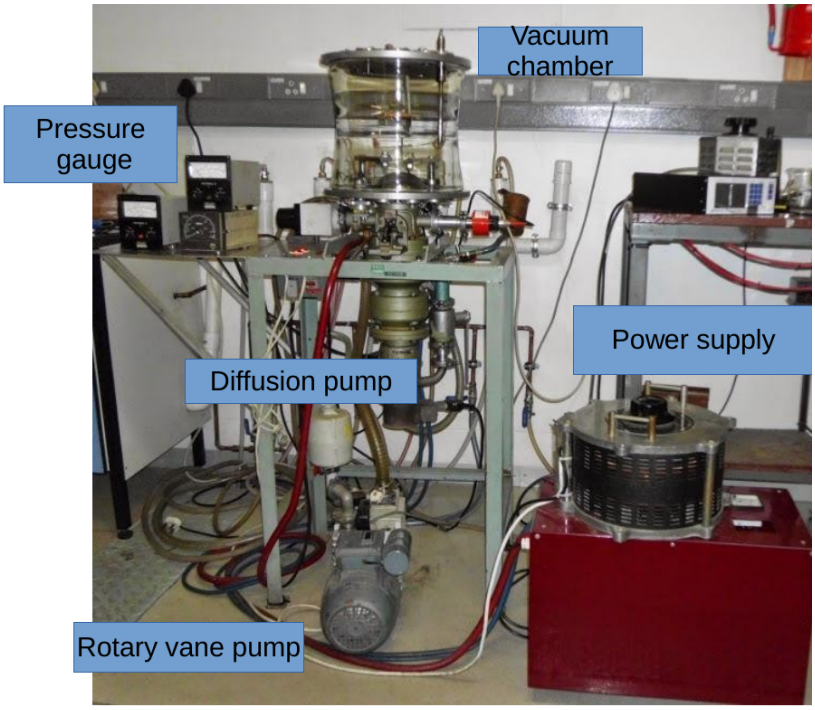



**Figure 4.2:** The experimental set-up of the thermal evaporation system used in the present study.

**Advantages of thermal evaporation technique:**

- Low impurities on the deposited thin films.
- Enhanced control of deposition rate.
- Loading of larger charges per deposition run.

**Disadvantages of thermal evaporation technique:**

- A lot of material is lost in the process.
- AC power supplies are huge and expensive

## 4.3 Sol-gel technique

The sol-gel process is a method used for producing glasses from small molecules [105]. The general idea of sol-gel synthesis is dissolving building blocks as alkoxydes from a liquid in order to reproduce it as a solid material in a more controlled manner. In general a sol is considered as a stable dispersion of colloidal particles or even polymers that are in a solvent. Then particles can either be crystalline or amorphous. There are three types of particles that formed in this process, where we have aerosol particles that are formed in a gaseous phase, sol has particles in a liquid phase [106] and gel have 3D continuous network, which encloses a liquid phase. But in a colloidal gel, the network is generated from the agglomeration of colloidal particles.

Polymer gel have particles that are polymeric sub-structured made from bulk of sub-colloidal particles. Basically, there's an interaction within the sol particles through van der Waals forces or hydrogen bonds. A gel can be formed through cross linking of the polymer chains. In a gel systems used for the synthesis of materials, the covalent nature of the interactions render a gelation process that is irreversible. The gelation process can however be reversed if other bonding interactions are involved [107, 106].

**Advantages of sol-gel technique**[108]

1. Low cost (effective cheap technique to produce high quality coatings).
2. Can be useful in preparing materials with different shapes, such as thin films,

porous structures, dense powders and thin fibers.

3. Shapes materials into complex geometries in a gel state.

4. Has low sintering temperature capability, usually 200 – 600 $^{o}$C.

5. Produce high purity products where the composition can be highly controllable.

There are **two types of sol-gel conditions** in every synthesis:

(a) Acidic conditions: there's a decrease in reaction rate when alkoxy groups are hydrolyzed.

(b) Basic conditions: reaction rate increases instances where alkoxy groups are dehydrolyzed to form spherical particles, powders and etc.

**Application**: Sol-gel derived materials have different roles in optics, electronics, energy materials, space science, thin films, (bio) sensors, medicine (e.g. controlled drug release) and separation technology (e.g. chromatography).

Sol-gel process includes the following steps during synthesis [107] (See figure 4.3):

1. Hydrolysis: is a process where decomposition involving separation of a bond which links with the addition of the hydrogen cation and the hydroxide anion of water.

2. Condensation: a reaction in which two molecules add up to form a larger molecule, including the loss of a small molecule which gives a formation of a network.

3. Gelation: Gels as defined by Born are liquids that exhibit a high elastic resistance against shear due to their excellent viscous and elastic properties. A gel is the product of condensation, where the network spans the size of the system (e.g. film/particle size).

4. Ageing: this is attributed to the physical change of a material with respect to time, in a environment with defined conditions, resulting to improvement or deterioration of properties.

5. Sintering: a process of densifying and forming a solid mass of material by heat or pressure without deforming the structure.

6. Drying: A mass transfer process where water or another solvent removed from a solid by evaporation.

7. Densification: is the act of reducing porosity in a sample by making it more dense.

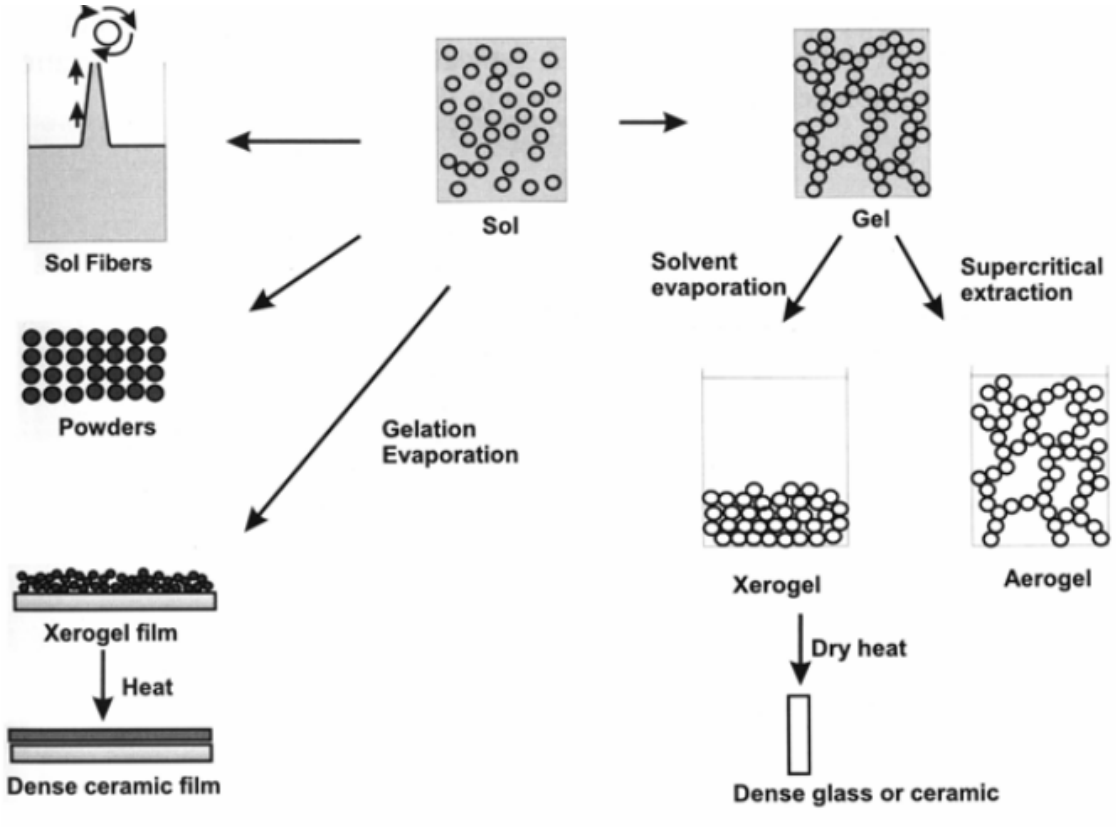



**Figure 4.3:** Sol-gel processing options [107]

The sol–gel method was used in the preparation of $SiO_2 - HfO_2$ planar waveguides

doped with $Eu^{3+}$ in a clean room at room temperature with a humidity of 59% to give quality waveguides.

### 4.3.1 Dip-coating process

The dip-coating process is a method used to deposit thin layers on different substrates, this technique is applied right after the sample preparation and it is separated into the five stages listed below [109]:

1. Immersion: The clean substrate is immersed in the solution at a constant speed for the coating material.
2. Start-up: The substrate will remains inside the solution for a certain period of time and then starts to be pulled up with the same speed it was immersed. The withdrawing is also at a constant speed to avoid any jitters.
3. Deposition: The thin layer will start deposits itself on the substrate during withdrawal.
4. Drainage: Excess liquid drains out from the surface.
5. Evaporation: The solvent evaporates, to form a thin layer. For some solvents, like alcohols, evaporation take place when the deposition and drainage steps are in process.

Within a continuous process, all these steps are carried sequentially.

When depositing each layer of $Eu^{3+}$ doped $SiO_2 - HfO_2$ waveguide the following parameters were kept constant:

1. Speed rate for immersion: 30 mm/minute

2. Wait time (start-up): 30 seconds

3. Speed for withdrawing the sample (Deposition, Drainage and Evaporation): 30 mm/minute

4. Wait time before removing the sample (Evaporation and Drainage): 30 seconds

After deposition the sample was heated in an oven at 900 $^oC$ for 60 seconds. This process was repeated 20 times since each waveguide had 20 thin layers of $Eu^{3+}$ doped $SiO_2 - HfO_2$ waveguide. The speed at which you immerse and withdraw determines the thickness of the coating (the faster the withdrawal the thicker film).

### 4.3.2 Cleaning of substrate

The glass substrate (v–SiO) were cleaned with detergent and rinsed with deionized water. Thereafter the glass substrate was sonicated for 15 minutes in acetone, followed by methanol ultra–sonicating for 15 minutes. Finally the samples were sonicated in ethanol and distilled water for 10 minutes again and then dried with purified nitrogen gas.

### 4.3.3 $SiO_2 - HfO_2$ planar waveguides doped with $Eu^{3+}$

Two starting solutions were prepared namely; the first one was prepared by adding 3 ml of tetraethylorthosilicate (TEOS) into 17 ml of ethanol (EtOH), proceeded by 4.80 ml of deionized water ($H_2O$) into 0.8 ml of hydrochloric acid (HCl) (HCl added as catalyst); EOS:EtOH:$H_2O$:HCl, was then left to prehydrolyze for 1 hour at 65 $^o$C. The second solution of ethanolic colloidal suspension was also produced by using as 2.2g of HfOCl as a precursor, mixed in TEOS solution, with Si/Hf molar ratio of 70/30.

Europium ($Eu(NO_3)_3$ solid phase, mass of 0.154 g) was added with a $Eu(Si + Hf)$ molar concentration of 0.01 percent and was prehydrolyzed for 1 hour at 65 $^o$C.

The two solutions were then mixed together and the final mixture stirred for 16 hours at room temperature. The obtained solution was then filtered with a 0.2 millipore filter for dip coating Eu doped silica-hafnia waveguide. Europium-activated silica–hafnia waveguide were obtained and then deposited on cleaned pure v–SiO glass substrates using dip-coating technique, with a dipping rate of 30 mm/min (it includes the immerse and withdraw speed). Before coating additional layers, post deposition annealing of each layer was carried out in vacuum for 1 minute at 900 $^o$C. After 20 cycles of dipping, the film was subsequently heated for 2 min at 900 $^o$C. Final films, produced from 20 coatings, were then stabilized by a last thermal treatment for 5 min in air at 900 $^o$C. As a result transparent and crack-free waveguides were obtained.

## 4.4 Techniques used for optical and morphology analysis

### 4.4.1 Scanning electron microscopy for morphological analysis

Imaging of a sample in scanning electron microscopy is achieved by scanning the sample using a focused beam of accelerated electrons in the range of (0.5–30 kV). The interaction of atoms with electrons within a sample, produces ls that are detected and also has information about the sample's composition and its surface topography [110].

Energy-dispersive X-ray spectroscopy (EDS, EDX, or XEDS) is an analytical tool used for elemental or chemical analysis of an SEM sample. This technique relies on the interaction of the sample with the incident electron beam, producing X-rays characteristic of the chemical or elemental composition of the irradiated sample area. These

characteristic X-ray are dependent on the unique atomic structure of every element. Thus enabling the measurement of a unique set of peaks in the X-ray spectrum of the element of interest [111].

An atom in a sample, at rest is at the ground state, with electrons having discrete energy levels. The incident beam will excite an electron within an inner shell, so that it ejects it from this shell while creating a hole. The system is likely to de-excite so that it can occupy the empty level with an electron, there by emitting a characteristic X-ray of energy equal to the difference in energy of the lower and higher energy levels. The number of the X-rays emitted and their corresponding energy are measured using an energy-dispersive spectrometer [112].

### 4.4.2 Transmission electron microscopy for morphological analysis

Transmission electron microscopy (TEM) images are formed when there is an interaction of the electrons, that are transmitted through the sample. A continuous beam of a highly accelerated electrons (30–300 kV) is transmitted through a very thin sample (<100nm), interacting with the sample as it passes through it. The sample can be drop cast on a TEM Cu–grid for imaging (for technical reasons). Energy dispersive spectroscopy (EDS) is a technique or procedure that is used to identify and quantify elemental composition of sample surface area in small ranges such as in nanometers and is also performed on TEM using the same principles mentioned in the previous section [88].

### 4.4.3 UV-vis spectroscopy for optical characterization

Ultraviolet–visible spectroscopy relates to the absorption transmission and reflection characterization of materials in the ultraviolet–visible spectral region. In some instances the optical response of materials in the light near–UV and near–infrared the same range of optical excitation. But absorption in the visible range is directly affected by the detection of colors of chemicals that are involved in the sample [113]. This is a region of electromagnetic spectrum, where materials undergo electronic transitions. The technique complements fluorescence spectroscopy. However the difference between absorption and fluorescence is that absorption measures transitions from the ground state to the excited state whilst fluorescence probes transitions from the excited state to the ground state [114]. The optical measurements were carried out using WIN CARY 500 spectrometer, set in the range 200 nm to 800 nm after a baseline correction for 100% and 0% calibration.

# Chapter 5

# Results and discussion

In this chapter we report, foremost the simulations of the scattering and absorption cross–section of Ag NPs were calculated using MEEP (FDTD methods). The morphology analysis of Ag NPs synthesized by chemical reduction method is presented in detail. Their optical and morphology characteristic are discussed in detail to determine their plasmonic effect and dependencies on shape, size and interspacing of the Ag NPs absorption. As a proof of concept organic solar cell is incorporated with Ag NPs to observe efficiency enhancement effects associated with plasmonic effect. Lastly a discussion on the synthesis and characterization of $Eu^{3+}$ doped waveguides is presented.

## 5.1 Data analysis from MEEP simulation

### 5.1.1 Methods of the simulation

The domain consists of a single silver spherical metal NPs of diameter $a$. Perfectly matched layers (PMLs) were used in the upper and bottom boundaries to prevent reflection. Periodical boundary conditions were used in the lateral directions to model periodic array of NPs.

On the surface there were 10 spherical Ag NPs. A plane wave source of polarized electric-field was placed 500 nm above the surface. The transmitted power into the particles was measured by a frequency domain monitor placed at the plane interface. It was calculated by integrating the Poynting vector of the Fourier transformed electromagnetic fields over the plane in the normal direction as discussed in section 3.2. The integrated transmission efficiency within the spectral range of 200-900 nm was calculated.

From the Drude-Lorentz equation (discussed in section 3.1.3.3), the resultant/complex dielectric function of a metal was defined as:

$$\varepsilon(\omega) = 1 - \frac{\omega_p^2 \sigma_o}{\omega(\omega - i\gamma_o)} + \Sigma_j^k \frac{\omega_p^2 \sigma_j}{\omega_j^2 - \omega^2 + i\omega\gamma_j} \tag{5.1}$$

where $\varepsilon(\omega)$ is the dielectric function, $\omega_p$ is the plasma frequency with oscillator strength $\sigma_o$ and damping frequency $\gamma_o$, $k$ is the number of oscillators with resonant frequency $\omega_j$, strength $\sigma_j$ and damping frequency $\gamma_j$. The parameters for the complex dielectric function used for Ag NPs in the FDTD simulations are given in table 5.1. These values were obtained from [115, 116].

| | Ag |
|---|---|
| $\omega_p$ (eV) | 9.01 |
| $\sigma_0$ | 0.845 |
| $\gamma_0$ (eV) | 0.048 |
| $\omega_1$ (eV) | 0.816 |
| $\sigma_1$ | 0.065 |
| $\gamma_1$ (eV) | 3.886 |
| $\omega_2$ (eV) | 4.481 |
| $\sigma_2$ | 0.124 |
| $\gamma_2$ (eV) | 0.452 |
| $\omega_3$ (eV) | 8.185 |
| $\sigma_3$ | 0.011 |
| $\gamma_3$ (eV) | 0.065 |
| $\omega_4$ (eV) | 9.083 |
| $\sigma_4$ | 0.840 |
| $\gamma_4$ (eV) | 0.916 |

**Table 5.1:** Parameters used in the modelling of Ag NPs absorption and scattering cross–section.

### 5.1.2 Results from the simulation:

Figure 5.1 shows the scattering cross-section, for a simple plane surface with silver spheres of different sizes. The simulation was performed using FDTD for different sizes (diameter: 40, 50, 60, 70, 80, 90 and 100 nm) of the spherical Ag NPs. Note that the resonance for the Ag NPs is in the ultraviolet region. As the size increases so does the scattering cross-section.

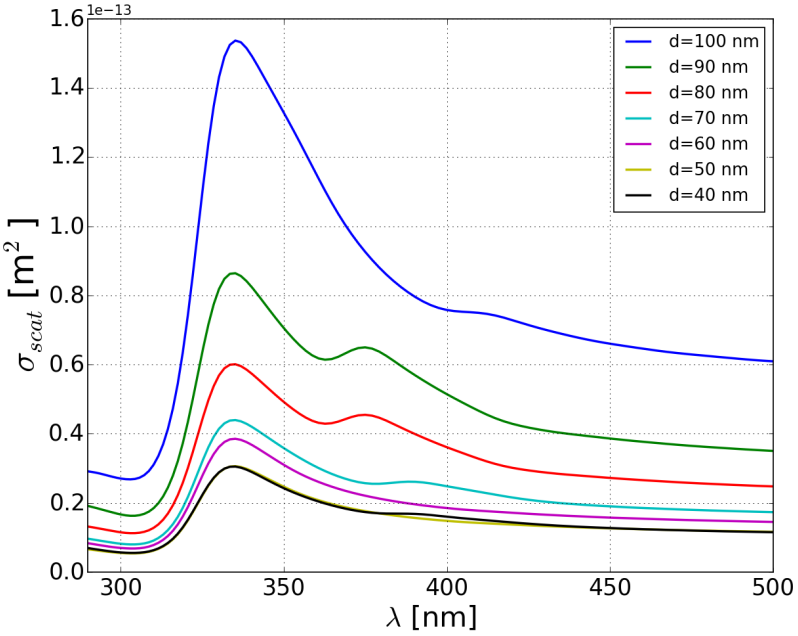



**Figure 5.1:** The scattering cross–section for silver spheres of different diameters.

Simple structures such as isolated tiny spheres exhibit a single plasmon resonance. Nevertheless, more complicated structures often may result multi-featured resonance spectra, with an enhanced strong local fields in at intersection points or in between gaps of different particles [117, 118].

The plasmon resonances of complex structures is the result of "hybridization" fundamental plasmons of simple subs–tructures [118]. Figure 5.2 shows the absorption cross-section, for a simple plane surface with silver spheres. We observe that as the size of Ag NPs decrease the more it absorbs light. The absorption cross-section increase results a blue shift and there's no dependence in the wavelength ($\lambda$).

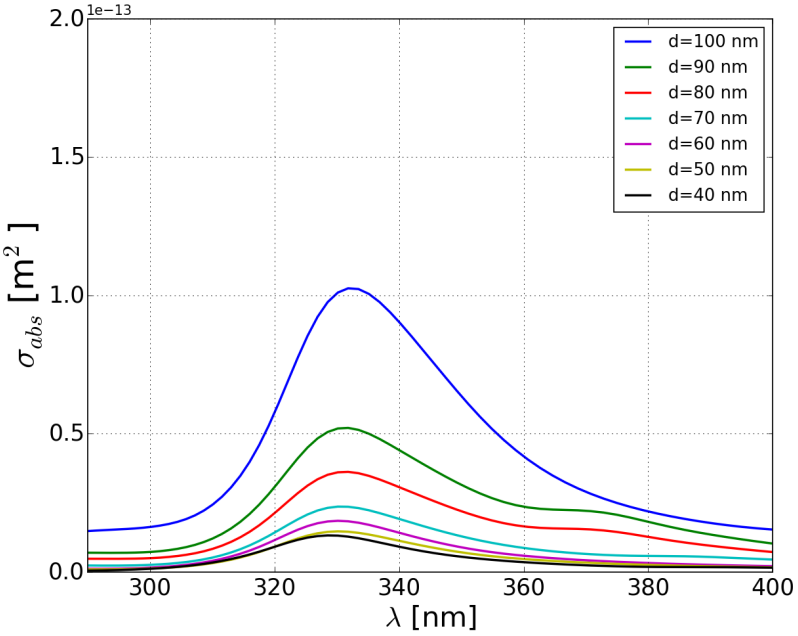



**Figure 5.2:** The absorption cross-section for a simple plane surface with silver spheres of different diameters.

Note that for small particles with diameter of 5 nm (see figure 5.3 ) there is a shift resonance observed at more or same the amplitude of the the particle. The shift observed is to surface plasomn where the this particles scatter light and absorb light nearly at the same ratio. Small particles absorb light while bigger particles scatter light (see figure 5.4 and figure 5.3).

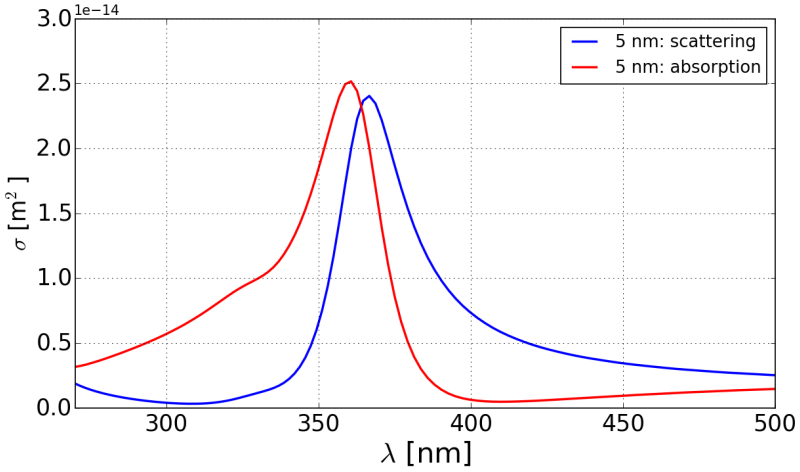



**Figure 5.3:** Scattering/absorption cross-section for a spherical Ag NPs of a diameter 5 nm in a simple plane surface.

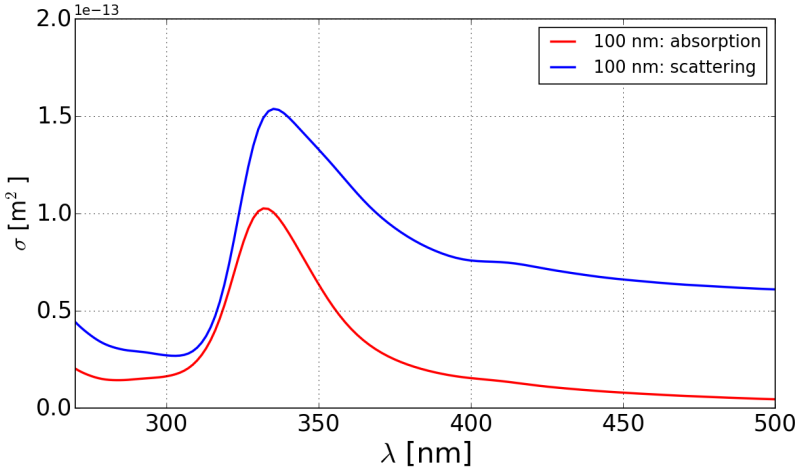



**Figure 5.4:** Scattering/absorption cross-section for a spherical Ag NPs of a 100 nm diameter in a simple plane surface.

The amount of light that is scattered and absorbed by the particle, and the angular distribution of the scattered light, depends on the properties of the Ag NPs, such as shape, size, material properties and the angle at which the particle is illuminated. A strong scattering and absorption of the light for metallic NPs results is related to the intense surface plasmon extinction of bands [119]. From the size and shape of these Ag NPs we can obtain optical properties such as resonant frequencies, field distributions, field enhancements [120].

The Lorentzian function in equation 3.46 also describes the response due to the LB transition at energy $\omega_o$ [121]. The optical response of Ag spherical nanoparticle, with dispersive and a complex dielectric $\varepsilon = Re(\varepsilon) + Im(\varepsilon)$ immersed in an medium $\varepsilon_n$ is obtained by the quasi-static theory [122]. From the particles polarization, the quasi-static dipole approximation, then the LSPR is defined by

$$Re\{\varepsilon_m + L(\varepsilon(\omega) - \varepsilon_n)\} \tag{5.2}$$

where L is the shape factor of the particle and for a spherical particle in air ($L = 1/3, \varepsilon_n$), an LSPR is defined by the Frohlich condition [121, 123]

$$Re\{\varepsilon(\omega)\} = -2\varepsilon_n \tag{5.3}$$

To achieve resonance conditions of equation 5.3, $Im\{\varepsilon(\omega)\}$ must be close to zero. This is a condition that is satisfied by metals. Large $Im\{\varepsilon(\omega)\}$ means a weak plasmon resonance.

## 5.2 Morphological analysis of Ag NPs

TEM (transmission electron microscope) images of Ag NPs were captured. These particles were synthesised at constant temperature and concentration (measured in molarity M) of $AgNO_3$ through out, but at varied reaction times. For this analysis Ag NPs were deposited on a TEM copper grid coated by carbon. The particle size were analysed using *Imagej software*. This is an open source software found at *https* : *//imagej.nih.gov/ij/download.html*

Particles prepared at 100 $^oC$ and $AgNO_3$ concentration of 0.1 M for 3:10 hours, showed the distribution of the spherical Ag NPs on the Cu grid (see Figure 5.5). These particles are uniformly distributed and spherical at a magnification of 200× having an average diameter of 15 nm (see figure 5.6). Note that the Ag NPs are very much close to each other and hence the multiple resonance cannot be excluded.

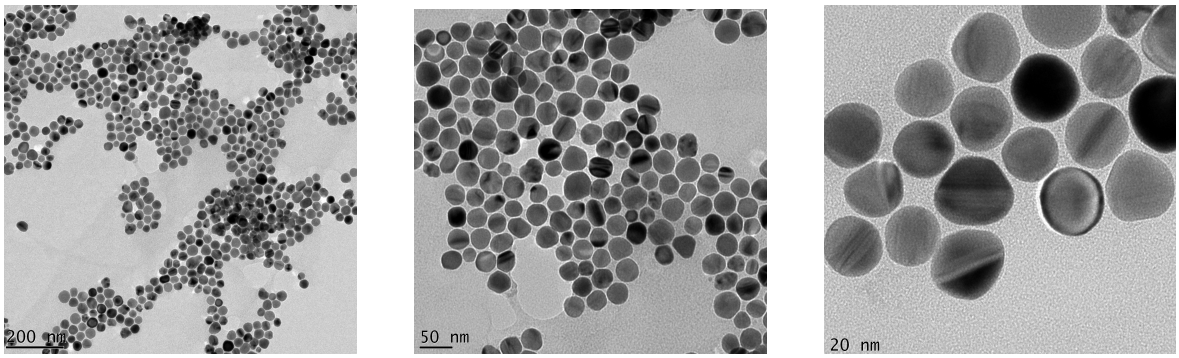



**Figure 5.5:** TEM images showing spherical Ag NPs.

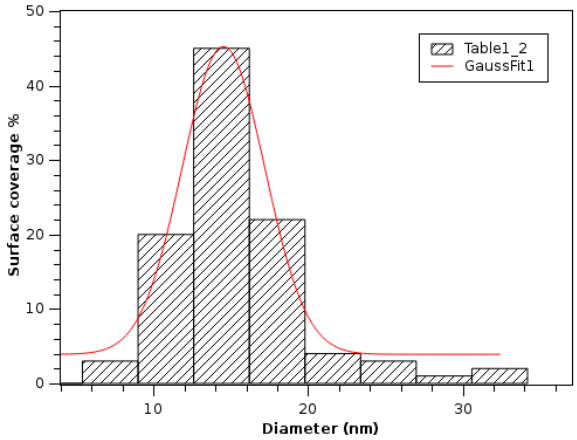



**Figure 5.6:** Histogram showing Ag spherical NPs of an average diameter of 15 nm.

Figure 5.7 shows Ag NPs synthesized at 100$^o$C with $AgNO_3$ concentration of 0.1 M but allowed to react for 3 hours and 20 minutes resulting in prism like shapes. Some of these particles began to agglomerate, leading to a change in shape and size. they still remain uniformly distributed (mono dispersed) and EDS analysis confirmed that these NPs were Ag NPs (see figure 5.12b). The size of the particles decrease as the particles reacts longer, giving an average particle diameter of 14 nm (see figure 5.8). However owing to the bimodal distribution figure 5.8, it is clear that longer reaction times favours the nucleation of smaller Ag NPs of 7 nm diameter. Note that particles are not very much close to each other except when they are nucleating. The longer the reaction time also leads to large Ag NPs ($>$ 20 nm.)

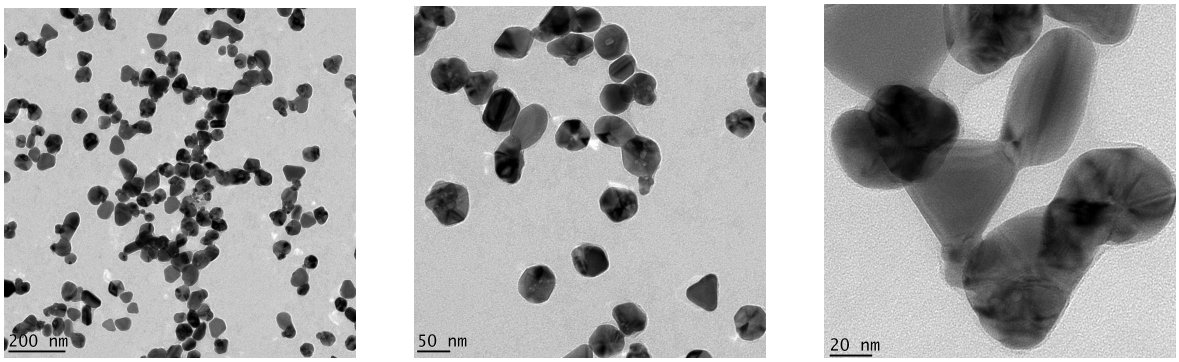



**Figure 5.7:** TEM images showing prism like Ag NPs.

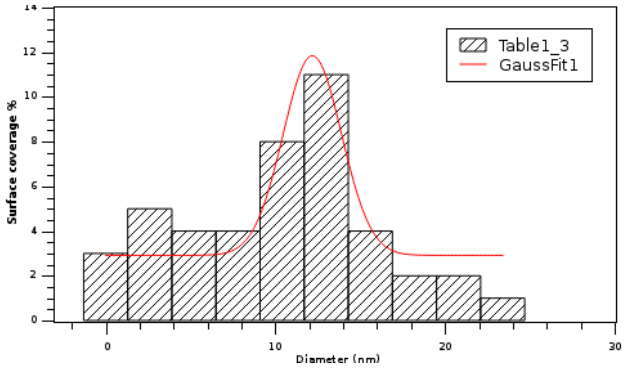



**Figure 5.8:** Histogram showing agglomerated prism like Ag NPs of an average diameter of 14 nm.

Figure 5.7 also depicts Ag NPs which were synthesised at 100$^o$C with $AgNO_3$ concentration of 0.1M but allowed to react for 3 hours and 40 minutes. Most of the particles have agglomerated with no uniform particle distribution and size dispersion. Therefore longer reaction times, weakens the role of stabilizer (PVP), which leads to inhomogeneous agglomeration and nucleation of the Ag NPs. At this point to determine the size particles is easy because of the state of shape, but for particles where two or three particles fused together the average particles size were 16 nm (see figure 5.10).

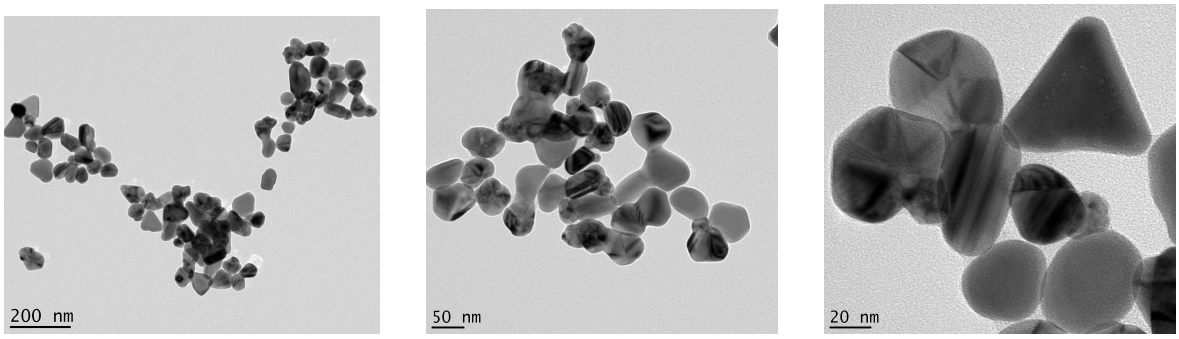



**Figure 5.9:** TEM images showing nucleated prism Ag NPs.

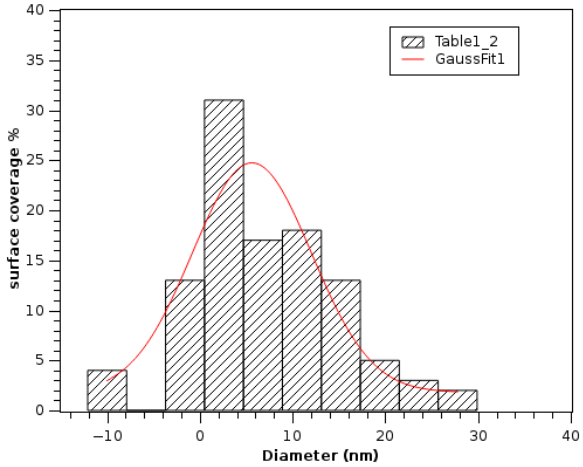
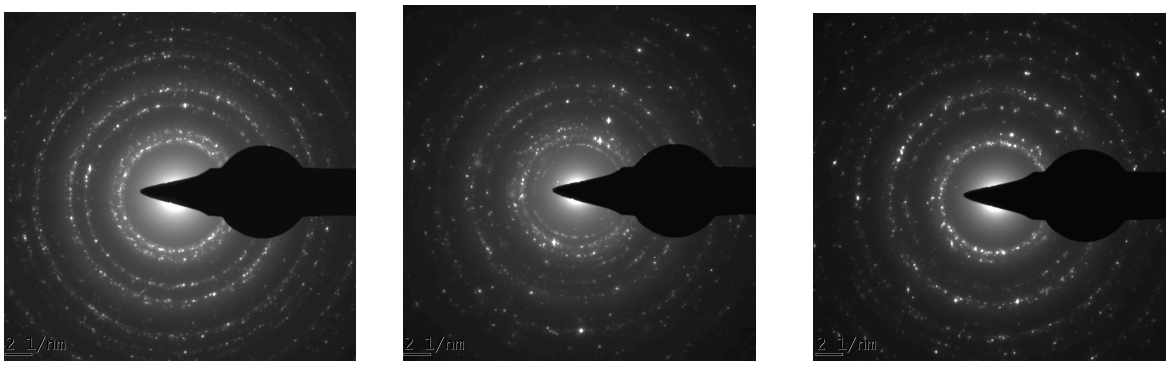



**Figure 5.10:** Histogram showing agglomerated Ag NPs average diameter of 16 nm.

Selected Area Electron Diffraction (SAED) patterns were recorded for Ag NPs in the aggregate to determine their crystal structure. Figure 5.11 confirms the polycrystalline (small spots making up a ring, each spot arising from Bragg reflection for an individual crystallite) nature of a basic face-centred-cubic structure of Ag NPs. From the SAED pattern of metal we observe bright spots.

As the shape of the Ag NPs changes so are the ring patterns. For spherical Ag NPs the rings are more bright and clear (see figure 5.11a). We observe that as the shapes change the rings becomes dimmer (see figure 5.11b), for example the rings of the fully nucleated particles are blurred as compared to the others (the rings spherical NPs are clear and brighter (see figure 5.11a)). This could mean that the more complicated structure Ag NPs may reduce the quality of polycrystallinity.

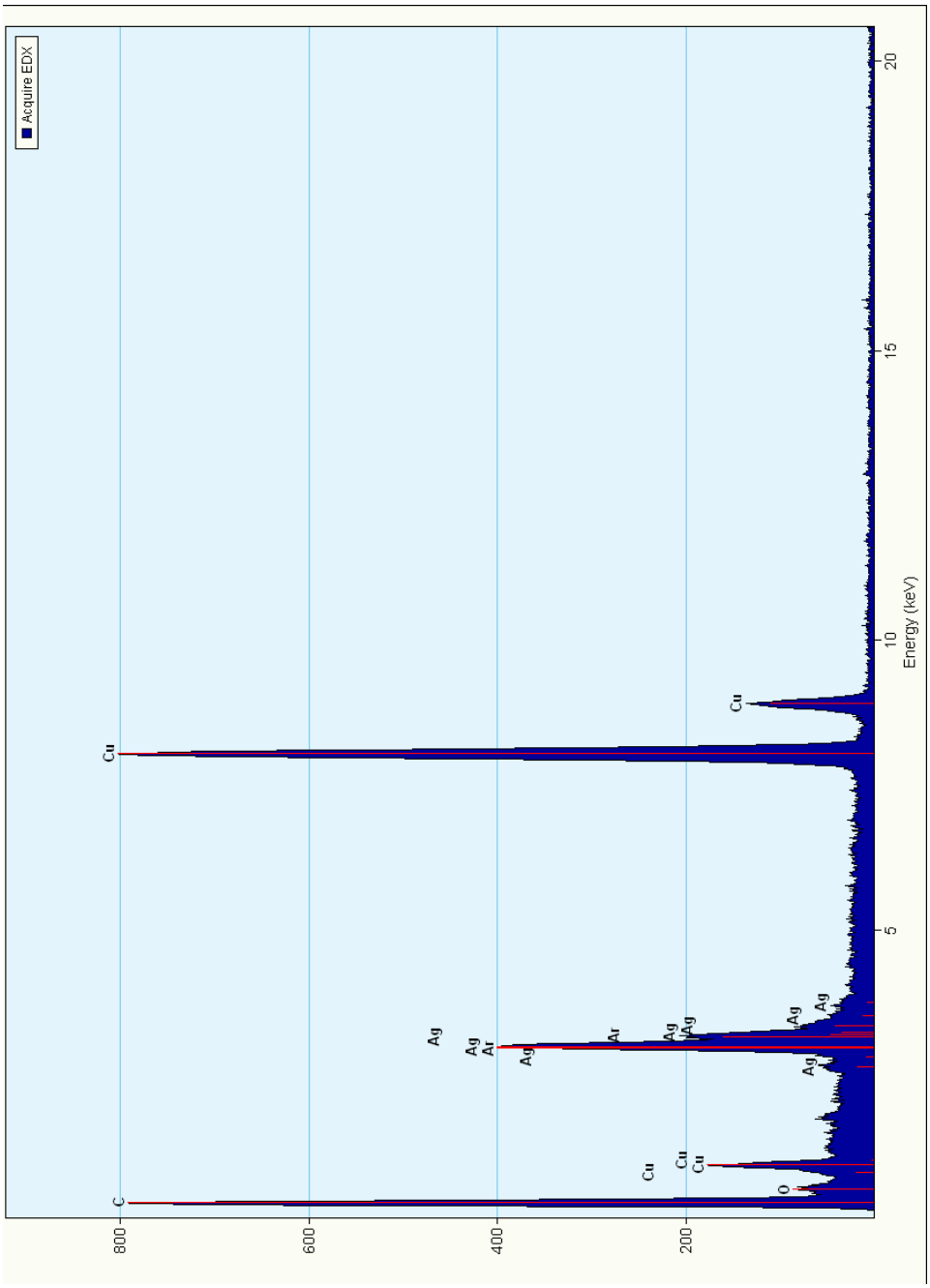


**(a)** spherical Ag NPs **(b)** prism like Ag NPs **(c)** agglomerated Ag NPs

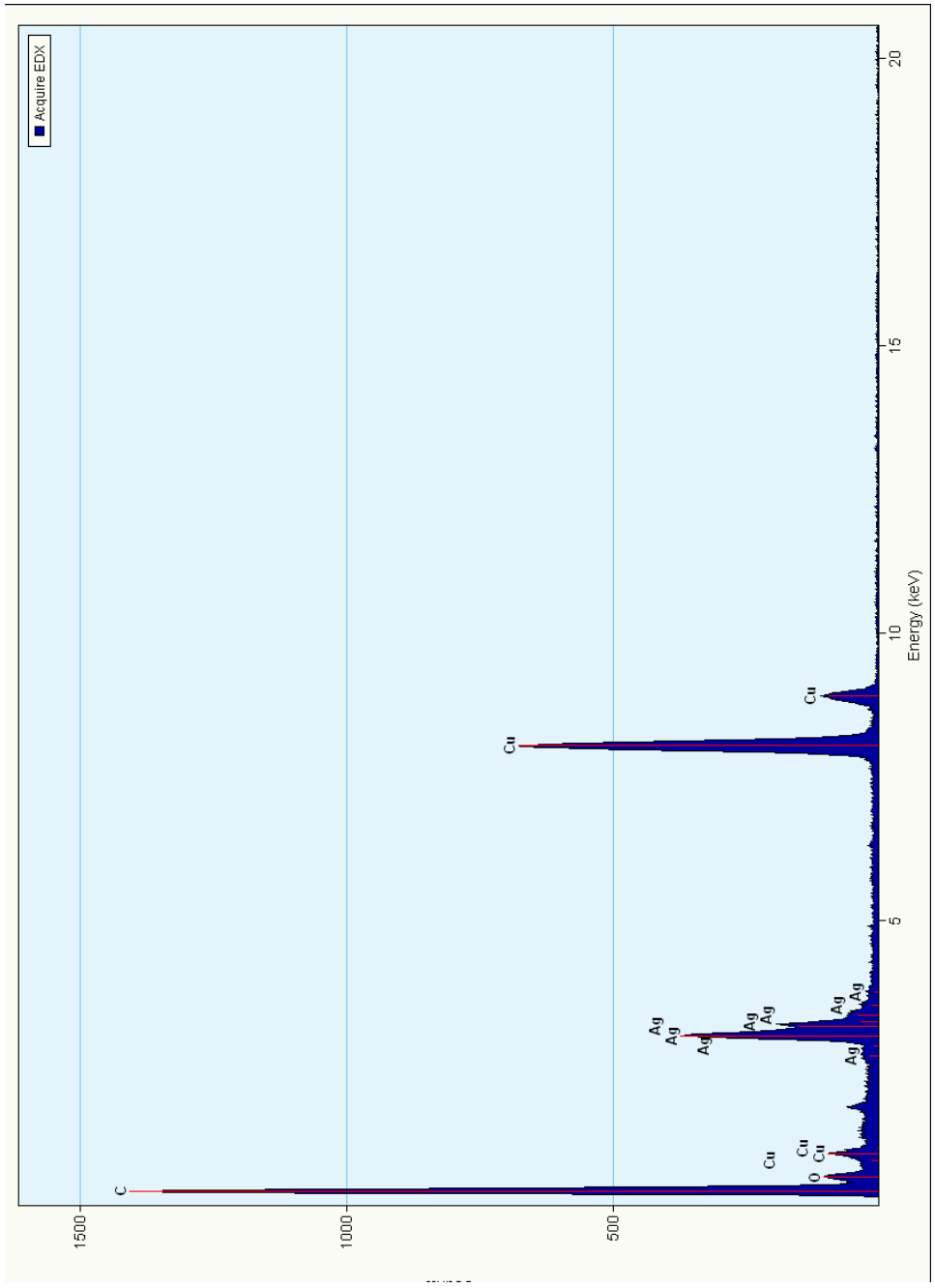
**Figure 5.11:** SAED patterns of Ag NP synthesized at varied reaction time

To confirm if these particles were Ag NPs (see Figure 5.12), EDS profile of these samples was performed, where the L lines of Ag were observed at approximately 3 keV, confirming the presence of silver.

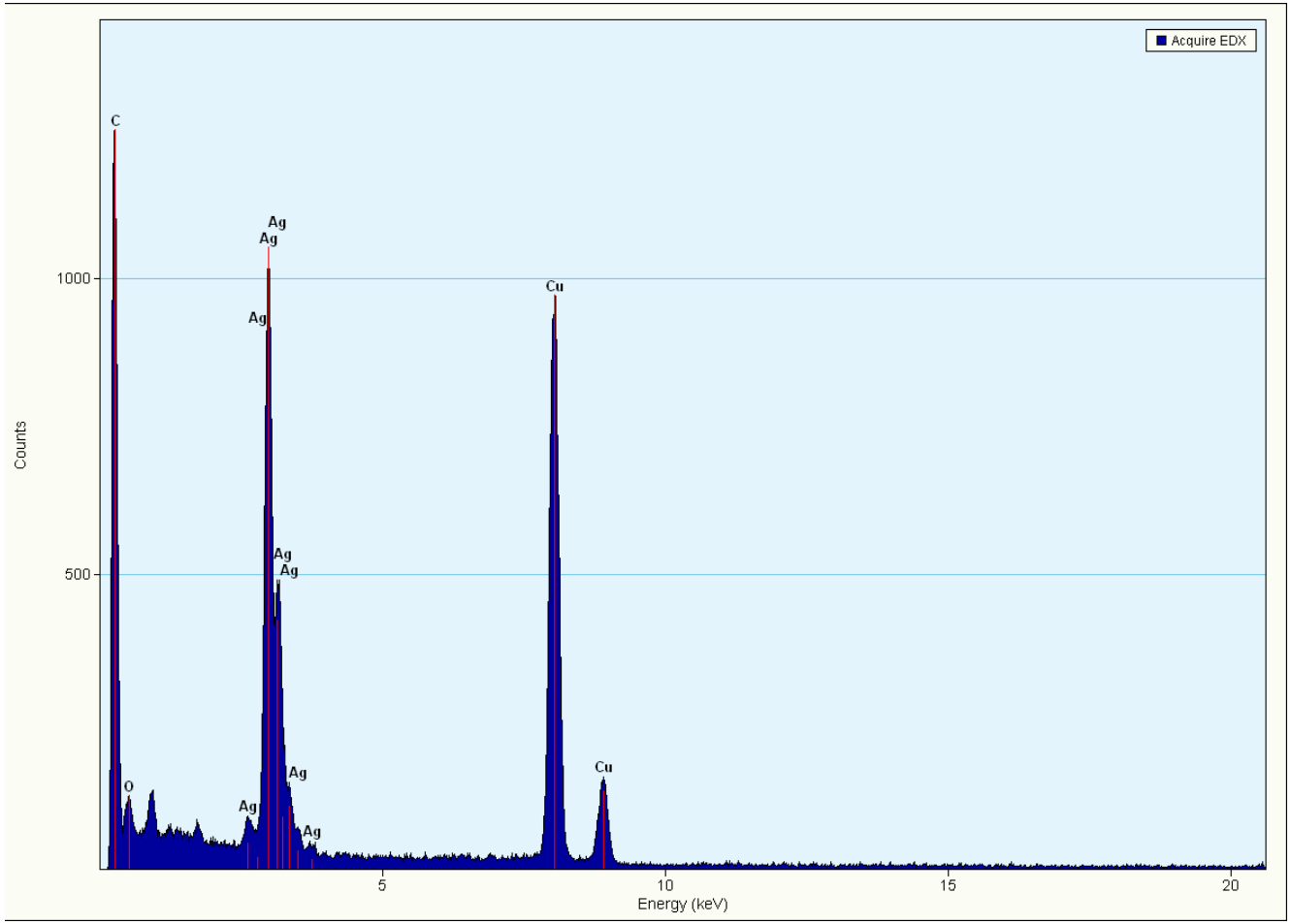
The length of the reaction times provides sufficient energy to add atoms together and even to nucleate new Ag NPs. The surface diffusion of these ad atoms is therefore expected to enhance nucleation and growth of the particles. This results not only in the shape changes but also as in size changes as well. Whereby, the environment in terms the LSPR properties is sensitive to shape and size of NPs [124]. Also the dielectric function of the host (glass) with the NPs affects the LSPR resonance frequency and bandwidth [71].




**(a)** spherical Ag NPs




**(b)** prism like Ag NPs




**(c)** agglomerated Ag NPs

**Figure 5.12:** EDS of Ag NPs synthesized at varied reaction times

## 5.3 The optical absorption of Ag NPs by UV-Vis Spectroscopy

The absorption of light by specific materials at a specific wavelength determined by the absorption coefficient. Materials that are suitable for solar cell applications in general possess a high absorption coefficients ( $10^7\ m^{-1}$) over a wide range of wavelengths. Our series of Ag NPs grown by chemical reduction process at different reaction times and at constant temperature and concentrations were characterized using a UV–Vis NIR–500 CARY Spectrophotometer, at the school of chemistry, university of Witwatersrand.

Figure 5.13 illustrates the optical absorption spectra of Ag NPs synthesized by chemical reduction at $100^oC$ and 0.1M concentration of $AgNO_3$ but at different reaction times.

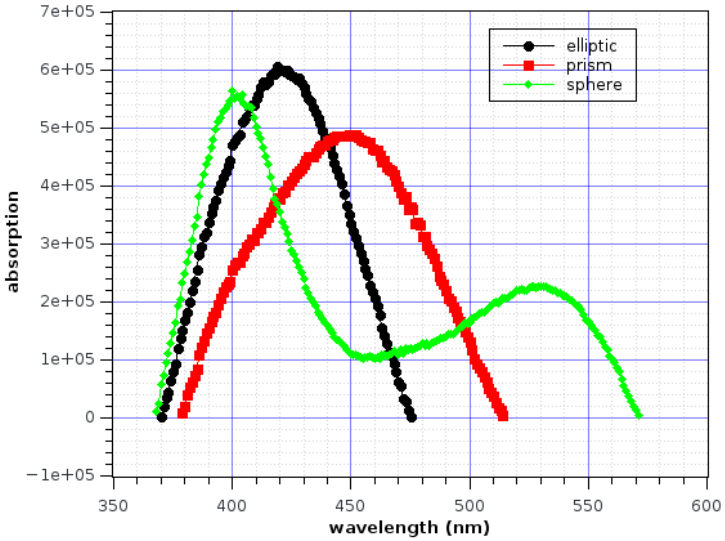
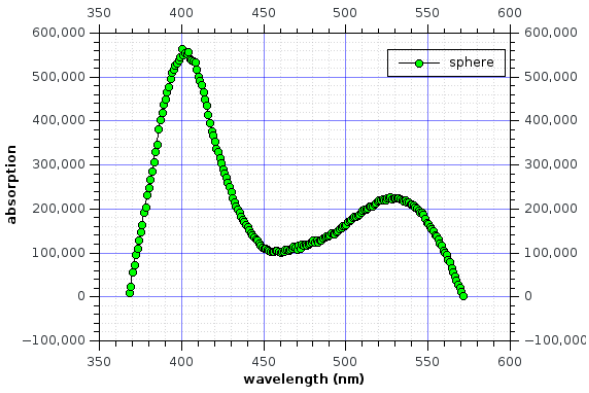



**Figure 5.13:** Absorption spectrum of Ag NPs fabricated at varied reaction times

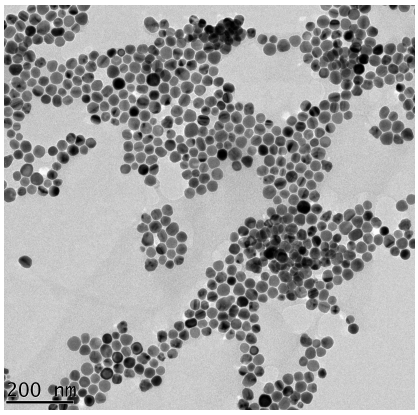
In this case experimental results are exactly in good agreement with theory where the resonance is at 400 nm for Ag NPs of 20 nm. The appearance of two resonance peaks of figure 5.13 indeed puzzling as it is expected that for a spherical NPs should be a single resonance. However it is plausible that the quadrupole effect or higher order resonance come into play due to increased interaction between Ag NPs.

To further analyse the results, we present TEM data with optical resonance data of spherical Ag NPs in figure 5.14. The absorption optical spectra of spherical Ag NPs (see figure 5.14a) shows bimodal peaks depicting the excitation of a spherical Ag NPs. Additional absorption peaks may correspond to the poly dispersed Ag NPs are shown in figure 5.14b or higher order resonances. Spherical Ag NPs show a plasmon resonance at 400 nm, and an in-plane dipole resonance at 534 nm, (See [125] for details).

Importantly, this behaviour of the induced polarizations depends strongly on interparticle distance, with dipoles in the inter-facial region between the spheres being strongly influenced by interparticle coupling when the particles are close together [126]. From the TEM image (figure 5.14b) clearly the spacing between the particles may indicate the presence of the second peak.




**(a)** Absorption spectra for spherical Ag NPs




**(b)** TEM image for spherical Ag NPs

**Figure 5.14:** Absorption spectra and TEM images showing interspacing of spherical Ag NPs

The size and shape changes in the Ag NPs after long reaction times, lead to a red shift in the absorption cross-section/spectra indicating an increase of Ag NPs size with aspect ratio. The higher magnitude of the absorption cross–section in comparison to their scattering cross–section of 10 nm Ag NPs derived from numerical solution of Maxwell's equation by FDTD illustrate the observation, that small size particles absorb more predominantly rather than scatter (see figure 5.15).

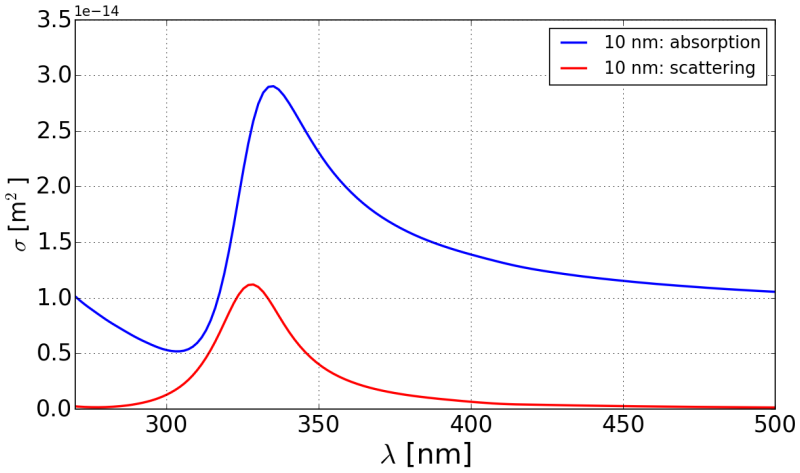



**Figure 5.15:** Absorption spectra for Ag spherical NPs of 10 nm diameter with MEEP simulation.

## 5.4 The I-V characteristics of organic photovoltaic cell and analysis

The effect of the surface plasmon resonance on OPV device efficiency was investigated by incorporating the Ag NPs on a hole transport layer (PEDOT:PSS) of the device. They were spin coated on ITO, after blending in PEDOT:PSS. A reference device was made first without Ag NPs with the following structure: ITO/PEDOT:PSS/ P3HT:PCBM/Al. For the Ag NPs incorporation, the Ag NPs were blended in PEDOT:PSS with different droplets ratios of Ag NPs (2, 3 and 4 drops of spherical Ag

NPs) into 10 drops of PEDOT:PSS. The architecture of the device used in this work was of the following format; ITO/Ag NPs + PEDOT:PSS/ P3HT:PCBM/Al having a 1:1 ratio of the P3HT:PCBM blend. Figure 5.16 shows the I–V characteristics for the reference device and the devices with the different droplet ratios of Ag NPs into 10 drops of PEDOT:PSS (2:10, 3:10 and 4:10).

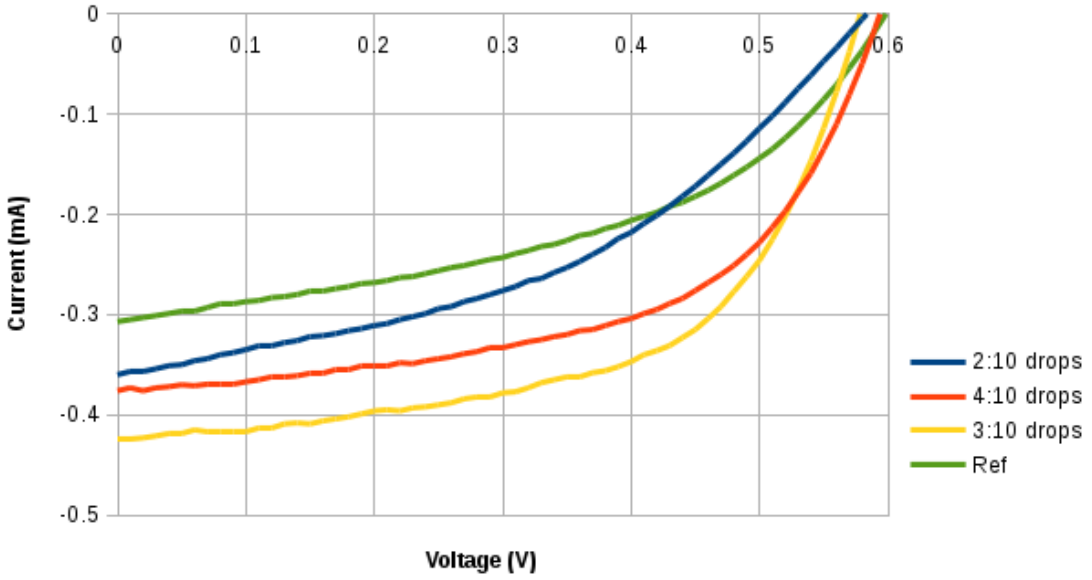



**Figure 5.16:** I–V characteristics of fabricated devices with different concentration of Ag NPs

It is seen that spherical and polydispersed Ag NPs incorporation into PEDOT:PSS leads to an increase of the short circuit current $I_{SC}$ below the threshold concentration. The open circuit voltage $V_{OC}$ of the Ag NPs incorporated device does change not significantly. This indicates that the addition of Ag NPs does not change the interfacial properties of the active layer. The summary of these results are presented in table 5.2.

Table 5.2 shows that the $I_{SC}$ increases with an increasing Ag NPs concentration by 72%. The increase of the $I_{SC}$ could be attributed to the enhanced absorption due to LSPR effect. The $V_{OC}$ remains more or less the same which indicates that that the addition of Ag NPs does not change the electronic structure of the active polymer blend of the Bulk hetero-junction. The increase of the $I_{SC}$ with increasing Ag concentration

denotes the absence Schottky barrier (Ag work function  4.6 eV). This is expected as Ag NP are dispersed in PEDOT:PSS below the percolation threshold.

| Parameters of the organic solar cell with and without Ag NPs | | | | |
|---|---|---|---|---|
| Device (drops ratio of Ag NPs into PEDOT:PSS) | Short circuit current $I_{sc}$ (mA) | Open circuit voltage $V_{oc}$ (V) | Current at maximum power $I_{P_{max}}$ (mA) | Voltage at $V_{P_{max}}$ (V) |
| Reference cell | 0.307 | 0.5677 | 0.2100 | 0.4686 |
| 2:10 | 0.360 | 0.5800 | 0.2558 | 0.4344 |
| 3:10 | 0.424 | 0.5977 | 0.2800 | 0.4689 |
| 4:10 | 0.376 | 0.5902 | 0.3226 | 0.4547 |

**Table 5.2:** Summary of the perfomance banch mark values of $I_{sc}$, $V_{oc}$, $I_{P_{max}}$ and $V_{P_{max}}$ for the OPVs with spherical Ag NPs blended in PEDOT:PSS

There are two known parasitic resistances that affect the performance of a solar cell, namely: the series resistance and the shunt resistance. The series resistance reduces the efficiency of solar cells by dissipating power through parasitic resistances. The shunt and series resistance are estimated by taking the inverse slope near $V_{OC}$ and $I_{SC}$ respectively. Table 5.3 shows the characteristics resistance values of an OPV cell with the decoupled series and shunt resistances. The series resistance is dependent on the conductivity of the donor and acceptor layers, Therefore the mobility of each layer will thus affect the series resistance. Further it is seen that the addition of Ag NPs does not significantly changes the series resistance, meaning that Ag does not produce space charges.

On the other hand the shunt resistance is sensitive to recombination of the charge carrier at the donor–acceptor interface. Overall the shunt resistance is one order magnitude larger than the series resistance. The larger values of the shunt resistance could be attributed to pinholes or short or recombination losses at the PEDOT:PSS layer. Thus the increase of the photogenerated current could be purely due to the plasmonic effect with potential recombination at high Ag;PEDOT:PSS droplet ratios (4:10) which reduces the current.

| Organic solar cell with and without Ag NPs data analysis | | | | |
|---|---|---|---|---|
| Device (ratio of Ag NPs into PEDOT:PSS) | Current density $J_{SC}$ (mA/cm$^2$) | Characteristic resistance $R_{CH}$ (k$\Omega$ cm$^2$) | Series resistance $R_S$ ($\Omega$ cm$^2$) | Shunt resistance $R_{SH}$ ($\Omega$ cm$^2$) |
| Reference cell | 1.50 | 3.140 | 28.17 | 411.42 |
| 2:10 | 1.83 | 2.378 | 40.00 | 819.72 |
| 3:10 | 2.00 | 2.345 | 43.29 | 746.27 |
| 4:10 | 2.33 | 1.951 | 42.51 | 649.35 |

**Table 5.3:** Summary of the device characteristics parameters $J_{SC}$, $R_{CH}$, $R_S$ and $R_S$ for OPV cell with spherical Ag NPs blended in PEDOT:PSS.

The constant open circuit voltage with various series values implies the absence of recombination or short at the electrode (see figure 5.17) Thus the extra shunt resistance is negligible which makes the potential recombination site to be in the active layer. The determination of the losses can be obtained from the $(1 + R_S/R_{SH})$ ratio at various $R_S$ values. Shunt resistance increase with increase of the Ag NPs droplet concentrations while the open circuit voltage remains constant.

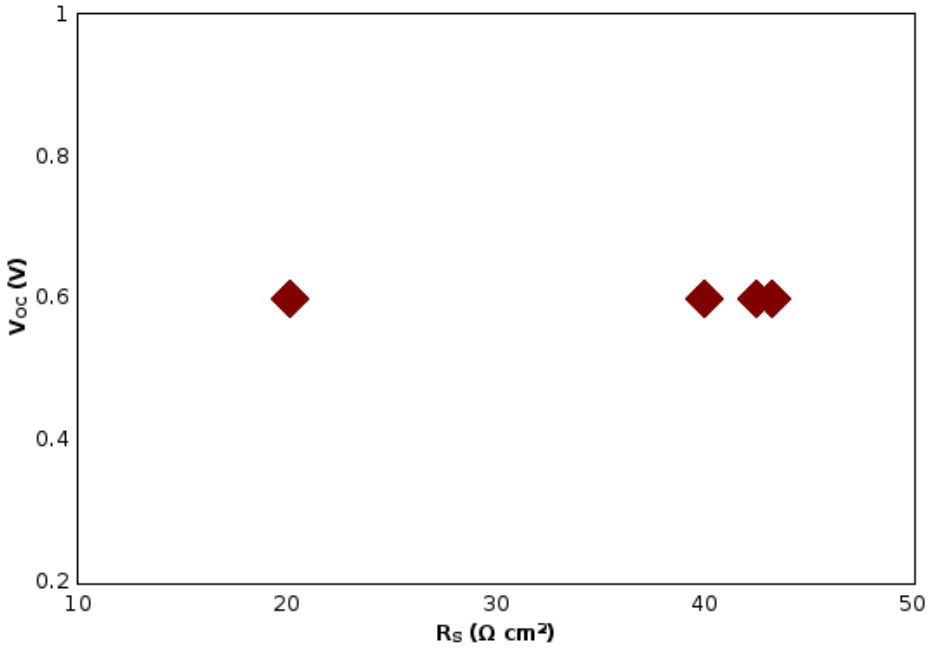



**Figure 5.17:** Shunt resistance increase at constant open circuit voltage.

A great amount of power losses are mainly caused by the presence of a shunt resistance in the device. Low shunt resistance contributes to power losses in the device by making an alternating current path for the light generated current. This diversion reduces the amount of current that flows in the device junction and reduces the voltage from the solar cell [127]. Figure 5.18 shows the current density – voltage characteristics of all the device, used for the extraction of the calculations on table 5.3.

Table 5.4 shows that maximum Power produced by the cell increases with an increase of the concentration of spherical Ag NPs and so is the efficiency of the cell. From the reference device to the device of ratio 4:10 shows that there is an increase in efficiency of up to 1.05%. This shows that the Ag NPs can enhance the efficiency of cheap solar cell through plasmonic effects. The fill factor was calculated using the following equation:

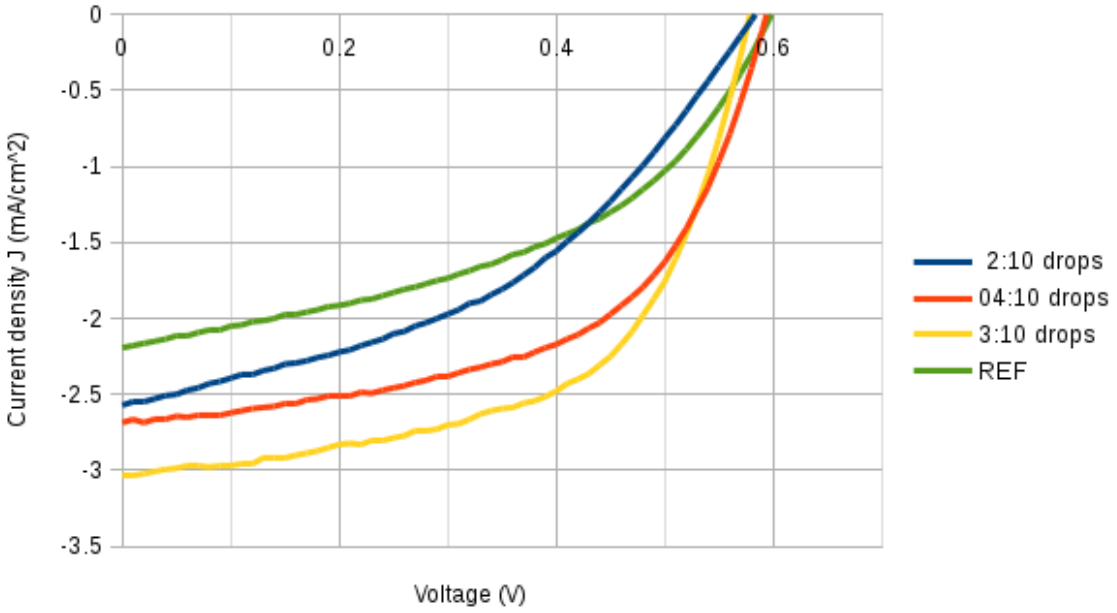



**Figure 5.18:** J-V characteristics fabricated device with varied concentration of Ag NPs in PEDOT:PSS.

$$FF = \frac{I_{P_{max}} I_{P_{max}}}{V_{oc} I_{sc}} \tag{5.4}$$

and the light incident power $P_{in}$ for efficiency calculation is 1kW/m$^2$ (AM1.5) and the area of the cell under study is : 2 mm x 7 mm = 14 mm$^2$ = 1.4×10$^{-5}$ m$^2$

then $P_{in}$ = 0.014 W and the efficiency calculated by the expression;

$$\eta = \frac{P_{max}}{P_{in}} \tag{5.5}$$

Figure 5.19 shows that the power produced by the cell increases with an increase of the concentration of spherical Ag NPs and maximum power of each device was different.

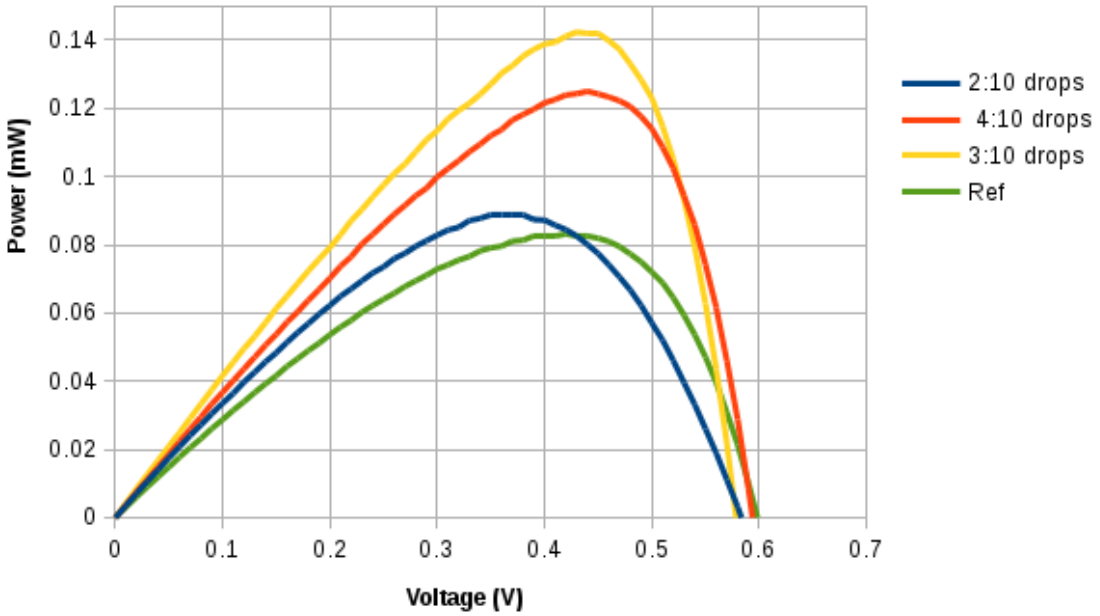



**Figure 5.19:** P-V characteristics fabricated device with varied concentration of Ag NPs in PEDOT:PSS .

Table 5.4, shows that the incorporation of Ag NPs lead to an efficiency enhancement of 50% in respect to the reference device. An increase in efficiency of 12.9 % is observed when compared to the efficiency of the reference cell, for the cell with two drops of the Ag NPs blended into 10 drops of PEDOT:PSS (2:10). Similarly for the cells with the ratios 3:10 and 4:10 the increase went up by 33.4% and 50% compared to the cell with no Ag NPs (reference cell). All in all the highest efficiency achieved for the OPV solar cell was 1.05% while that of the reference cell was measured to 0.70%. The Ag NPs has improved the performance of a solar cell for all the devices investigated.

| Organic solar cell with and without Ag NPs data analysis | | | |
|---|---|---|---|
| Device (ratio of Ag NPs into PEDOT:PSS) | Maximum power $P_{max}$ (mW) | Fill factor | Efficiency $\eta$ |
| Reference cell | 0.984 | 0.5363 | 0.70 % |
| 2:10 | 1.111 | 0.5437 | 0.79 % |
| 3:10 | 1.313 | 0.5339 | 0.94 % |
| 4:10 | 1.480 | 0.6671 | 1.05 % |

**Table 5.4:** Summary of the performance (including Power produced by the cell and photo convertion efficiency) of the OPVs with spherical Ag NPs blended in PEDOT:PSS.

The possible diffusion of oxygen ($O_2$) into the active layer because of the pinholes in aluminium electrode is likely to degrade the P3HT:PCBM blend by forming charge transfer complexes with $O_2$ [128]. This is one of the leading factor of having low efficiency in the device. There are other factors which leads to a low efficiency such as an increase in the series resistance on the cell. A lower shunt resistance engenders to power loss in the cell.

## 5.5 Morphology of $SiO_2 - HfO_2$ planar waveguides

Figure 5.24 shows the SEM images of $SiO_2 - HfO_2$ planar waveguides activated by $Eu^{3+}$ as synthesised by sol-gel technique and were deposited through dip coating. The samples were charging in the SEM and therefore were coated with gold palladium to see the structures. SEM shows that the surface is smooth, except for the pinholes on the surface which may have resulted during the deposition of the sample on the substrate. EDS analysis have verified the presence of Hf, Si and Eu. Au and Pd have been attributed to the coating described above. The planar silica-hafnia waveguides shows full densification and no phase separation at wavelength scale.

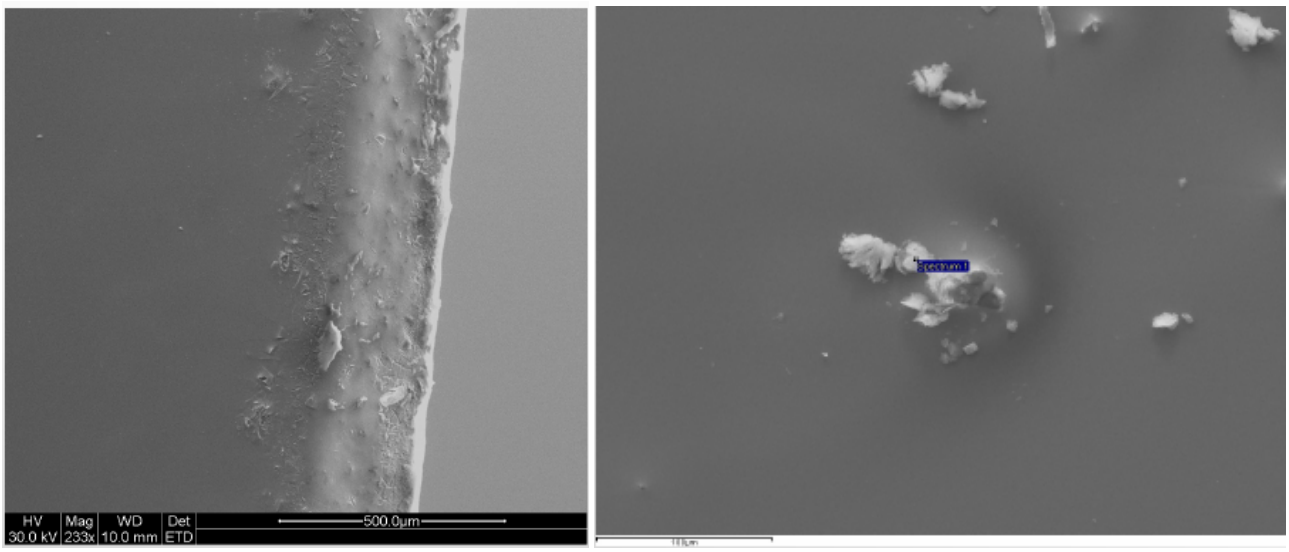



**Figure 5.20:** $SiO_2 - HfO_2$ waveguide at the edge (left) and at the surface (right) of the sample

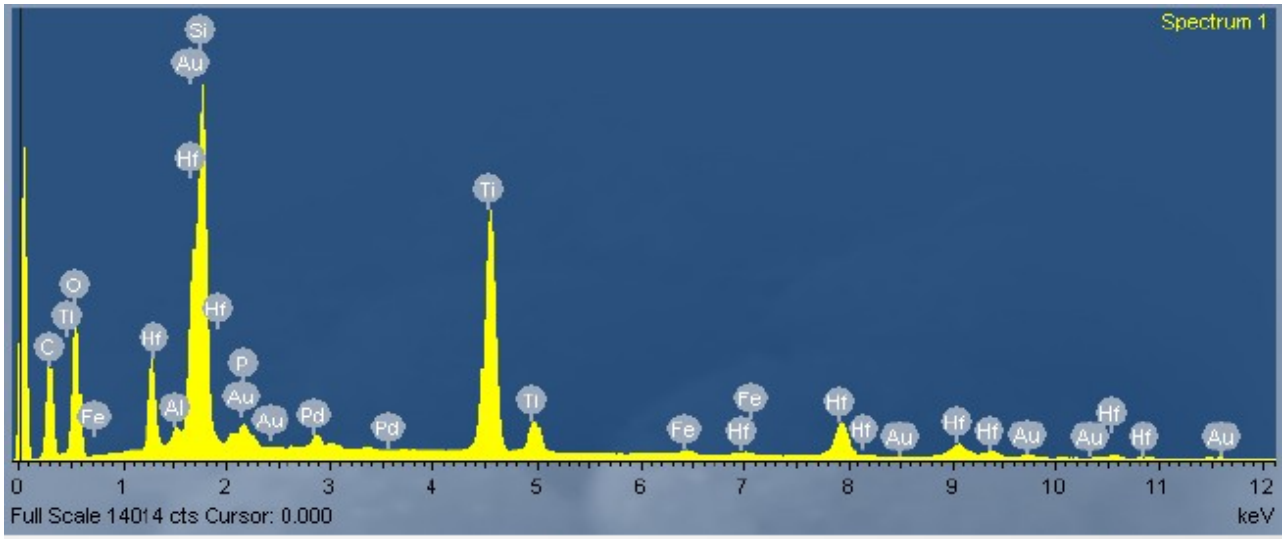



**Figure 5.21:** EDS analysis of $SiO_2 - HfO_2$ waveguides

## 5.6 M-line spectroscopy measurement for planar silica-hafnia waveguides

A method to measure the thickness of the layer between the prism and the waveguide in a reflecting prism coupler is proposed such as M-line spectroscopy. To perform measurements of the refractive indices and thickness of planar waveguides, a knowledge of the prism's characteristics and to accurately measure the angles is required [129].

M-line spectroscopy measurement were performed to obtain refractive index and the thickness of the waveguides as shown in figure 5.22 using for two modes, namely: the Transverse Magnetic (TM) and the Transverse Electric (TE) modes excited at 632.8 nm. Using this technique the thickness and the refractive index were determined to be:

1. Thickness : 1.4951 $\mu$m
2. Refractive index: 1.5848

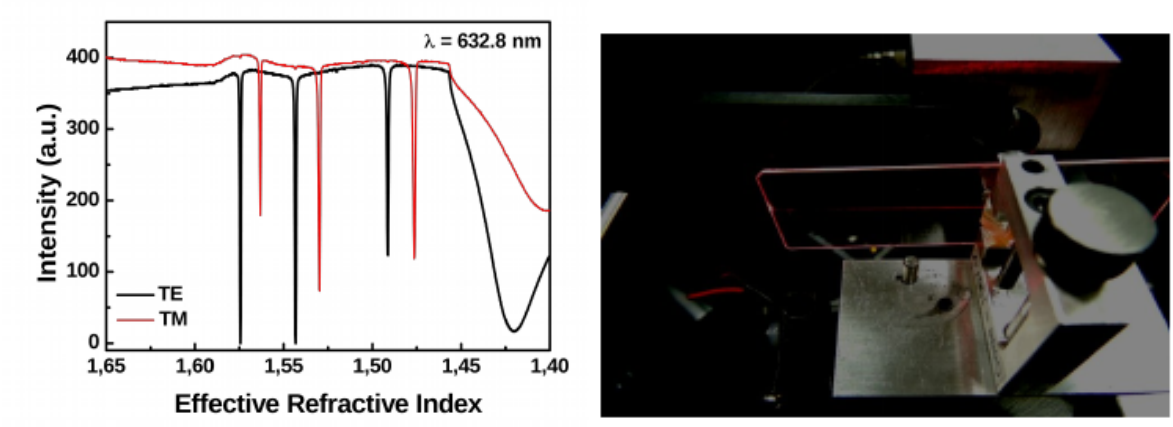



**Figure 5.22:** M-line measurement for both modes TE and TM

The planar silica-hafnia waveguides doped with $Eu^{3+}$ are full densified and share no phase separation at wavelength scale. The measured refractive index and thickness

sustains a single mode at 1.5$\mu$m, which has a long lifetime and which can be used in photovoltaic device.

## 5.7 Photoluminescence properties of europium doped silica-hafnia waveguides

The photoluminescence characterization of $SiO_2 - HfO_2$ planar waveguides activated with $Eu^{3+}$ (Has long lifetime and mostly radiative) were studied with an argon ion laser at a excitation wavelength of 488 nm. The emission lines due to the rare earth ions. $Eu^{3+}$ in the planar waveguide are shown in (fig 5.23).

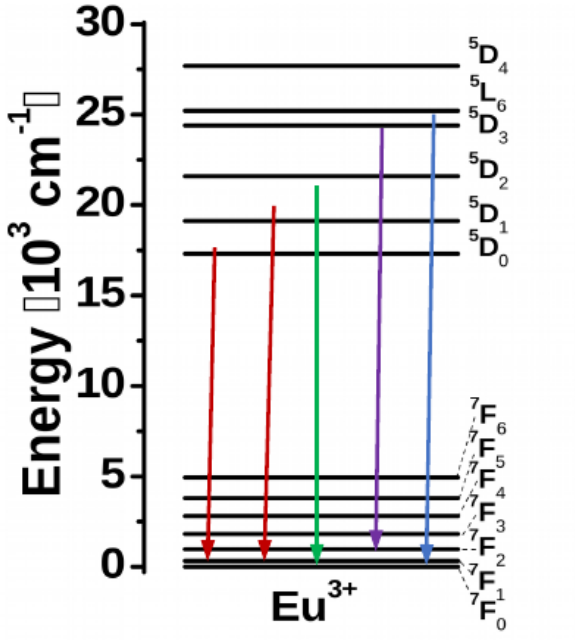



**Figure 5.23:** Energy level diagram for $Eu^{3+}$ ions.

Figure 5.24 shows the measured photoluminescence spectrum of the 70Si:30Hf:$Eu^{3+}$ waveguide. The measurements were done at room temperature. The emission spectrum exhibits four typical emission peaks in the range of 560–700 nm, which result from

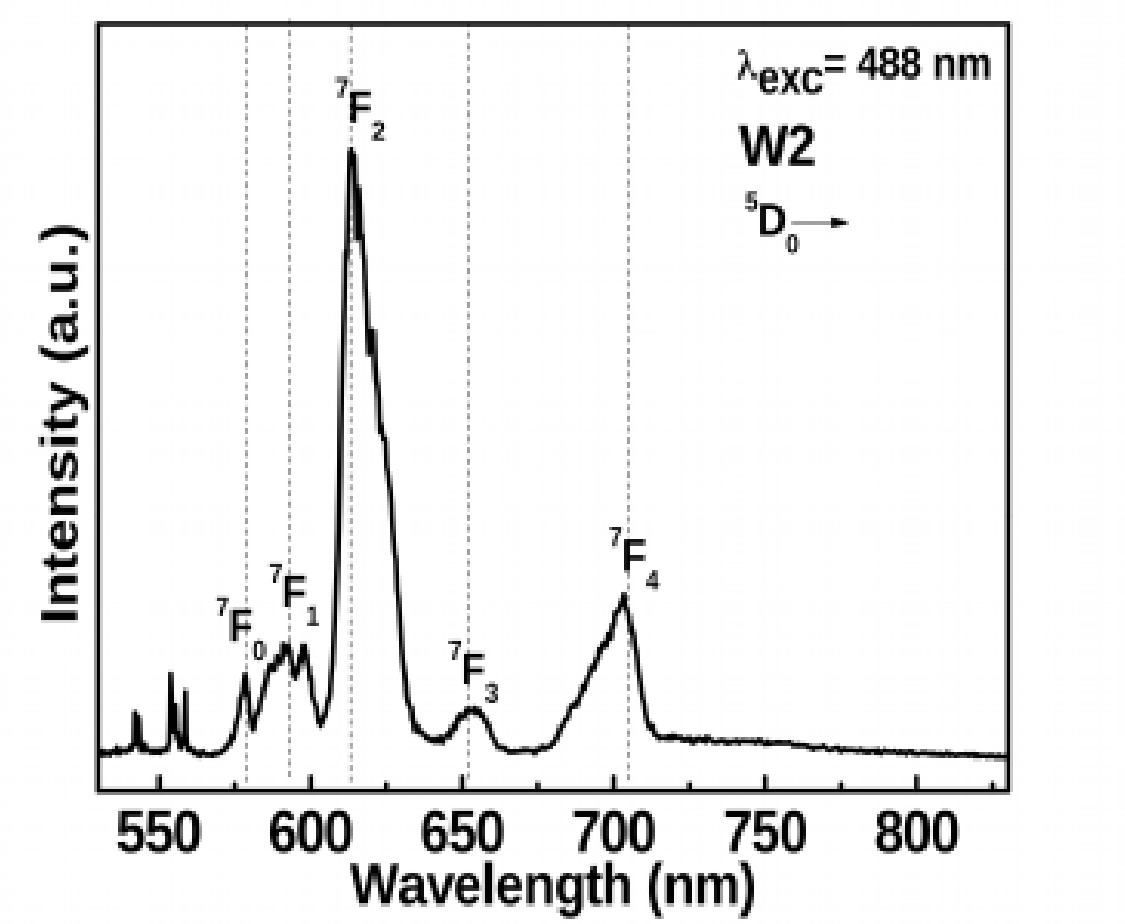



**Figure 5.24:** Room temperature photolumensence spectrum of $Eu^{3+}$ doped $SiO_2 - HfO_2$.

$^5D_0 \longrightarrow ^7 F_J$ (J = 0, 1, 2, 3 and 4) transitions. The strong emission peak at 613 nm is ascribed to an electric dipole transition from $^5D_0 \longrightarrow ^7 F_2$ of $Eu^{3+}$, while the emission near 593 nm is assigned to a magnetic dipole transition starting from $^5D_0 \longrightarrow ^7 F_1$ of $Eu^{3+}$. Moreover, there are two weak emission peaks located at 580 and 652 nm, which are ascribed to $^5D_0 \longrightarrow ^7 F_0$ and $^5D_0 \longrightarrow ^7 F_3$ transitions of $Eu^{3+}$, respectively.

From the parity selection rule, when $Eu^{3+}$ ions are located in position with an inversion symmetric center, the $^5D_0 \longrightarrow ^7 F_1$ magnetic dipole transition is allowed, which gives an orange red emission at about 590 nm. But if the ions are located at a position

without an inversion symmetric center, because of the opposite parity 5d configuration is mixed into $4f^n$ configuration, this may lift the parity selection. Thus the f-f forbidden transition are partially released, like the hypersensitive $^5D_0 \longrightarrow ^7 F_2$ electric dipole transition will be allowed, which gives in the red emission at around 613 nm and $^5D_0 \longrightarrow ^7 F_4$ bands lie at longer wavelengths (705 nm) and are restricted by the energies of the $^7F_4$ crystal states below the $^5D_0$ electronic state so it has weak features. For $Si/Hf$ waveguide activated by $Eu^{3+}$, the strongest red emission peak located at 613 nm is observed. It may be presumed that the $Eu^{3+}$ ions mainly occupy the non-inversion symmetric center in host lattice.

# Conclusions

This research project focused on Ag NPs grown by chemical reduction process. The time of reactions were varied during Ag NPs synthesis, TEM images showed that Ag NPs of different shapes and sizes were formed at the reaction times. As such the formation of spherical, prism (triangular) like and fully agglomerated prism like shapes with diameters of 15, 14 and 16 nm respectively, were obtained. The resonance of the Ag NPs absorption spectra were in the range of 400 nm and 500 nm. A good agreement of the resonance absorption cross–section determined FDTD methods based on MEEP software have been established. Our simulations have shown the dependencies of the scattering and absorption cross-sections on the size of the particles.

The dependence of the scattering and absorption cross-section of Ag NPs with different size has been established by MEEP software based on the modified Drude-Lorentz model and it is in good agreement with the experimental data.

In order to compare the enhancement efficiencies, a reference cell was fabricated in this format: ITO/PEDOT:PSS/P3HT:PCBM/Al. Then device was annealed at temperature of 50 $^oC$ in Ar gas for 15 minutes. Then device was the incorporated with different drops concentration Ag NPs blended in PEDOT:PSS such that the device was in this design ITO/Ag NPs + PEDOT:PSS/P3HT:PCBM/Al which showed a showed good performance (varying from the ratio 2:10, 3:10 and 4:10). The enhancement efficiency was increased from 0.70% to 1.05% for diverse concentrations of spherical Ag NPs and corresponding to a 50% increase in efficiency attributed to surface plasmon resonance effect. The incorporation of Ag NPs in PEDOT:PSS of organic solar cells, has shown

an efficiency enhancement

The optical analysis from UV-Vis spectrometer showed an enhancement in absorption with different particle shape and sizes. The increase in the ratio of Ag NPs blended in PEDOT:PSS is seen in the enhancement of $I_{sc}$ and $P_{max}$. The incorporation of Ag NPs in PEDOT:PSS of organic solar cells does not change the $V_{oc}$ and $R_S$ significantly.

Enhancing light harvesting has led to greater generation of exciton hence the increase in $I_{sc}$ and $P_{max}$. The results depict an increase in efficiency enhancement after incorporation of Ag NPs. The $P_{max}$ and $J_{sc}$ went up by 51% and 53.5%, respectively, from the reference cell to the cell with Ag NPs.

The planar silica-hafnia waveguides doped with $Eu^{3+}$ are full densified and share no phase separation at wavelength scale. The measured refractive index and thickness sustains a single down converted mode at 1.5$\mu$m, which has a long lifetime and can be used in light trapping in the photovoltaic device. Both two approaches holds a great promise in the enhancement and tuning optical absorption in solar cells.

# Future research

In the course of this project, several exciting ideas on the efficient conversion of solar energy to electricity have been proposed. These ideas range from the modification of polymer blend to match band gap at which the light emission is maximum to the use of light management schemes. In this respect, the following should be explored for future work:

- The need to incorporate and vary concentrations of the Ag Nps directly in the PCBM:P3HT blend and examine the contribution of scattering and absorption.
- The effect of multi-junction can be studied by incorporating Ag and Au NPs together on the device so that the absorption may be tuned sequentially.
- Ag NPs heats up when exposed to light for a long time, a follow up study should be done understand the phenomena and its effects on efficiency.
- Implementing waveguides into the organic solar cell through applying quantum cutting and up conversion layers.
- Study the effect of up and down conversion on organic solar cell doped with rare-earth elements. This is essential especially in cases which involves the mechanisms of energy transfer in dual rare earth ions.
- Implement photonic crystal structures in OPV device.
- Combination of Ag NPs surface plasmonic resonance with up and down conversion characteristics to enhance efficiency in OPVs.

# Bibliography


[1] Ibrahim Dincer. Renewable energy and sustainable development: a crucial review. *Renewable and Sustainable Energy Reviews*, 4(2):157–175, 2000.

[2] Muhammad Asif and Tariq Muneer. Energy supply, its demand and security issues for developed and emerging economies. *Renewable and Sustainable Energy Reviews*, 11(7):1388–1413, 2007.

[3] ND Kaushika and Anil K Rai. An investigation of mismatch losses in solar photovoltaic cell networks. *Energy*, 32(5):755–759, 2007.

[4] Prashant V Kamat. Meeting the clean energy demand: nanostructure architectures for solar energy conversion. *The Journal of Physical Chemistry C*, 111(7):2834–2860, 2007.

[5] Markus C Scharber, David Mühlbacher, Markus Koppe, Patrick Denk, Christoph Waldauf, Alan J Heeger, and Christoph J Brabec. Design rules for donors in bulk-heterojunction solar cells—towards 10% energy-conversion efficiency. *Advanced materials*, 18(6):789–794, 2006.

[6] Lawrence Kazmerski, D Gwinner, and A Hicks. Best research-cell efficiencies. *National Renewable Energy Laboratory*, 2010.

[7] S Fischer, JC Goldschmidt, P Löper, GH Bauer, R Brüggemann, K Krämer, D Biner, M Hermle, and SW Glunz. Enhancement of silicon solar cell efficiency by upconversion: Optical and electrical characterization. *Journal of Applied Physics*, 108(4):044912, 2010.

[8] Umesh Kulshrestha and SE Jorgensen. Encyclopedia of environmental management. *Gas*, 6(7):8, 2013.

[9] Markus C Scharber, David Mühlbacher, Markus Koppe, Patrick Denk, Christoph Waldauf, Alan J Heeger, and Christoph J Brabec. Design rules for donors in bulk-heterojunction solar cells—towards 10% energy-conversion efficiency. *Advanced Materials*, 18(6):789–794, 2006.

[10] Sung Heum Park, Anshuman Roy, Serge Beaupre, Shinuk Cho, Nelson Coates, Ji Sun Moon, Daniel Moses, Mario Leclerc, Kwanghee Lee, and Alan J Heeger. Bulk heterojunction solar cells with internal quantum efficiency approaching 100&percnt. *Nature photonics*, 3(5):297–302, 2009.

[11] Wayne Hu and Joseph Silk. Thermalization constraints and spectral distortions for massive unstable relic particles. *Physical review letters*, 70(18):2661, 1993.

[12] Stefan Alexander Maier. *Plasmonics: fundamentals and applications*. Springer Science & Business Media, United Kingdom, 2007.

[13] Mei Xue, Lu Li, Bertrand J Tremolet de Villers, Huajun Shen, Jinfeng Zhu, Zhibin Yu, Adam Z Stieg, Qibing Pei, Benjamin J Schwartz, and Kang L Wang. Charge-carrier dynamics in hybrid plasmonic organic solar cells with ag nanoparticles. *Applied Physics Letters*, 98(25):253302, 2011.

[14] Marjan Saboktakin, Xingchen Ye, Soong Ju Oh, Sung-Hoon Hong, Aaron T Fafarman, Uday K Chettiar, Nader Engheta, Christopher B Murray, and Cherie R Kagan. Metal-enhanced upconversion luminescence tunable through metal nanoparticle–nanophosphor separation. *ACS nano*, 6(10):8758–8766, 2012.

[15] MC Brierley and PW France. Neodymium-doped fluoro-zirconate fibre laser. *Electronics Letters*, 23:815–817, 1987.

[16] J Silver, MI Martinez-Rubio, TG Ireland, GR Fern, and R Withnall. Yttrium oxide upconverting phosphors. 3. upconversion luminescent emission from

europium-doped yttrium oxide under 632.8 nm light excitation. *The Journal of Physical Chemistry B*, 105(38):9107–9112, 2001.

[17] J De Wild, JK Rath, A Meijerink, WGJHM Van Sark, and REI Schropp. Enhanced near-infrared response of a-si: H solar cells with $\beta$-nayf 4: Yb 3+(18%), er 3+(2%) upconversion phosphors. *Solar energy materials and solar cells*, 94(12):2395–2398, 2010.

[18] T Trupke, MA Green, and P Würfel. Improving solar cell efficiencies by up-conversion of sub-band-gap light. *Journal of Applied Physics*, 92(7):4117–4122, 2002.

[19] Georg Klein. Light sources, types of colorants, observer. In *Industrial Color Physics*, pages 11–131. Springer, New York, 2010.

[20] Alexandre G Brolo. Plasmonics for future biosensors. *Nature Photonics*, 6(11):709–713, 2012.

[21] VAG Rivera, SPA Osorio, Y Ledemi, D Manzani, Younes Messaddeq, LAO Nunes, and E Marega. Localized surface plasmon resonance interaction with er 3+-doped tellurite glass. *Optics express*, 18(24):25321–25328, 2010.

[22] Mark I Stockman. Nanoplasmonics: past, present, and glimpse into future. *Optics express*, 19(22):22029–22106, 2011.

[23] Kevin C Hewitt. Nano-raman spectroscopy: Instrument design and techniques. *Phys. Canada*, 62:49–54, 2006.

[24] Herbert Zimmermann, Matthias Zebisch, and Norbert Sträter. Cellular function and molecular structure of ecto-nucleotidases. *Purinergic signalling*, 8(3):437–502, 2012.

[25] Dieter K Schroder. Surface voltage and surface photovoltage: history, theory and applications. *Measurement Science and Technology*, 12(3):R16, 2001.

[26] Carsten Olbrich, Johan Strumpfer, Klaus Schulten, and Ulrich Kleinekathofer. Quest for spatially correlated fluctuations in the fmo light-harvesting complex. *The Journal of Physical Chemistry B*, 115(4):758–764, 2010.

[27] C Tanase, EJ Meijer, PWM Blom, and DM De Leeuw. Unification of the hole transport in polymeric field-effect transistors and light-emitting diodes. *Physical Review Letters*, 91(21):216601, 2003.

[28] Henning Sirringhaus, PJ Brown, RH Friend, Martin Meedom Nielsen, Klaas Bechgaard, BMW Langeveld-Voss, AJH Spiering, Rene AJ Janssen, EW Meijer, P Herwig, et al. Two-dimensional charge transport in self-organized, high-mobility conjugated polymers. *Nature*, 401(6754):685–688, 1999.

[29] Yang Shen and Mool C Gupta. Investigation of electrical characteristics of p3ht: Pcbm organic solar cells. In *Photovoltaic Specialists Conference (PVSC), 2012 38th IEEE*, pages 002770–002774. IEEE, 2012.

[30] Arvind Shah, P Torres, Reto Tscharner, N Wyrsch, and H Keppner. Photovoltaic technology: the case for thin-film solar cells. *Science*, 285(5428):692–698, 1999.

[31] Florian Machui, Stefan Langner, Xiangdong Zhu, Steven Abbott, and Christoph J Brabec. Determination of the p3ht: Pcbm solubility parameters via a binary solvent gradient method: Impact of solubility on the photovoltaic performance. *Solar Energy Materials and Solar Cells*, 100:138–146, 2012.

[32] Jenny Nelson. Organic photovoltaic films. *Current Opinion in Solid State and Materials Science*, 6(1):87–95, 2002.

[33] Josiah Walton. *The search for majoron emission in xenon-136 and two-neutrino double-beta decay of xenon-134 with the Enriched Xenon Observatory*. PhD thesis, University of Illinois at Urbana-Champaign, 2016.

[34] H Bässler. Localized states and electronic transport in single component organic solids with diagonal disorder. *Physica status solidi (b)*, 107(1):9–54, 1981.

[35] Sean E Shaheen, Christoph J Brabec, N Serdar Sariciftci, Franz Padinger, Thomas Fromherz, and Jan C Hummelen. 2.5% efficient organic plastic solar cells. *Applied Physics Letters*, 78(6):841–843, 2001.

[36] Changqi Ma and Zheng Cui. Printed organic thin film solar cells. *Printed Electronics: Materials, Technologies and Applications*, page 201, 2016.

[37] Jean-Michel Nunzi. Organic photovoltaic materials and devices. *Comptes Rendus Physique*, 3(4):523–542, 2002.

[38] Loucas Tsakalakos. *Nanotechnology for photovoltaics*. CRC press, USA, 2010.

[39] Peter Würfel and Uli Würfel. *Physics of solar cells: from basic principles to advanced concepts*. John Wiley & Sons, Freiburg/Germany, 2009.

[40] Serap Günes, Helmut Neugebauer, and Niyazi Serdar Sariciftci. Conjugated polymer-based organic solar cells. *Chemical reviews*, 107(4):1324–1338, 2007.

[41] Marius Albota, David Beljonne, Jean-Luc Brédas, Jeffrey E Ehrlich, Jia-Ying Fu, Ahmed A Heikal, Samuel E Hess, Thierry Kogej, Michael D Levin, Seth R Marder, et al. Design of organic molecules with large two-photon absorption cross sections. *Science*, 281(5383):1653–1656, 1998.

[42] JE Ehrlich, XL Wu, I-YS Lee, Z-Y Hu, H Röckel, SR Marder, and JW Perry. Two-photon absorption and broadband optical limiting with bis-donor stilbenes. *Optics Letters*, 22(24):1843–1845, 1997.

[43] BAO JI. *A study of a-Fe2O3 thin films for the oxygen evolution reaction in water photolysis*. PhD thesis, National University of Singapore, 2010.

[44] William Shockley and Hans J Queisser. Detailed balance limit of efficiency of p-n junction solar cells. *Journal of applied physics*, 32(3):510–519, 1961.

[45] Eric W McFarland and Jing Tang. A photovoltaic device structure based on internal electron emission. *Nature*, 421(6923):616–618, 2003.

[46] Recombination losses. http://www.pveducation.org/pvcdrom/design/recombination-losses. Accessed on 18-06-2016.

[47] Jenny Nelson et al. *The physics of solar cells*, volume 1. World Scientific, London: Imperial college, 2003.

[48] Tayebeh Ameri, Gilles Dennler, Christoph Lungenschmied, and Christoph J Brabec. Organic tandem solar cells: a review. *Energy & Environmental Science*, 2(4):347–363, 2009.

[49] JJM Halls, K Pichler, RH Friend, SC Moratti, and AB Holmes. Exciton diffusion and dissociation in a poly (p-phenylenevinylene)/c60 heterojunction photovoltaic cell. *Applied Physics Letters*, 68(22):3120–3122, 1996.

[50] M Theander, Arkady Yartsev, Donatas Zigmantas, Villy Sundström, W Mammo, MR Andersson, and Olle Inganäs. Photoluminescence quenching at a polythiophene/c 60 heterojunction. *Physical Review B*, 61(19):12957, 2000.

[51] Yen-Ju Cheng, Sheng-Hsiung Yang, and Chain-Shu Hsu. Synthesis of conjugated polymers for organic solar cell applications. *Chemical reviews*, 109(11):5868–5923, 2009.

[52] Harald Hoppe and Niyazi Serdar Sariciftci. Organic solar cells: An overview. *Journal of Materials Research*, 19(07):1924–1945, 2004.

[53] Gang Yu, Jun Gao, Jan C Hummelen, Fred Wudl, and Alan J Heeger. Polymer photovoltiac cells: Enhanced efficiencies via a network of internal donor-acceptor heterojunctions. *Science*, 270(5243):1789, 1995.

[54] Markus C Scharber and Niyazi Serdar Sariciftic. Efficiency of bulk-heterojunction organic solar cell. *Progress in polymer science*, 38(12):1929–1940, 2013.

[55] Dan Chi, Shengchun Qu, Zhanguo Wang, and Jizheng Wang. High efficiency p3ht: Pcbm solar cells with an inserted pcbm layer. *Journal of Materials Chemistry C*, 2(22):4383–4387, 2014.

[56] Li-Min Chen, Ziruo Hong, Gang Li, and Yang Yang. Recent progress in polymer solar cells: manipulation of polymer: fullerene morphology and the formation of efficient inverted polymer solar cells. *Advanced Materials*, 21(14-15):1434–1449, 2009.

[57] Lukas Schmidt-Mende, Andreas Fechtenkötter, Klaus Müllen, Ellen Moons, Richard H Friend, and JD MacKenzie. Self-organized discotic liquid crystals for high-efficiency organic photovoltaics. *Science*, 293(5532):1119–1122, 2001.

[58] Gang Li, Rui Zhu, and Yang Yang. Polymer solar cells. *Nature Photonics*, 6(3):153–161, 2012.

[59] Almantas Pivrikas, Niyazi Serdar Sariciftci, Gytis Juška, and Ronald Österbacka. A review of charge transport and recombination in polymer/fullerene organic solar cells. *Progress in Photovoltaics: Research and Applications*, 15(8):677–696, 2007.

[60] Dieter Wöhrle and Dieter Meissner. Organic solar cells. *Advanced Materials*, 3(3):129–138, 1991.

[61] Joseph M Marshall and Doriana Dimova-Malinovska. *Photovoltaic and Photoactive Materials: Properties, Technology and Applications*, volume 80. Springer Science & Business Media, 2012.

[62] Andreas Baumann, Tom J Savenije, Dharmapura Hanumantharaya K Murthy, Martin Heeney, Vladimir Dyakonov, and Carsten Deibel. Influence of phase segregation on recombination dynamics in organic bulk-heterojunction solar cells. *Advanced Functional Materials*, 21(9):1687–1692, 2011.

[63] Wendy U Huynh, Janke J Dittmer, and A Paul Alivisatos. Hybrid nanorod-polymer solar cells. *Science*, 295(5564):2425–2427, 2002.

[64] Harry A Atwater and Albert Polman. Plasmonics for improved photovoltaic devices. *Nature materials*, 9(3):205–213, 2010.

[65] P Apell, R Monreal, and S Lundqvist. Photoluminescence of noble metals. *Physica Scripta*, 38(2):174, 1988.

[66] Tigran V Shahbazyan. Theory of plasmon-enhanced metal photoluminescence. *Nano letters*, 13(1):194–198, 2012.

[67] Peter Apell, R Monreal, and Stig Lundqvist. Photoluminescence of noble metals. *Physica Scripta*, 38(2):174, 1988.

[68] A Mooradian. Photoluminescence of metals. *Physical Review Letters*, 22(5):185, 1969.

[69] GT Boyd, ZH Yu, and YR Shen. Photoinduced luminescence from the noble metals and its enhancement on roughened surfaces. *Physical Review B*, 33(12):7923, 1986.

[70] Stefania Massari and Marcello Ruberti. Rare earth elements as critical raw materials: Focus on international markets and future strategies. *Resources Policy*, 38(1):36–43, 2013.

[71] VAG Rivera, E Marega Jr, and FA Ferri. *Localized surface plasmon resonances: noble metal nanoparticle interaction with rare-earth ions*. Intech Open Access Publisher,DOI: 10.5772/50753, 2012.

[72] BR Judd. Optical absorption intensities of rare-earth ions. *Physical Review*, 127(3):750, 1962.

[73] JR Simpson. Rare earth doped fiber fabrication: techniques and physical properties. *Optica Engeneering-New York-Marcel Dekker Incoparated*, 71:1–16, 2001.

[74] Shigeki Tokita, Junji Kawanaka, Yasukazu Izawa, Masayuki Fujita, and Toshiyuki Kawashima. 23.7-w picosecond cryogenic-yb: Yag multipass amplifier. *Optics express*, 15(7):3955–3961, 2007.

[75] PP Sorokin and MJ Stevenson. Stimulated infrared emission from trivalent uranium. *Physical Review Letters*, 5(12):557, 1960.

[76] CA Morrison and RP Leavitt. Crystal-field analysis of triply ionized rare earth ions in lanthanum trifluoride. *The Journal of Chemical Physics*, 71(6):2366–2374, 1979.

[77] J Keyne, DM Binnie, J Carr, NC Debenham, A Duane, DA Garbutt, WG Jones, I Siotis, and JG McEwen. Study of $\omega$ production near threshold in the reaction $\pi$- p$\longrightarrow \omega$ n. *Physical Review D*, 14(1):28, 1976.

[78] Stefan Hufner. *Optical spectra of transparent rare earth compounds*. Accedemic press, New York, 2012.

[79] NC Chang, John B Gruber, Richard P Leavitt, and Clyde A Morrison. Optical spectra, energy levels, and crystal-field analysis of tripositive rare earth ions in y2o3. i. kramers ions in c2 sites. *The Journal of Chemical Physics*, 76(8):3877–3889, 1982.

[80] VAG Rivera, OB Silva, Y Ledemi, Younés Messaddeq, and E Marega Jr. *Collective Plasmon-Modes in Gain Media: Quantum Emitters and Plasmonic Nanostructures*. Springer,New York, 2014.

[81] Vera Cantale. *Towards label-free biosensors based on localized surface plasmon resonance*. PhD thesis, Università degli Studi di Ferrara, 2011.

[82] Yao Zhang, Zhangjian Li, and Baojun Li. Multimode interference effect and self-imaging principle in two-dimensional silicon photonic crystal waveguides for terahertz waves. *Optics Express*, 14(7):2679–2689, 2006.

[83] Ezequiel R Encina and Eduardo A Coronado. On the far field optical properties of ag- au nanosphere pairs. *The Journal of Physical Chemistry C*, 114(39):16278–16284, 2010.

[84] Chengteh Lee, Weitao Yang, and Robert G Parr. Development of the colle-salvetti correlation-energy formula into a functional of the electron density. *Physical review B*, 37(2):785, 1988.

[85] Lukas Novotny and Bert Hecht. *Principles of nano-optics*. Cambridge university press, Cambridge, 2012.

[86] John David Jackson. *Classical electrodynamics*. Wiley, New York, 1999.

[87] Edward M Purcell and Carlton R Pennypacker. Scattering and absorption of light by nonspherical dielectric grains. *The Astrophysical Journal*, 186:705–714, 1973.

[88] $finite - difference - time - domain - method$. `https://en.wikipedia.org/wiki/Finite-difference_time-domain_method`. Accessed on 29-02-2016.

[89] Robert Warmbier Faris Mohammed and Alexander Quandt. plasmonics. 2016.

[90] Ardavan F Oskooi, David Roundy, Mihai Ibanescu, Peter Bermel, John D Joannopoulos, and Steven G Johnson. Meep: A flexible free-software package for electromagnetic simulations by the fdtd method. *Computer Physics Communications*, 181(3):687–702, 2010.

[91] Max Born and Emil Wolf. *Principles of optics: electromagnetic theory of propagation, interference and diffraction of light*. Pergamon press, Oxford, 1970.

[92] Robert G Hunsperger. Theory of optical waveguides. In *Integrated Optics: Theory and Technology*, pages 30–45. Springer, Berlin Heidelberg, 1991.

[93] Harry JR Dutton. Understanding optical communications, international technical support organization, 1998.

[94] Herwig Kogelnik. 2. theory of dielectric waveguides. In *Integrated optics*, pages 13–81. Springer, Berlin Heidelberg, 1975.

[95] Tsutomu Kitoh Kenji Kawano. *Introduction to Optical Waveguide Analysis: Solving Maxwell's Equations and the SchroÈdinger Equation.* John Wiley & Sons, New York, 2001.

[96] Xiao-Qiong Qi and Jia-Ming Liu. Photonic microwave applications of the dynamics of semiconductor lasers. *Selected Topics in Quantum Electronics, IEEE Journal of*, 17(5):1198–1211, 2011.

[97] Allan W Snyder and John Love. *Optical waveguide theory.* Springer Science & Business Media, New York, 2012.

[98] Mauro Epifani, Cinzia Giannini, Leander Tapfer, and Lorenzo Vasanelli. Sol-gel synthesis and characterization of ag and au nanoparticles in sio2, tio2, and zro2 thin films. *Journal of the American Ceramic Society*, 83(10):2385–2393, 2000.

[99] Isabel Pastoriza-Santos and Luis M Liz-Marzán. Formation and stabilization of silver nanoparticles through reduction by n, n-dimethylformamide. *Langmuir*, 15(4):948–951, 1999.

[100] Dip Singh Gill, Balwinder Arora, Kailash Chandra Pathak, Inder Mohan Joshi, and Mandeep Singh Bakshi. Transference number and conductance studies of agno 3 in water–organic solvent mixtures at 25 c. *Journal of the Chemical Society, Faraday Transactions*, 88(1):57–60, 1992.

[101] Shabbir A Bashar. Study of indium tin oxide (ito) for novel optoelectronic devices. *University of Manchester Institute of Science and Technology, Manchester*, pages 106–109, 1998.

[102] Robley C Williams. Plating by thermal evaporation, May 11 1937. US Patent 2,079,784.

[103] Mahesh Chand Sharma, Balram Tripathi, Sumit Kumar, Subodh Srivastava, and YK Vijay. Low cost cuinse 2 thin films production by stacked elemental layers process for large area fabrication of solar cell application. *Materials Chemistry and Physics*, 131(3):600–604, 2012.

[104] Pavithra Prashanth. Thermal evaporation. *Equipment technologist Center for Excellence in Nanoelectronics Indian Institute of Science*, pages 1–18, 1998.

[105] C Jeffrey Brinker and George W Scherer. *Sol-gel science: the physics and chemistry of sol-gel processing*. Academic press, New York, 2013.

[106] Renata Reisfeld and Christian K JØrgensen. *Optical properties of colorants or luminescent species in sol-gel glasses*. Springer, Berlin Heidelberg,, 1992.

[107] Larry L Hench and Jon K West. The sol-gel process. *Chemical Reviews*, 90(1):33–72, 1990.

[108] Bakul C Dave, Bruce Dunn, Joan Selverstone Valentine, and Jeffrey I Zink. Sol-gel encapsulation methods for biosensors. *Analytical Chemistry*, 66(22):1120A–1127A, 1994.

[109] Yunfeng Lu, Rahul Ganguli, Celeste A Drewien, Mark T Anderson, C Jeffrey Brinker, Weilang Gong, Yongxing Guo, Hermes Soyez, Bruce Dunn, Michael H Huang, et al. Continuous formation of supported cubic and hexagonal mesoporous films by sol–gel dip-coating. *Nature*, 389(6649):364–368, 1997.

[110] Sem explanation. `https://www.wits.ac.za/research/mmu/microscopy%20and%20microanalysis%20unit/techniques/22232/scanning_electron_microscope_sem.html#SEM`. Accessed on 18-05-2016.

[111] Michael F Toney, Jason N Howard, Jocelyn Richer, Gary L Borges, Joseph G Gordon, Owen R Melroy, David G Wiesler, Dennis Yee, and Larry B Sorensen. Distribution of water molecules at ag (111)/electrolyte interface as studied with surface x-ray scattering. *Surface science*, 335:326–332, 1995.

[112] Rolf Fandrich, Ying Gu, Debra Burrows, and Kurt Moeller. Modern sem-based mineral liberation analysis. *International Journal of Mineral Processing*, 84(1):310–320, 2007.

[113] Nicolle NP Moonen and François Diederich. Limitations on the use of uv/vis spectroscopy for the evaluation of conjugation effectiveness. *Organic & biomolecular chemistry*, 2(16):2263–2266, 2004.

[114] Mohammed Ibrahim Nail Saleh et al. *Characterization of Potassium Permanganate By Using The (UV-VIS) Spectrophotometer*. PhD thesis, Sudan University of Science and Technology, 2015.

[115] Peter B Johnson and R-W_ Christy. Optical constants of the noble metals. *Physical review B*, 6(12):4370, 1972.

[116] Edward D Palik. *Handbook of optical constants of solids*, volume 3. Academic press, Maryland, 1998.

[117] Amy M Michaels, Jiang Jiang, and Louis Brus. Ag nanocrystal junctions as the site for surface-enhanced raman scattering of single rhodamine 6g molecules. *The Journal of Physical Chemistry B*, 104(50):11965–11971, 2000.

[118] E Prodan, C Radloff, Naomi J Halas, and P Nordlander. A hybridization model for the plasmon response of complex nanostructures. *Science*, 302(5644):419–422, 2003.

[119] Ilanit Doron-Mor, Zahava Barkay, Neta Filip-Granit, Alexander Vaskevich, and Israel Rubinstein. Ultrathin gold island films on silanized glass. morphology and optical properties. *Chemistry of materials*, 16(18):3476–3483, 2004.

[120] Masahiro Inoue and Kazuo Ohtaka. Surface enhanced raman scattering by metal spheres. i. cluster effect. *Journal of the Physical Society of Japan*, 52(11):3853–3864, 1983.

[121] Tavakol Pakizeh. Optical absorption of plasmonic nanoparticles in presence of a local interband transition. *The Journal of Physical Chemistry C*, 115(44):21826–21831, 2011.

[122] Craig F Bohren and Donald R Huffman. *Absorption and scattering of light by small particles*. John Wiley & Sons, Fedral republic of Germany, 2008.

[123] NL Dmitruk, SZ Malynych, IE Moroz, and V Yu Kurlyak. Optical efficiency of ag and au nanoparticles. *Semiconductor physics quantum electronics & optoelectronics*, (13,14):369–373, 2010.

[124] David D Evanoff and George Chumanov. Size-controlled synthesis of nanoparticles. 2. measurement of extinction, scattering, and absorption cross sections. *The Journal of Physical Chemistry B*, 108(37):13957–13962, 2004.

[125] Rongchao Jin, YunWei Cao, Chad A Mirkin, KL Kelly, George C Schatz, and JG Zheng. Photoinduced conversion of silver nanospheres to nanoprisms. *Science*, 294(5548):1901–1903, 2001.

[126] Encai Hao and George C Schatz. Electromagnetic fields around silver nanoparticles and dimers. *The Journal of chemical physics*, 120(1):357–366, 2004.

[127] K Bouzidi, MABA Chegaar, and A Bouhemadou. Solar cells parameters evaluation considering the series and shunt resistance. *Solar Energy Materials and Solar Cells*, 91(18):1647–1651, 2007.

[128] Francis Otieno Otieno. *Enhancement of photo-conversion efficiency of organic solar cells by plasmon resonance effect*. PhD thesis, 2016.

[129] P Apell, R Monreal, and S Lundqvist. Photoluminescence of noble metals. *Physica Scripta*, 38(2):174, 1988.